

Fall 2013

# The Application and Analysis of Automated Triangulation of Video Imagery by Successive Relative Orientation

Jae Sung Kim  
*Purdue University*

Follow this and additional works at: [https://docs.lib.purdue.edu/open\\_access\\_dissertations](https://docs.lib.purdue.edu/open_access_dissertations)



Part of the [Civil Engineering Commons](#)

---

## Recommended Citation

Kim, Jae Sung, "The Application and Analysis of Automated Triangulation of Video Imagery by Successive Relative Orientation" (2013). *Open Access Dissertations*. 149.  
[https://docs.lib.purdue.edu/open\\_access\\_dissertations/149](https://docs.lib.purdue.edu/open_access_dissertations/149)

This document has been made available through Purdue e-Pubs, a service of the Purdue University Libraries. Please contact [epubs@purdue.edu](mailto:epubs@purdue.edu) for additional information.

**PURDUE UNIVERSITY**  
**GRADUATE SCHOOL**  
**Thesis/Dissertation Acceptance**

This is to certify that the thesis/dissertation prepared

By Jae Sung Kim

Entitled

The Application and Analysis of Automated Triangulation of Video Imagery by  
Successive Relative Orientation

For the degree of Doctor of Philosophy

Is approved by the final examining committee:

James S. Bethel

Chair

Mireille Boutin

Henry J. Theiss

Daniel G. Aliaga

To the best of my knowledge and as understood by the student in the *Research Integrity and Copyright Disclaimer (Graduate School Form 20)*, this thesis/dissertation adheres to the provisions of Purdue University's "Policy on Integrity in Research" and the use of copyrighted material.

Approved by Major Professor(s): James S. Bethel

Approved by: Michael E. Kreger

Head of the Graduate Program

10/04/2013

Date

THE APPLICATION AND ANALYSIS OF AUTOMATED TRIANGULATION OF  
VIDEO IMAGERY BY SUCCESSIVE RELATIVE ORIENTATION

A Dissertation

Submitted to the Faculty

of

Purdue University

by

Jae Sung Kim

In Partial Fulfillment of the

Requirements for the Degree

of

Doctor of Philosophy

December 2013

Purdue University

West Lafayette, Indiana

To my family.



## ACKNOWLEDGEMENTS

I would like to express my gratitude to committee chair, Professor James Bethel for his insight, guidance and advice. And I would like to express my gratitude to committee members – Professor Daniel Aliaga, Professor Mimi Boutin, Dr. Henry Theiss for their helpful ideas and recommendation.

And, I would like to thank to Professor Edward Mikhail for his teaching and consultation. Also, I appreciate the opportunity to work with Chris Miller, Professor Jane Frankenberger, Laura Esman, and Larry Theller. My appreciation extends to Ms. Jenny Ricsky and Ms. Dorothy Miller for their coordination for my Ph.D work.

I would like to express my gratitude to the cohorts and colleagues from Purdue geomatics – Derek Fuller, Eric Fuller, Wasin Rujikietgumjorn, Luis Gaztambide, Ruben Gaztambide, Janice Patrick, James Monty, Kyohyuk Kim, Yunting Su, Chiung-Shiuan Fu, and Scott Peterson.

## TABLE OF CONTENTS

	Page
LIST OF TABLES .....	vi
LIST OF FIGURES .....	xi
ABSTRACT .....	xv
CHAPTER 1. INTRODUCTION.....	1
1.1 Statement of the Problem .....	1
1.2 Summary of Methodology .....	2
1.3 Objectives.....	4
1.4 Approach .....	6
CHAPTER 2. LITERATURE REVIEW.....	10
2.1 Camera Calibration.....	10
2.2 Interest Point Detection and Matching Literature.....	13
2.3 Relative Orientation and Pose Estimation Literature .....	17
CHAPTER 3. THE DESCRIPTION OF EQUIPMENT AND DATA .....	25
3.1 Video Camera Equipment.....	25
3.2 Video Data Description .....	27
3.3 Control Point Acquisition by GPS Surveying .....	31
CHAPTER 4. AUTOMATED RELATIVE ORIENTATION .....	37
4.1 Interest Point Detection .....	37
4.2 Matching by Cross Correlation & RANSAC .....	43
4.3 Relative Orientation by Eight Point Algorithm .....	46
4.4 Relative Orientation by Coplanarity and Scale Restraint Conditions.....	51
4.5 Camera Calibration.....	57
4.6 Absolute Orientation .....	62

	Page
4.7 Bundle Block Adjustment.....	64
4.8 Post Adjustment Statistics .....	66
CHAPTER 5. ESTIMATION STRATEGIES.....	70
5.1 Simultaneous Least Squares .....	70
5.2 Cantilever Least Squares .....	72
5.3 Kalman Filtering Least Squares.....	74
CHAPTER 6. APPLICATIONS .....	81
6.1 APPLICATION1: Camera Calibration .....	81
6.1.1 Calibration from Urban, Laboratory Scene .....	83
6.1.2 Calibration from Aerial Imageries .....	108
6.2 APPLICATION 2: Automated Relative Orientation	
– Terrestrial Case.....	112
6.3 APPLICATION 3: Automated Relative Orientation	
– Aerial Case .....	123
6.3.1 Relative Orientation.....	123
6.3.2 Bundle Block Adjustment (BBA).....	138
6.3.3 Absolute Orientation for SLS, KF, and CLS .....	149
6.4 APPLICATION 4: Automated Relative Orientation	
– Simulation .....	156
6.4.1 Relative Orientation.....	157
6.4.2 Bundle Block Adjustment (BBA).....	174
6.4.3 Absolute Orientation for SLS, KF, and CLS .....	179
CHAPTER 7. CONCLUSIONS AND RECOMMENDATIONS .....	186
7.1 Conclusions.....	186
7.2 Recommendations.....	190
LIST OF REFERENCES .....	191
APPENDICES	
Appendix A Static GPS Survey Log .....	203
Appendix B RTK GPS Survey Log .....	207
Appendix C Exterior Orientation Parameters from Simulation.....	208
VITA .....	234

## LIST OF TABLES

Table	Page
3.1 Initial Approximation of Camera Calibration Parameters .....	28
3.2 The Precision of GPS Survey .....	33
6.1 <i>A Priori</i> Standard Deviation of Interior Orientation Parameters .....	83
6.2 The Result of Calibration (Urban 1) .....	87
6.3 RMS of Residuals (Urban 1, units=pixels) .....	88
6.4 Correlation Matrix for Calibration Parameters (Urban1) .....	88
6.5 The Result of Calibration (Urban 2) .....	91
6.6 RMS of Residuals (Urban 2, units=pixels) .....	91
6.7 Correlation Matrix of the Calibration Parameters (Urban 2).....	91
6.8 The Result of Calibration (Urban 3) .....	94
6.9 RMS of Residuals (Urban 3, units=pixels) .....	94
6.10 Correlation Matrix of Calibration Parameters (Urban 3).....	94
6.11 The Result of Calibration (Laboratory 1).....	99
6.12 RMS of Residuals (Laboratory 1, units=pixels).....	100
6.13 The Result of Calibration (Laboratory 2).....	102
6.14 RMS of Residuals (Laboratory 2, units=pixels).....	102

Table	Page
6.15 The Comparison of Misclosures at Checkpoints for Each Calibration. Units are meters in object space. “group1” and “group2” refer to swapping the role of control and check points.....	104
6.16 The Comparison of Standard Deviations (units=pixels).....	106
6.17 Interior Orientation Parameters for Uncalibrated Camera.....	109
6.18 <i>A Priori</i> Standard Deviations for Interior Orientation Parameters (sigmas chosen to represent “unknown” parameters) .....	109
6.19 The Result of Self Calibration Using Aerial Imagery (groups interchange of control and check points) .....	110
6.20 RMS of Residuals for Self Calibration (units=pixels) .....	111
6.21 RMS Misclosure at Check Points (units=meters).....	111
6.22 Data Acquisition.....	112
6.23 Data Description .....	112
6.24 Parameter Setup .....	114
6.25 Exterior Orientation Parameters from SLS .....	116
6.26 Exterior Orientation Parameters from CLS .....	117
6.27 Exterior Orientation Parameters from KF.....	117
6.28 Observation Residuals of Each Solution (RMS, units=pixels) .....	117
6.29 RMS Discrepancy of CLS and KF from SLS.....	118
6.30 Semi Major and Minor Axis of Error Ellipsoid.....	121
6.31 Memory Occupancy of Each Solution.....	123
6.32 Aerial Data Acquisition.....	124

Table	Page
6.33 Data Description .....	124
6.34 The Parameters for Interest Point Detection and Matching .....	125
6.35 Exterior Orientation Parameters from SLS .....	133
6.36 Exterior Orientation Parameters from KF .....	133
6.37 Exterior Orientation Parameters from CLS .....	134
6.38 Residual of Each Solution (RMS, units=pixels) .....	134
6.39 The Semi Major and Minor Axis of Error Ellipsoid (units=meters).....	136
6.40 Comparison of Confidence Ellipsoid for Original Selection of Dynamic Model Covariance versus Covariance from Propagation (Composite of All Points) .....	137
6.41 Memory Occupancy of Each Solution.....	137
6.42 Exterior Orientation Parameters from Bundle Block Adjustment.....	141
6.43 The RMS of Residuals (units=pixels).....	144
6.44 Seven Parameter Values for Transformation to the Control Points from BBA w/ Minimal Constraints.....	144
6.45 Misclosures of Check Points (units=meters).....	145
6.46 The Length of Semi Major Axis of Error Ellipsoid at Pass Points.....	146
6.47 The Comparison of Interior Orientation Parameters .....	148
6.48 The Comparison of Exterior Orientation Parameters .....	149
6.49 The Seven Parameters Estimated by Absolute Orientation .....	150

Table	Page
6.50 Misclosures at Check Points for Seven Parameter Transformation (units=meters) .....	151
6.51 The Polynomial Parameters Estimated by Absolute Orientation .....	152
6.52 Misclosures at Check Points for Schut Polynomial Transformation .....	155
6.53 The Comparison of Misclosures for Each Method (units=meters), (AO=absolute orientation, MC=minimal constraints).....	156
6.54 The Nominal Parameters for Simulation .....	158
6.55 The Random Perturbations Added to Nominal Values (Sigmas for RNG) .....	158
6.56 The Semi Major and Minor Axis of Error Ellipsoid (units=meters).....	172
6.57 Average Memory Occupancy (MB). Note: Matlab returns slightly different numbers when running the same program .....	174
6.58 The RMS of Residuals (units=pixels).....	176
6.59 Seven Parameter Transformation to the Control Points from BBA w/ Minimal Constraints .....	177
6.60 Misclosures of Check Points (units=meters) with only MC plus AO.....	178
6.61 The Seven Parameters Estimated by Absolute Orientation .....	180
6.62 Misclosures at Check Points for Seven Parameter Transformation (units=meters) .....	182
6.63 The Comparison of Misclosures of Each Method (units=meters).....	184
B.1 RTK GPS Survey Log .....	207

Table	Page
C.1 Simulation 1 .....	208
C.2 Simulation 2 .....	213
C.3 Simulation 3 .....	218
C.4 Simulation 4 .....	224
C.5 Simulation 5 .....	229



## LIST OF FIGURES

Figure	Page
3.1 SONY HDR CX 100 Camcorder .....	27
3.2 Drive Path for Terrestrial Video Data Acquisition.....	29
3.3 Flight Path for Aerial Video Data Acquisition .....	30
3.4 GPS Surveying Plan.....	34
3.5 Top: Static GPS Antenna and Receiver. Bottom: RTK Receiver, Antenna, Data Collector, and Cellular Data Device.....	35
3.6 Static (Left) and RTK (Right) GPS Surveying .....	36
5.1 The types of Kalman Filtering (can also be done without smoothing).....	77
6.1 Three Calibration Approaches .....	82
6.2 Calibration Target for Urban 1 and 2 .....	84
6.3 Calibration Target for Urban 3 .....	85
6.4 Pass Point plot of Urban 1 .....	87
6.5 Grid Plot of Radial and Decentering Distortions of Urban 1 (Effects are exaggerated by $\times 3$ ) .....	89
6.6 Quiver Plot of Urban 1 (Effects are exaggerated by $\times 3$ ) .....	89
6.7 Pass Point plot of Urban 2.....	90

Figure	Page
6.8 Grid Plot of Radial and Decentering Distortions of Urban 2 (Effects are exaggerated by $\times 3$ ) .....	92
6.9 Quiver Plot of Urban 2 (Effects are exaggerated by $\times 3$ ) .....	92
6.10 Pass Point Plot of Urban 3.....	93
6.11 Grid Plot of Radial and Decentering Distortions of Urban 3 (Effects are exaggerated by $\times 3$ ) .....	95
6.12 Quiver Plot of Urban 3 (Effects are exaggerated by $\times 3$ ) .....	95
6.13 Calibration Targets for Laboratory 1 .....	97
6.14 Calibration Targets for Laboratory 2 .....	98
6.15 Pass Point Plot of Laboratory 1 .....	99
6.16 Radial and Decentering Distortions of Laboratory 1 .....	100
6.17 Quiver Plot of Laboratory 1 .....	101
6.18 Pass Point Plot of Laboratory 2 .....	101
6.19 Radial and Decentering Distortions of Laboratory 2 .....	103
6.20 Quiver Plot of Laboratory 2.....	103
6.21 Radial Distortion according to $K_1$ , $K_2$ and $K_3$ .....	107
6.22 The distribution of the contribution of $K_1$ , $K_2$ and $K_3$ (Left: Uncorrelated, Right: Correlated).....	108
6.23 Input Data to Automated Relative Orientation .....	113
6.24 Subregion for Sampling Points .....	114
6.25 Matched Points in Terrestrial Images .....	115
6.26 Comparison of X Coordinates.....	120
6.27 Comparison of Y Coordinates.....	120

Figure	Page
6.28 Comparison of Z Coordinates.....	120
6.29 Error Ellipsoids from Each Approach (SLS Top Left, CLS: Top Right, KF: Bottom Center) .....	121
6.30 Scale Restraint Equations .....	122
6.31 Aerial Dataset over Purdue Campus .....	128
6.32 Matched Points for Each Pair of Images 1-3, 3-5, 5-7, 7-9, ... . The intermediate images are also shown. The images are organized as triplets. ....	132
6.33 X Coordinate Comparison .....	135
6.34 Y Coordinate Comparison .....	135
6.35 Z Coordinate Comparison.....	135
6.36 Error Ellipsoids from Each Approach (SLS w/ Apriori Covariance for White Noise: Top Left, SLS w/ Propagated Covariance for White Noise: Top Right, CLS: Bottom Left, KF: Bottom Right) .....	137
6.37 Control, Check and Pass Points Configuration (The First Group) .....	139
6.38 Control, Check and Pass Points Configuration (The Second Group) .....	140
6.39 Error Ellipsoid for Pass Point2 from Group 1 .....	147
6.40 The Data for the Comparison of BBA with iWitness .....	148
6.41 Pass, Scale Restraint, Control and Check Points for Simulation.....	158
6.42 Pass, Scale Restraint, Control and Check Points for Simulation.....	159
6.43 Strip Deformation in Z direction .....	161

Figure	Page
6.44 Strip Deformation Comparison, Simulation 1, y axis is exaggerated by $\times 4.62$ (Top: X, Center: Y, Bottom: Z) .....	162
6.45 Strip Deformation Comparison, Simulation 1, Real Aspect Ratio (Top: X, Center: Y, Bottom: Z) .....	163
6.46 Strip Deformation Comparison, Simulation 2, y axis is exaggerated by $\times 3.97$ (Top: X, Center: Y, Bottom: Z) .....	164
6.47 Strip Deformation Comparison, Simulation 2, Real Aspect Ratio (Top: X, Center: Y, Bottom: Z) .....	165
6.48 Strip Deformation Comparison, Simulation 3, y axis is exaggerated by $\times 2.39$ (Top: X, Center: Y, Bottom: Z) .....	166
6.49 Strip Deformation Comparison, Simulation 3, Real Aspect Ratio (Top: X, Center: Y, Bottom: Z) .....	167
6.50 Strip Deformation Comparison, Simulation 4, y axis is exaggerated by $\times 2.14$ (Top: X, Center: Y, Bottom: Z) .....	168
6.51 Strip Deformation Comparison, Simulation 4, Real Aspect Ratio (Top: X, Center: Y, Bottom: Z) .....	169
6.52 Strip Deformation Comparison, Simulation 5, y axis is exaggerated by $\times 1.82$ (Top: X, Center: Y, Bottom: Z) .....	170
6.53 Strip Deformation Comparison, Simulation 5, Real Aspect Ratio (Top: X, Center: Y, Bottom: Z) .....	171
6.54 Error Ellipsoid from Each Approach (SLS: Top Left, CLS: Top Right, KF: Bottom Center) .....	173
7.1 Misclosures at Check Points of Each Calibration .....	187
7.2 Average Standard Deviation of Each Calibration .....	187

## ABSTRACT

Kim, Jae Sung. Ph.D., Purdue University, December 2013. The Application and Analysis of Automated Triangulation of Video Imagery by Successive Relative Orientation. Major Professor: Dr. James S. Bethel.

The purpose of this thesis is the analysis and evaluation of methods to orient a strip of images using an automated approach. Automatic orientation of strips of video frame imagery would facilitate the construction of three dimensional models with less demand on a human operator for tedious measurement. Often one has no control points, so only relative orientation is possible. The relative orientation process gives camera parameters such as attitudes and selected baseline components and it can be implemented by using either collinearity or coplanarity equations. To automate the point selection, the pass and/or tie points were detected by the Colored Harris Laplace Corner detector along a strip of images and they were matched by cross correlation across multiple scales. However, the matched points from cross correlation still include the outliers. Therefore, the Random Sample Consensus (RANSAC) method with the essential matrix was applied to detect only inliers of point pairs. Then relative orientation was performed for this series of video imagery using the coplanarity condition. However, there is no guarantee that three rays for a single point will intersect in a single point. Therefore for all photos, subsequent to the

first one, the scale restraint equation was applied along with the coplanarity equation to ensure these three rays' intersection. At this point, the Kalman Filtering algorithm was introduced to address the problem of uncompensated systematic error accumulation. Kalman Filtering is more parsimonious of computing effort than Simultaneous Least Squares, and it gives superior results compared with Cantilever Least Squares models by including trajectory information.

To conform with accepted photogrammetric standards, the camera was calibrated with selected frames extracted from the video stream. For the calibration, minimal constraints are applied. Coplanarity and scale restraint equations in relative orientation were also used for initial approximation for the nonlinear bundle block adjustment to accomplish camera calibration. For calibration imagery, the main building of the bell tower at the University of Texas was used as an object because it has lots of three dimensional features with an open view and the data could be acquired at infinity focus distance. Another two sets of calibrations were implemented with targets placed inside of a laboratory room.

The automated relative orientation experiment was carried out with one terrestrial, one aerial and another simulated strip. The real data was acquired by a high definition camcorder. Both terrestrial and aerial data were acquired at the Purdue University campus. The terrestrial data was acquired from a moving vehicle. The aerial data of the Purdue University campus was acquired from a Cessna aircraft. The results from the aerial and simulation cases were evaluated

by control points. The three estimation strategies are stripwise Simultaneous, Kalman Filtering and Cantilever, all employing coplanarity equations. For the aerial and simulation case, an absolute comparison was made between the three experimental techniques and the bundle block adjustment. In all cases, the relative solutions were transformed to ground coordinates by a rigid body, 7-parameter transformation. In retrospect, the aerial case was too short (8 photographs) to demonstrate the compensation of strip formation errors. Therefore a simulated strip (30 photographs) was used for this purpose. Absolute accuracy for the aerial and simulation approaches was evaluated by ground control points. Precision of each approach was evaluated by error ellipsoid at each intersected point. Also memory occupancy for each approach was measured to compare resource requirements for each approach. When considering computing resources and absolute accuracy, the Kalman Filter solution is superior compared with the Simultaneous and the Cantilever methods.

## CHAPTER 1. INTRODUCTION

### 1.1 Statement of the Problem

To better reconstruct the 3D geometry of a scene from a strip of imagery, we analyze, evaluate and seek to better the automation of this task. This has been attempted since early in the twentieth century by analog means. In a digital environment, one could approach the task by bundle blocks adjustment or by successive relative orientation. The latter approach presents interesting possibilities for sequential estimation, and it therefore was chosen for study. To fully exploit this technique, we must also introduce some automation of the measurement task. The problem is to automate the process of image strip formation using the coplanarity model.

The image rays from conjugate points intersect in space and reestablish the original epipolar geometry of a pair of images (Mikhail, Bethel & McGlone, 2001). This process is called relative orientation and it gives camera parameters such as attitudes and selected baseline components. Since the relative orientation procedure requires the coordinates of conjugate points in the pair of images, the coordinates have to be measured either manually or automatically. In a real world situation, there are often more than just one pair of images, and it requires a lot of human effort to measure the conjugate point coordinates for the



entire dataset manually. Therefore, automatic measurement of conjugate points can reduce the effort and time required and also, it can increase the accuracy by preventing human measurement errors.

## 1.2 Summary of Methodology

The first step of automatic relative orientation is camera calibration. An uncalibrated camera has inaccurate values for principal point offset, focal length, radial distortion and tangential distortion determined by calibration. These inaccurate interior orientation parameters should be determined by calibration to guarantee high quality results. Camera calibration has re-emerged as a research topic along with the dynamic developments in digital camera technology. A calibration facility with accurately located targets is an expensive proposition. Therefore, a camera calibration procedure which doesn't require control point information was used in this research.

After camera calibration, one can proceed with photogrammetric applications. To automate the selection and measurement of pass points, the concept of interest points were used. There are several algorithms for interest point detection and they have different characteristics. Therefore, the most reliable method should be sought to increase the accuracy and efficiency of the proposed methodology. The detected interest points in each image can be matched between photographs by cross correlation, if the convergence angle between adjacent photographs is not large. To increase the reliability of cross correlation, matching was performed in multi-level image pyramids. Still, the

matching is not always correct and the wrongly matched points should be removed. The automatic procedure for the conjugate point coordinates measurement should fulfill the above requirements. Once a correct and well distributed set of conjugate points are prepared, they are used in the relative orientation procedure to estimate exterior orientation parameters. We can fix the orientation of one photograph of the pair, and then fix one of the orientation parameters ( $b_x, b_y, b_z, \omega, \phi, \kappa$ ) of the second photograph and solve for the rest of the parameters, which gives position of the second camera in a relative sense. The coplanarity condition was chosen as the basic equation for the relative orientation procedure. Since the coplanarity condition doesn't guarantee three rays' intersection for three ray points, the scale restraint condition equation was introduced to force this three ray intersection. Therefore, the math model for the first pair of images carries five parameters, out of six possible exterior orientation parameters, but those from the second pair of images carry six parameters with the scale restraint equation introduced as just described. The six parameter model is used for all subsequent image pairs in the strip.

For a series of image pairs, the exterior orientation parameters can be estimated by relative orientation with either sequential or simultaneous solution. For the sequential solution, the parameters can be estimated for the first pair of images, and those from second pair can be added to the first solution. This procedure is repeated to the last pair of images. However, systematic errors from lens distortion and atmospheric refraction can be accumulated in this procedure especially for uncalibrated case and it becomes larger as number of image pairs

increases, which is called the cantilever effect. So, we call this type of least squares solution “Cantilever” Least Squares. The cantilever effect can be alleviated by introducing trajectory information in simultaneous solution. However, simultaneous solutions incur efficiency problems because of large matrix size. We need a solution which can mitigate systematic error from Cantilever Least Squares and increase efficiency from Simultaneous Least Squares. Therefore, a sequential estimation technique using the Kalman Filter was introduced to address these problems since the Kalman Filter can reduce the cantilever errors by forward and backward smoothing, and it doesn’t occupy large memory because at each epoch, we only estimate the parameters in the state vector rather than the entire strip.

### 1.3 Objectives

The overall objective of this research is to analyze and improve fully automated and robust procedures for strip triangulation by successive relative orientations. The specific objectives are to:

1. Analyze Simultaneous, Cantilever, and Kalman Filter approaches. The analysis of each approach is the most important aspect in this research.
2. Investigate prior work related to automatic relative orientation and related subjects through extensive literature review from the photogrammetry, computer vision, signal and image processing fields.

3. Develop a practical camera calibration procedure with the goal of recovering camera parameters such as principal point offsets  $(x_0, y_0)$ , focal length  $(f)$ , three radial distortion parameters  $(K_1, K_2, K_3)$ , and two decentering distortion parameters  $(P_1, P_2)$ . The calibration should be performed without measurement of control points in the object space. Note that the “focal length” should really be designated “principal distance”, but at infinity focus, the two are identical.
4. Acquire strip oriented terrestrial data from car and airborne data from aircraft. The data acquisition plan should be restricted to only fair weather conditions in both cases. The target area/object should be chosen to ensure a sufficient number of well defined features so that an interest point based strategy will be successful. The imagery will be captured as a video stream. Overlap between successive frames will be guaranteed by a combination of vehicle velocity/frame rate and selective sampling of individual frames.
5. For both terrestrial and aerial datasets, detect interest points by the Colored Harris Laplace corner detector, which is considered to be a reliable interest point detector.
6. Match the candidate point sets by multi scale cross correlation for each image pyramid by feature tracking. By this means, the interest points which are matched through the top of the image pyramid will survive and be input to the next step.
7. Detect inliers by Random Sample Consensus (RANSAC) using the model of the eight point algorithm to solve for the elements of the essential matrix.

Because there may be still mismatched points from the cross correlation, RANSAC was adopted to filter out those outlier points which are mismatched.

8. Using “clean” data and approximations from the linear solution just described, Solve relative orientation with coplanarity and scale restraint condition equations using three frameworks: (a) Simultaneous Least Squares, (b) Cantilever Least Squares and (c) Sequential Least Squares (Kalman Filter). The results of each algorithm will be compared and the relative strengths and weakness of each will be addressed.

9. Estimate orientation in the world object space coordinate system. The first approach is a one step procedure using bundle block adjustment. The second approach is a two step procedure with relative followed by absolute orientation. The bundle blocks adjustment would be the conventional approach to solving this problem, without regard to computer resource constraint. The absolute orientation will be implemented by both seven parameter conformal and polynomial non conformal transformation. The results of the absolute orientation from each approach: Simultaneous, Cantilever, and Kalman Filter will be compared.

#### 1.4 Approach

Images can be oriented efficiently without labor intensive manual measurements of conjugate image points and without acquisition of control point information by automation of the relative orientation procedure.

Camera calibration plays a key role in any photogrammetric operation. False calibration parameters or uncalibrated parameters (nominal values) will severely limit the achievable accuracy of any proposed method. Therefore, the chosen camera will be calibrated rigorously by the self-calibration technique with both signalized target points and photo ID target points in the object space. The calibration will be done using bundle block adjustment with added parameters. Since this is nonlinear, we need initial approximation. The exterior orientation parameters are initially approximated by the eight point algorithm. The eight point algorithm gives four solutions for exterior orientations and their ambiguity was resolved by geometric reasoning. Once exterior orientations are initially approximated, they can be confirmed by nonlinear estimation in the conventional relative orientation algorithm, then used as initial approximation for the bundle block adjustment with added parameters. This finally results in the needed calibration parameters. For the block adjustment, we use only minimal constraints. This alleviates any requirement for control points in the object space which makes the procedure very easy to accomplish.

The proposed research will be tested against sequences of video imagery selected frames for terrestrial and aerial cases. The images will be captured with selected frames chosen to be reasonable image overlap. The performance of matching by cross correlation decreases if the overlap is too small or equivalently if the base height ratio is too large. Conversely, if the base height ratio becomes very small and the rays become nearly parallel, the matching works better and better but the geometric strength collapses. Therefore, frames were selected so

that the overlap ratio should be between 60~80 %. The terrestrial data were taken from a moving vehicle and the aerial video imageries were taken from a Cessna aircraft. It should be noted that the proposed method can also be adapted for digital still camera cases, but it is hard to manually trigger a series of photos to achieve a fixed overlap ratio in a moving vehicle.

The automatic detection of conjugate interest points is a key step which ensures the automation of the whole procedure of strip formation by relative orientation. Interest point detection is a large field of research itself and the most of reliable methodology was sought. From this search, the Colored Harris Laplace corner detector was chosen as the one most appropriate for this project. The detected interest points are matched across images by cross correlation and the matching is performed in multi-scale to increase reliability. However, there still exist outliers among the matched point pairs and they are excluded using the Random Sample Consensus (Fishler & Bolles, 1981) method. For a pair of images, relative orientation can be implemented by the General Least Squares method and the coplanarity equation. However, this approach is not sufficient for more than two consecutive images because there is no guarantee that three conjugate rays will intersect in a single point only. The scale restraint equation handles this problem by constraining the intersection of the three rays to a single point. Therefore, the condition equations of the first pair of images have only coplanarity conditions with five exterior orientation parameters (one of the exterior orientation parameters was fixed). From the second model, the condition equations include both coplanarity and scale restraint equations with six exterior orientation

parameters. This set of condition equations of multiple successive relative orientations can be solved by different algorithms. Three algorithms have been selected for study. The first case is Simultaneous Least Squares, the second case is Cantilever Least Squares, and the last case is Sequential Least Squares with a dynamic model, also known as the Kalman Filter. Subsequently they will be referred to as SLS, CLS, and KF. The application of KF algorithm to the strip formation problem, together with the automated point determination represents an innovative approach to the solution of this problem. It will be compared with the cited alternative algorithms.



## CHAPTER 2. LITERATURE REVIEW

The reviewed literature covers the subject of camera calibration, interest point detection and matching, relative orientation for pose estimation, and Kalman Filtering. The scope of the literatures includes publications from the fields of photogrammetry, computer vision, signal and image processing, statistics, and even biology.

### 2.1 Camera Calibration

Much research has been done in the field of camera calibration. Brown (1971) used an analytical plumb-line method which used a test field consisting of a series of plumb lines to calibrate close range cameras to estimated inner orientation elements including radial and decentering distortions. His experiment showed that the plumb-line method is superior in convenience and provides comparable accuracy with the costlier stellar calibration method. Tsai (1987) introduced a calibration method using a two-stage technique which computes both interior and exterior camera parameters. In the proposed technique, initial approximations are obtained for all elements of interior and exterior orientation, including target object points. In the next step, a bundle block adjustment with self-calibration is performed. He also showed that 60 points are more than

sufficient to obtain a good calibration. Weng, Huang, and Ahuja (1992) employed camera calibration to estimate principal point offset, and lens distortions such as radial, decentering, and prism. They estimated the principal point offset from a distortion free camera model by a closed form model in the first step. In the following step, the geometric distortion parameters were estimated by non-linear optimization. Cooper and Robson (1996) explained the classical camera calibration model in terms of principal distance, principal point offset, and radial and tangential distortion. They noted that the principal distance value is usually to the nearest  $10\ \mu m$  and the maximum magnitude of radial lens distortion is about  $10\text{-}20\ \mu m$  for a large format metric camera. Of course this project employs a non-metric camera. Also, they explained the multistation bundle adjustment, where exterior orientation, camera calibration data, and object space coordinates can be estimated by an Iterative Least Squares method. Robert (1996) showed a new one stage method of pinhole type camera calibration. Classical calibration is composed of two steps, which are point or a feature extraction, followed by estimation of the chosen parameters. But proposed method searches camera parameters which projects three dimensional points of pattern to the edges in the pattern by characterizing edge as zero crossing of Laplacian. And it didn't extract image features to estimate calibration parameters, but they calibrated camera during the process of edge estimation. He showed that the proposed method reduced systematic error than classical two stage based method. Heikkila (1997) suggested a four step camera calibration procedures. The first step is the linear and closed form solution to the direct linear transformation (DLT). The second

step is the nonlinear estimation of exterior orientation parameters with the initial estimates from DLT. The third step is the estimation of the distortion parameters. The fourth step is the image correction carried out by resampling of the original image using the physical camera parameters obtained by the previous steps. The experiments showed that the remaining errors were negligible and the procedure is recommended to the various machine vision applications requiring high geometrical accuracy. Fraser (1997) described self-calibration of a digital CCD sensor camera. The condition equation includes the terms for sensor exterior orientation, the object point coordinates, and self-calibration parameters. The calibration parameters are radial lens distortion ( $K_1, K_2, K_3$ ), decentering distortion ( $P_1, P_2$ ), interior orientation ( $x_0, y_0, c$ ), and in-plane distortion ( $b_1, b_2$ ), which gives total of 10 parameters. Clarke and Fryer (1998) explained the history of camera calibration and described the advantages and disadvantages of each method. They explained the history of stereoscopic restitution and related camera calibration methodologies. They reviewed math models, self-calibration and Least Squares applied to multi collimator calibration like USGS. Also, they investigated the plumb-line calibration, the additional parameters technique, and on-the-job calibration. Finally, they explained the application of calibration to the close range cameras. Sturm and Maybank (1999) presented a calibration algorithm for plane based object with versatile number of views and planes. The algorithm is consisted of computing plane homographies from feature correspondences, construction of equation matrix  $A$ , conditioning by rescaling rows and columns, and the solution by Least Squares. Experiments showed

satisfactory results and the calibration method could be used for economic calibration tool, ground plane calibration, reconstruction of piecewise planar objects from single views, reconstruction of indoor scenes, and augmented reality. Zhang (1999) suggested a flexible technique to calibrate cameras. In the proposed method, only a few observations to planar objects at different orientations are required. The method is composed of a closed form solution to the camera intrinsic (interior orientation) matrix, nonlinear refinement by the maximum likelihood criterion, and solution for radial distortions.

## 2.2 Interest Point Detection and Matching Literature

Moravec (1980) developed a corner detector function by moving a window over the image. If the windowed image region is homogeneous and it has no edge or no corner, then all shifts will give a small change in the function. If there is an edge, a shift perpendicular to the edge will give large change. And if there is a corner, a shift in both directions will give large change. But there are several drawbacks to the Moravec corner detector. It has anisotropic response, noisy response, and false positives at edges. Harris and Stephens (1988) addressed these problems in the following way. The anisotropic response occurred because Moravec's corner detector considered 45 degree shift. Harris corner detector covers all possible small shifts by an analytic expansion. Moravec's binary and rectangular window caused noisy response, which are solved by circular Gaussian window. The sensitivity to edges was solved by reformulating corner measure to the objective function comprised of eigenvalue expression, which can

differentiate from edge and corner better than Moravec corner detector. Lindeberg (1998) suggested automatic selection of characteristic scales using normalized Gaussian derivatives for blob and junction detection and frequency estimation. Characteristic scales were determined so that differential descriptors have the maxima over scales. Also, he suggested feature localization especially for detected junctions since the detected corners doesn't guarantee the accurate position of points. Schmid (1997) used local grey value multi scale invariants at the interest points and a voting algorithm to match and retrieve images. First a set of differential local jet, which is the convolution of Gaussian function to the image with  $\sigma$  (the size of Gaussian) to consider multi-scale approach, was calculated and the mahalanobis distance and voting algorithm was applied to match between input images and model images. The experiment considering image rotation, scale changes, viewpoint variations showed successful result. Lowe (1999, 2004) suggested a method which extracts distinctive invariant features to perform matching between different views. The method was invariant to scale and rotation and robust to change in 3d viewpoint, addition of noise, and change in illumination. The approach named of Scale Invariant Feature Transform (SIFT) are composed of four steps such as scale space extrema detection using Difference of Gaussian (DoG), keypoint localization, orientation assignment, and keypoint descriptor. The detected features are matched by correlation and the outliers are detected by voting with Hough Transform. Montesinos, Gouet and Deriche (1998) adapted color information to differential invariants interest point detector to match the points in uncalibrated images. They

used Hilbert's invariants with first order as local characterization for each Red, Green, Blue bands and generalized Harris corner detector considering color data. They compared each feature vectors to match points by computing likeness of two vectors. The result showed that color information improved matching result. Mikolajczyk and Schmid (2001) compared most widely used scale invariant interest point detectors which are Laplacian of Gaussian (LoG), Difference of Gaussian (DoG), gradient, and Harris with scale factor. The result showed that Laplacian of Gaussian detects the most points with the best accuracy. And he proposed interest points detector robust to scale changes, Harris Laplace corner detector, which detects corner points in different scale levels by scale adapted Harris corner detector, and chooses corners which attains local maxima LoG as point with characteristic scale. Mikolajczyk and Schmid (2004) gave detailed description of Harris Laplace corner detector and extended proposed methodology to adapt to significant affine transformation. In later research, Mikolajczyk and Schmid (2005) compared descriptors of interest region, which are shape context, steerable filters, PCA-SIFT, differential invariants, spin images, SIFT, complex filters, moment invariants, and cross correlation. They found out SIFT performs the best among investigated descriptors. Stöttinger, Sebe, Gevers and Hanbury (2007) addressed color interest point detector for image retrieval. They used colored scale invariant corner detector with LoG and quasi invariant color space. Their algorithm was tested for image retrieval by calculating Euclidean distances between SIFT descriptors of each image. The result showed that color based interest point detector is more meaningful, stable,

and distinct than other approaches such as Harris (1988), Lowe (1999), or Mikolajczyk's (2004) approaches because they didn't consider color space.

Lingua and Marenchino (2009) used SIFT operator for feature extraction and matching and they compared SIFT approach with Förstner operator and LSM (Least Squares Matching) technique. By the experiment of relative orientation with terrestrial and aerial images, they concluded that SIFT is good for large geometric and photometric distortion. Also, they could get more number of pairs of points than traditional method. However, SIFT operator couldn't match any points for large scale images with poor texture in the experiment, they implemented new auto adaptive ( $A^2$ ) SIFT operator to fit contrast threshold to the texture near interest point. By their suggested method of  $A^2$  SIFT operator, the matching problems of images with not only high geometric distortion but also poor texture could be handled.

Fischler and Bolles (1981) suggested new paradigm for model fitting which is called Random Sample Consensus (RANSAC). In RANSAC, the minimum numbers of samples are chosen randomly  $n$  times and establish model from each set of sample. The best fitted model could be determined by extracting only inliers which have criteria less than imposing threshold and choosing the model with the most inliers.

O'Neill and Denos (1996) developed automated system for pyramidal area correlation matching scheme. They used pixel averaging filter to texture imagery from coarse resolution to dense resolution in image pyramid, which is called

cascade system. The problem of blunder from correspondence was solved by disparity continuity, affine transformation and parameter constraints.

### 2.3 Relative Orientation and Pose Estimation Literature

One notable research related to relative orientation has been done in motion tracking research in computer vision discipline. In the research of Loguet-Higgins and Prazdny (1980), relative orientation problem was investigated through motion vision problem. They addressed recovering the motions of objects relative to viewer analytically and explained each case of motion through a static environment and a motion relative to a visually textured surface. In later research, Loguet-Higgins (1981) introduced the concept of essential matrix, which he derived from the relationship between two calibrated images. Eight corresponding points in both images gave solution to essential matrix in eight point algorithm and essential matrix gave 4 possible solutions of relative orientation problem. Weng, Huang and Ahuja (1989) dealt with the estimation of motion parameters and the structure of the scene from two perspectives. Feature correspondences between sequential images were established and the motion parameters were estimated for each pair. Then, the local motion was established according to object model dynamics. By the analysis through error simulation depending on motion and system parameters, it was found out that shorter focal length (larger field of view), large translations, translation orthogonal to the image plane gave more reliable estimates. Haralick et al. (1989) addressed the solutions for four pose estimation. They used Closed Form Least Squares



solutions over 2d-2d and 3d-3d cases and a globally convergent iterative method for 2d perspective projections and 3d pose estimation. A simplified linear solution and a robust solution to the 2d-2d perspective projection were used for pose estimation. They concluded that Iterative Weighted Least Squares technique is robust to blunders. Horn (1990) addressed the mathematical solution of recovering baseline and orientation from essential matrix. According to his solution, there is no need for singular value decomposition, coordinate transformation or circular function. However, his solution has two possible combinations and reverse sign of essential matrix gives two more additional combinations of relative orientation solutions. In another paper, Horn (1990) suggested a simple iteration method to solve relative orientation problems other than traditional photogrammetric iterative method which requires good initial approximation of parameters. The iterative methods look for global minimum error solution from any starting point in the parameter space by repeating iteration with different starting values for each rotation. He developed procedures for both cases where initial guess for the rotation is available or not. Besl and McKay (1992) suggested a method for registration of 3-d shapes using iterative closest point (ICP) algorithm, which finds the closest point on a geometric entity to the candidate point. ICP algorithm matches global features based on shape complexity and local features based on shape complexity and the percentage of allowable occlusions. The registration is computed as translations and rotations. Experiments showed the capabilities of the algorithm to point sets, curves and surfaces. Tomasi and Shi (1993) worked on the inference of scene geometry and

camera motion by factorization method which uses singular value decomposition technique. At first, features were selected by automatic detection, and singular valued decomposition was computed. Finally, rotation matrix and shape matrix were computed. It was found out that suggested method is robust to noise and allows very short inter frame feature tracking. Also, Tomasi and Shi (1996) worked on newly developed technique, which is direction of heading from image deformation. They proposed a method to compute the direction of heading from the differential changes in the angles between the projection rays of pairs of point features. The condition equation was solved by minimizing residual. Advantages of using image deformations rather than optical flow is to remove effect of rotation in computation process. However, the suggested process is not fully explored yet and there remain problems such as residual behavior of point position, camera motion, camera calibration and computation efficiency in real time application. Faugeras and Robert (1994) proposed methods of predicting features such as point, line, and curvatures in the third image from two image features analytically by using fundamental matrix. They experimented with real images and also, applied to trinocular stereo matching algorithm. Sullivan and Ponce (1998) proposed a method for automatically constructing G- spline models of 3d objects from several registered photographs. The constructed object models were used in pose estimation. For 100 sample poses, they position the camera so that silhouette of model roughly fits input data. The best fit was chosen as initial pose and minimization of cost through iteration gave final result. Overall, their approach is to minimize the distance to the continuous surface

rather than matching point sets or planes. Pan (1999) showed that two principle distances and five relative orientation parameters were recovered by suggested algebraic technique. He presented a direct closed form solution to the problem and proposed method to retrieve general coplanarity matrix, two principal distances, the special coplanarity matrix, the baseline vector and rotation matrix.

Hartley and Zisserman (2000) showed the derivation, definition and properties of essential matrix. Also they showed how to determine rotation and transition matrix from essential matrix.

Nister (2004) suggested efficient solution to classical five-point algorithm which solves relative pose estimation problem. Tenth degree polynomial coefficients were calculated and the roots were extracted to calculate essential matrix, from which rotation and translation matrices were recovered. The suggested algorithm was applied to RANSAC as a hypothesis generator to solve real-time unknown structure and motion problem.

Brückner, Bajramovic and Denzler (2008) compared eight, seven, six and five point algorithm for relative pose estimation problems. They showed that five point algorithm works well but eight point algorithm is better sometimes. Therefore they invented final combination algorithm which uses five point algorithm for RANSAC and automatically selects the best solution for final estimation between them.

Jasiobedzki, Se, Bondi, and Jakola (2008) performed keeping of Remotely Operated Vehicles (ROV) station and three dimensional mapping of seabed by relative pose estimation. For the purpose of station keeping, they implemented

relative pose estimation by artificial target of Space Vision Marker System (SVMS) and natural features. For natural features, they used Scale Invariant Feature Transform (SIFT) operator. For three dimensional mapping, they used image sequences from mobile stereo cameras and they stored SIFT keypoints to database. They matched SIFT features at each frame with those in the database. And weighted least squares was performed as a final matching step. After performing relative pose estimation, they represented the result by triangular mesh with photorealistic appearances.

Fraundorfer, Tanskanen and Pollefeys (2010) developed minimal case solution for two known orientation angles by solving relative pose problem with three point correspondences for calibrated data taken by smartphone. They suggested new algorithms such as three, four, and linear five point algorithms to estimate essential matrix. This is the special case for smart phones installed with inertial measurement unit (IMU) which measures two orientation angles. The eight point conditions could be reduced to 5 point condition by identifying three linear conditions in essential matrix of two known angles from IMU. The four point condition could be developed by giving zero determinant constraint to five point condition. The three point condition could be established by giving trace condition to the four point condition.

In the photogrammetry discipline, relative orientation is also an important topic and approached differently from computer vision discipline in the view of handling weak geometry. The text of Mikhail et al. (2001) provided the full concept of relative orientation. The coplanarity and scale restraint conditions

were explained in detail including theory, linearization and the solution by Least Squares. Liang and Heipke (1996) worked for automatic relative orientation of aerial photographs. They used modified Moravec's operator with coarser to fine image pyramid strategy using window tracking. For matching, they used not only radiometric constraint such as cross correlation but also geometric constraints such as epipolar geometry and local plane fitting. The blunders of matching were determined by residual analysis so that matched points with residual higher than certain threshold should be discarded. They experimented with ten pairs of images in different areas and showed satisfactory result in the view of accuracy and practicality. Lobonc (1996) suggested automated relative orientation procedure by automated pass point feature succeeded by relative orientation with blunder detection. He concluded that Förstner operator provided the best performance in general and area based correlation with subpixel interpolation gives high accuracy and simplicity. For blunder detection, he showed iterative reweighting technique performed at least as well as statistical technique. Also, he developed iterative orthophoto refinement algorithm where orthophotos are matched and elevation corrections are computed to improve DEM quality. In the research of Theiss (2000), aerial video frames were used as data sets for photogrammetric triangulation and dynamic modeling. He showed schematics of georegistration of airborne video imagery frames. Also, he showed invariance supported triangulation with single frame, two-frame camera parameter recovery, and image transfer and applications to three images. Habib and Kelley (2001) suggested automatic relative orientation algorithm using modified iterated Hough

transformation. They used coplanarity model with extracted edges or feature points. The relative orientation parameters were solved by inputting all possible primitive pairs and choosing the solution which received the most votes. The experiments showed the proposed method is robust and reliable in both urban and rural aerial images. Labe and Förstner (2006) showed rigorous relative orientation procedure, which is composed of corner detection by Lowe's interest point detector which uses difference of Gaussian, matching by Scale Invariant Feature Transform (SIFT) descriptor, blunder detection by Random Sample Consensus (RANSAC) with fundamental matrix. They experimented with airborne imageries by bundle block adjustment and showed encouraging result. Since the relative orientation problem in this research was solved either by Least Squares or Kalman Smoothing, they were also reviewed as follows. Mikhail (1976) explained the aspects of Least Squares such as linear and nonlinear cases, general and special cases such as observation only and indirect observation, Least Squares with conditions and constraints, and unified approach to Least Squares adjustment. Welch and Bishop (1995) explained discrete Kalman filtering and extended Kalman filtering noting the importance of covariance matrix of measurement and prediction. They noted that as measurement error covariance matrix approaches to zero, the actual measurement is trusted more, while the predicted measurement is trusted less. As *a priori* prediction error covariance matrix approaches to zero, the predicted measurement is trusted more, and the actual measurement is trusted less. The text of Brown and Hwang (1997) provided the basic background theory of

Kalman Filtering and Smoothing. Nonlinear Kalman Filtering theory was well explained in the text and it is noted that parameter vectors in linear case has to be dealt as update values in nonlinear cases. Lee (1999) compared spline and first order gauss markov model to rectify HYDICE imagery. In the implementation of Gauss Markov process, six exterior orientation parameters were estimated sequentially using nonlinear Kalman Smoothing. Theiss (2000) implemented Kalman Smoothing to adjust video frame sensor model sequentially. His research showed the detailed information about photogrammetric application of Kalman Smoothing and the conducted experiments showed that Kalman Smoothing is more computationally efficient than the bundle adjustment.

## CHAPTER 3. THE DESCRIPTION OF EQUIPMENT AND DATA

### 3.1 Video Camera Equipment

Fryer (1996) defined Photogrammetry as “The science, and art, of determining the size and shape of objects as a consequence of analysing images recorded on film or electronic media” (p.1). The Frenchman Laussedat, who is considered as the father of close range photogrammetry, created a map of Paris in the 1850's with the photographs taken from the rooftops of Paris (Fryer, 1996). Silver halide film based camera was used as the sensor for many decades and the cathode ray tube was first used for electronic image capture imaging in 1923 (Theiss, 2000). Video camera technology has advanced dramatically with the now widespread of solid state image sensors such as the CCD (Charge Coupled Device) and CMOS (Complementary Metal Oxide Semiconductor). Such solid state sensors provide excellent geometric stability, good dynamic range, acceptable color response, and direct recording of digital image data.

Automatic relative orientation can be performed on any pair of frame images regardless of whether captured as still camera imagery or as frames from a video stream. However, it's difficult to take sequential image frames by a still



camera on a vehicle considering the need for reasonable and constant overlap. Therefore, a video camera was chosen as data acquisition instrument since by sampling selected frames, it can provide images with reasonable overlap. Although video cameras are still behind still camera technology in the view of resolution, a modern video camera such as a full high definition (HD) camcorder supports the resolution of up to  $1920 \times 1080$ . Most modern video camera uses a CCD or CMOS sensor. CCD and CMOS are different in the mechanisms of reading the signal, such that CMOS is composed of a MOS switch and a sensing line, while a CCD is composed of detector sites and CCD shift registers. They each have their own advantages and disadvantages, but a modern consumer camcorder with full HD resolution has proved to be reliable instrument for the suggested research.

SONY HDR CX 100 camcorder (Figure 3.1) used for data acquisition has a 0.2 inch CMOS sensor and records video in the format of MPEG4 AVC/H.264, which is one of the standards for video compression. The camcorder supports full HD which has ratio of 16:9. The lens type is Carl Zeiss Vario-Tessar which has a nominal focal length of 2.5-62.5 mm, diameter of 30 mm, and aperture range of F1.8-2.2. The video files can be accessed and captured by the software Picture Motion Browser (SONY, 2011), which has been developed by SONY. The software upsamples images to three megapixels ( $2304 \times 1296$ ) when capturing image frames from video. Any effect of upsampling will be handled by camera calibration.



Figure 3.1 SONY HDR CX 100 Camcorder

### 3.2 Video Data Description

The data for camcorder calibration were acquired at the University of Texas, Austin, and the Main building in the bell tower area was chosen for calibration because it has lot of three dimensional features and the building can be seen without any obstacles in front of it. The video was taken in superb weather conditions in the midday. 11 frames with diverse orientation angles at different positions were acquired to estimate the interior orientation parameters. These are the principal point offsets ( $x_0$ ,  $y_0$ ), the focal length (principal distance) ( $f$ ), radial distortion ( $K_1$ ,  $K_2$ ,  $K_3$ ) and tangential distortion ( $P_1$ ,  $P_2$ ). Since the equivalent vidicon tube diameter is 0.2 inch, the sensor diagonal was approximated by 2/3 of 0.2 inch. The inner orientation parameters will be carried

in pixel units, but the absolute dimensions in length units establish the conversion from pixels to millimeters. Considering the aspect ratio and absolute dimensions, the inner parameters were initially approximated as in table 3.1.

Table 3.1 Initial Approximation of Camera Calibration Parameters

Parameter	$x_0$ (pixel)	$y_0$ (pixel)	$f$ (pixel)	$k_1$	$k_2$	$k_3$	$p_1$	$p_2$
Initial (approximation)	0	0	2341.67	0	0	0	0	0

Also, additional videos of different calibration targets for camera calibration were taken inside the Geomatics lab in the Civil Engineering Building. This was done twice and eight images were captured at each session. The camera parameters estimated are the same as described above.

A terrestrial and an aerial video stream were taken for the strip formation experiment. For terrestrial data, the candidate criteria were as follows. For a building scene, the building should be horizontally long enough to take a lengthy series of photos. Also, the exterior of the building should have enough well defined points for unambiguous identification and measurement. Lastly, there should be no blocking object in the foreground of the scene because the camera parameters were calculated at the hyperfocal distance (infinity focus). It was found out that the Purdue ITAP License building satisfied the above criteria because it is long horizontally, the exterior material is brick which has lot of detailed points, and there were no parked cars or obstacles during the video

capture except for a few trees which are inevitable for many buildings. The car moved in constant velocity mode without any acceleration to make the speed of the car as constant as possible. Figure 3.2 shows drive path during terrestrial data acquisition.

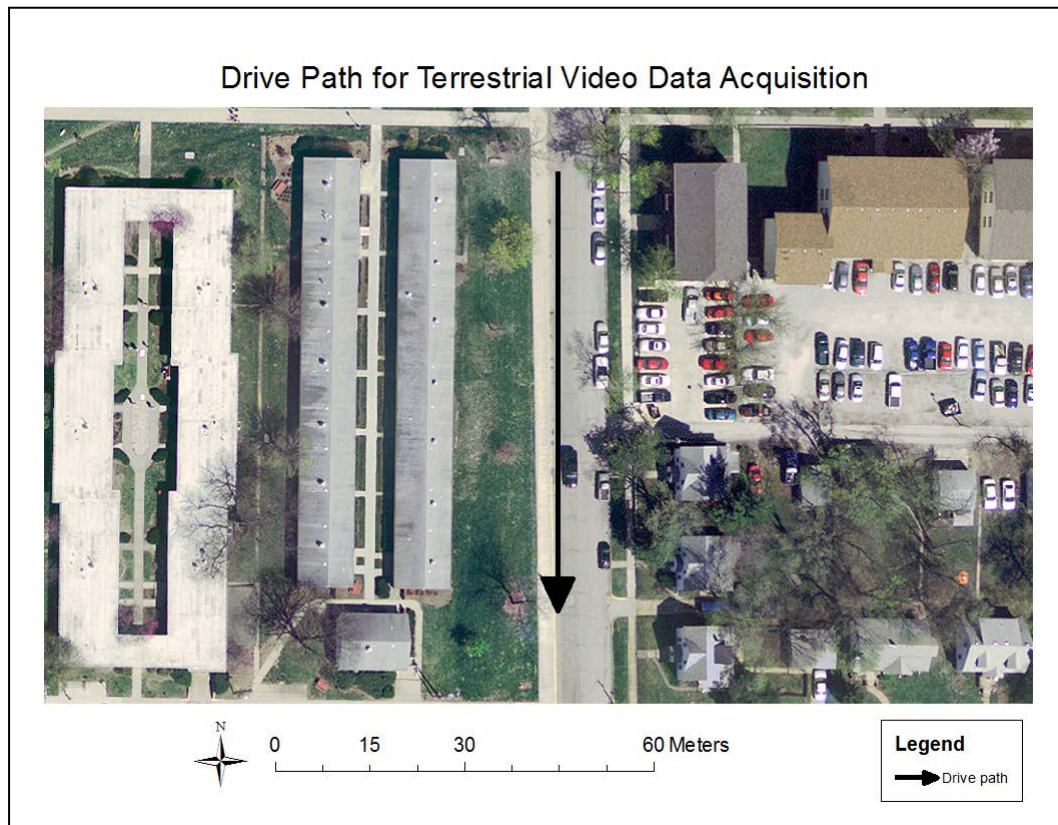


Figure 3.2 Drive Path for Terrestrial Video Data Acquisition

For aerial data, the candidate area was chosen considering the existence of abundant urban features such as buildings, roads and pavement. Also, the Purdue Airport traffic pattern was considered so that the data collection flight should not interfere with other aircraft traffic. Since the relative orientation results will be used for absolute orientation eventually as an absolute check on accuracy,

the existence of GPS control points for the candidate area was also considered. The Purdue University Campus, West Lafayette, IN, which fulfilled all of the above conditions, was chosen as the target area for the aerial data experiment.

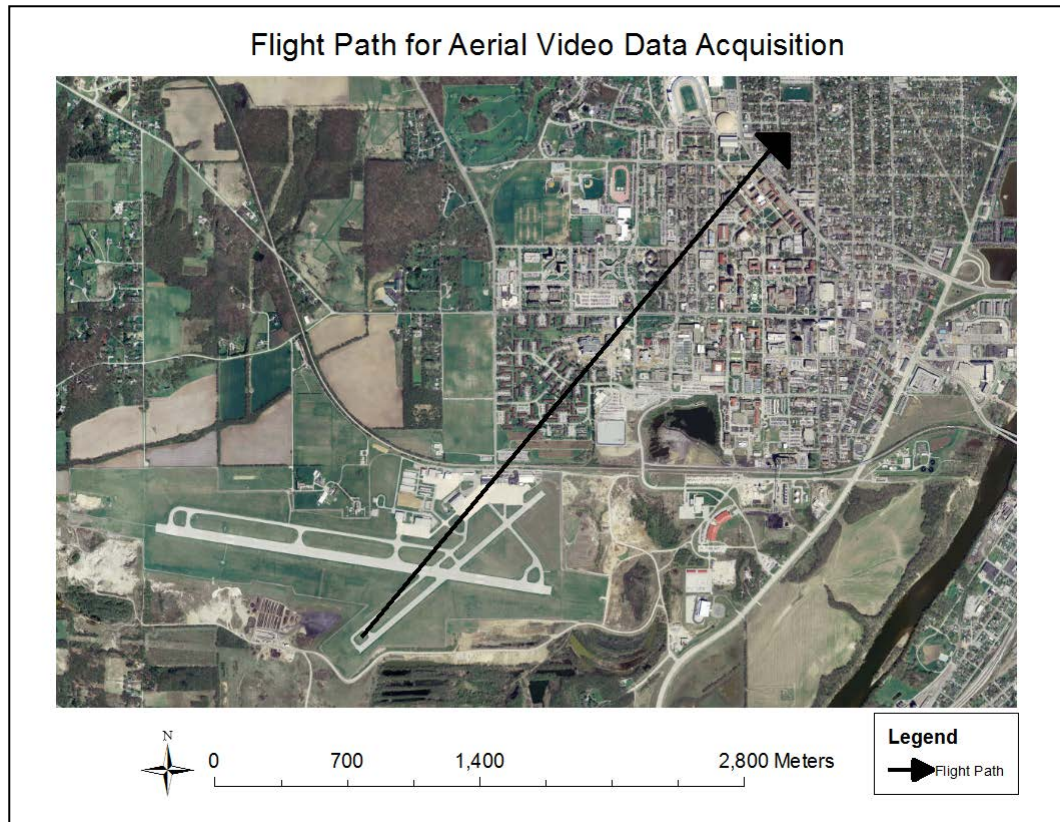


Figure 3.3 Flight Path for Aerial Video Data Acquisition

Figure 3.3 shows the flight path (black line) of the aircraft for the imagery collection. Video was taken in clear weather conditions with no snow on the ground. A High wing Cessna aircraft was used as the collection vehicle so that the scenes would not contain any part of the aircraft wings. The aircraft banked frequently during flight so that the data should be taken conveniently. The camera was held by hand, looking out through the opened passenger window.

The video was taken from taking off to landing and the most useful data was selected among whole dataset.

### 3.3 Control Point Acquisition by GPS Surveying

To assess the accuracy of the relative orientation results, and to get the results in the reference ground coordinate system, an absolute orientation procedure is required. To implement absolute orientation, we need control point information. Also, we will perform a bundle block adjustment with minimal constraints to compare with the results from relative and absolute orientation. We need control point information for all of these tasks. Further, we will divide the control points into two groups so that we can use one group as control points and another group as check points. This has the virtue of making the evaluation independent of the fitting process. We can implement two sets of experiments by exchanging the control and check points. Therefore, we need a sufficient number of control points on the images. There were existing control point datasets which were acquired by Real Time Kinematic (RTK) GPS surveying as shown by triangle with dot in Figure 3.4. These were collected using the recently implemented Indiana Real Time Network operated by the Indiana Department of Transportation. However, they were not uniformly distributed on the images and were not sufficient to use as both control and check points. Therefore, a new GPS survey was performed by both static and RTK with the equipment shown in figure 3.5. For static surveying, a minimum of 15 minutes were required for the recording time and it was shown later that 15 minutes were enough for an



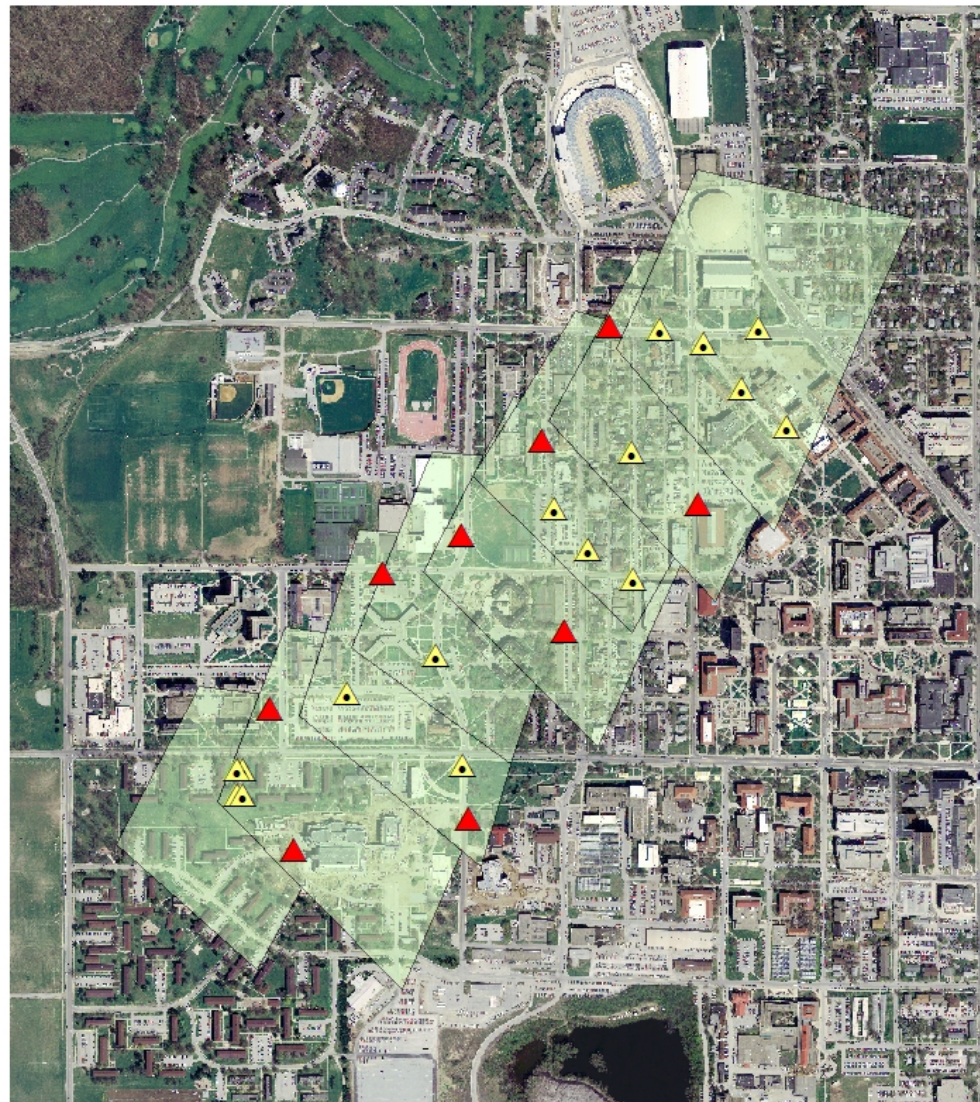
acceptable solution in this area. For the RTK survey, minimum of 3 minutes was required for the recording time. The static GPS surveying data were sent to the Online Positioning User Service (OPUS, National Geodetic Survey, 2012) maintained by National Geodetic Survey (NGS) of the National Oceanic and Atmospheric Administration (NOAA) and OPUS returned the position result and corresponding uncertainty. Typical one sigma precision of each coordinate component is 1-2 centimeter. This is possible using a dual frequency receiver and using the phase observable and corresponding mixed integer estimation to resolve the phase ambiguities. Six new control points were measured twice by static GPS surveying and three new control points were measured by both static and RTK GPS Surveying. Figure 3.6 shows the setup for each survey type and Table 3.2 shows the precision as standard deviations from the surveying result. The typical precision was about 1cm which is more than satisfactory to be used as control points for this project, where the nominal ground pixel size from the aerial (oblique) imagery is 1.69 meter (0.3 meter foreground, 3.0 meter background).

Table 3.2 The Precision of GPS Survey

	$\sigma_x$ (m)	$\sigma_y$ (m)	$\sigma_z$ (m)	type	$\sigma_x$ (m)	$\sigma_y$ (m)	$\sigma_z$ (m)	type
1	0.004	0.004	0.021	static	0.004	0.004	0.019	static
2	0.008	0.004	0.013	static	0.001	0	0.001	RTK
3	0.006	0.004	0.024	static	0.001	0.001	0.001	RTK
4	0.005	0.003	0.021	static	0.004	0.004	0.03	static
5	0.004	0.003	0.013	static	0.005	0.008	0.022	static
6	0.004	0.003	0.015	static	0.006	0.004	0.03	static
7	0.006	0.005	0.025	static	0.007	0.005	0.016	static
8	0.002	0.005	0.022	static	0.006	0.005	0.022	RTK
9	0.004	0.005	0.04	static	0.001	0.001	0.001	static



## GPS Surveying Plan



0 225 450 900 Meters

### Legend



-  new
-  existing

Figure 3.4 GPS Surveying Plan

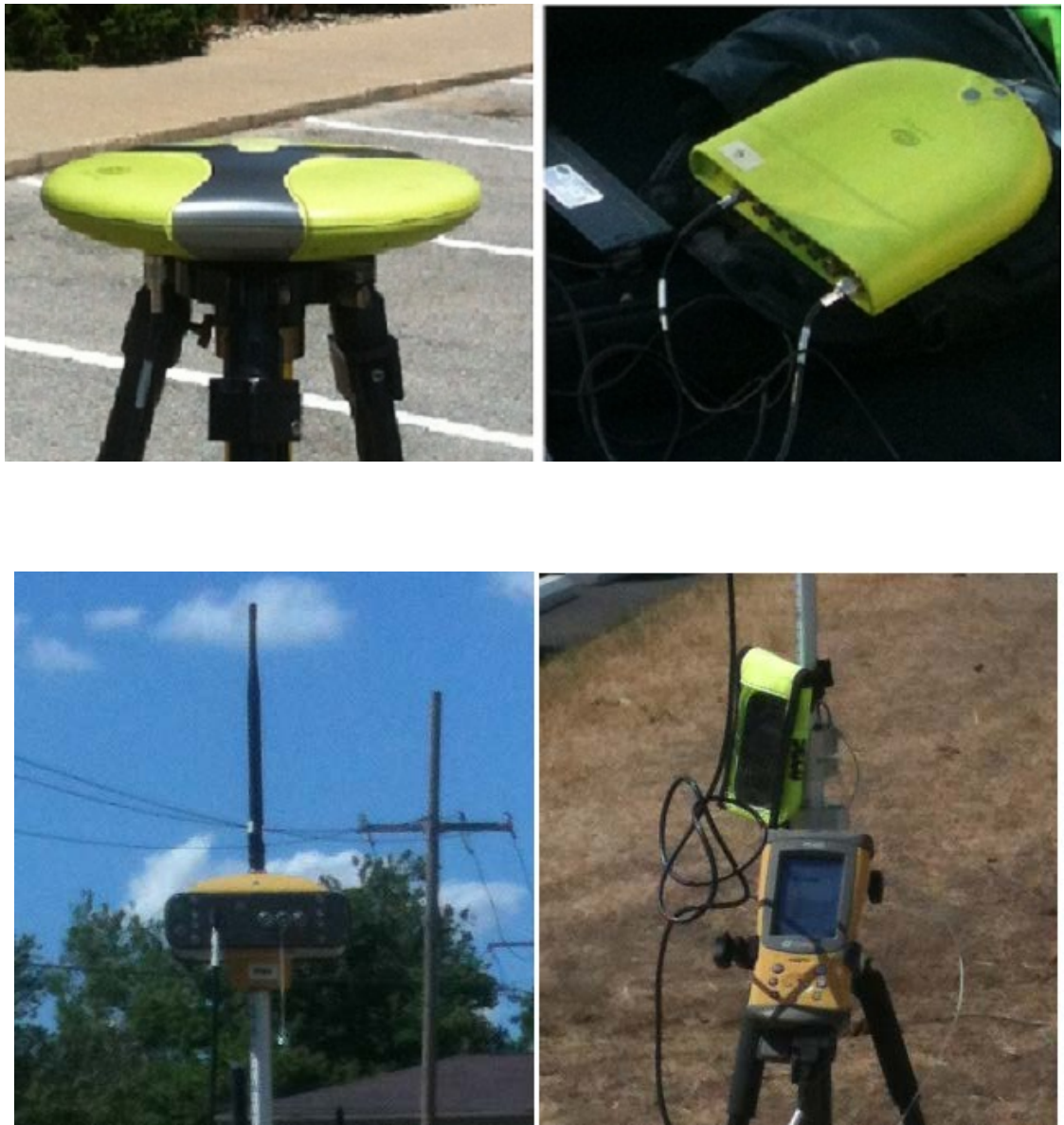


Figure 3.5 Top: Static GPS Antenna and Receiver. Bottom: RTK Receiver, Antenna, Data Collector, and Cellular Data Device





Figure 3.6 Static (Left) and RTK (Right) GPS Surveying

## CHAPTER 4. AUTOMATED RELATIVE ORIENTATION

### 4.1 Interest Point Detection

The first step of the relative orientation procedure is interest point detection. One of the most notable interest point detectors is the Harris corner detector (Harris et al, 1988), by which a number of other corner detectors were influenced. Förstner and Gulch (1987) independently developed virtually the same detector as Harris, at about the same time. Harris Corner detector procedure is described in equation (4.1) – equation (4.3).

$$\mathbf{M}_w = \begin{bmatrix} \sum_w (\mathbf{I}_x(x_i, y_i))^2 & \sum_w \mathbf{I}_x(x_i, y_i) \mathbf{I}_y(x_i, y_i) \\ \sum_w \mathbf{I}_x(x_i, y_i) \mathbf{I}_y(x_i, y_i) & \sum_w (\mathbf{I}_y(x_i, y_i))^2 \end{bmatrix} \quad (4.1)$$

Where  $\mathbf{I}_x$  and  $\mathbf{I}_y$  are defined below and  $\mathbf{I}$  represents the image inside the window,  $W$ .  $\mathbf{I}_x$  and  $\mathbf{I}_y$  represent the gradient in  $x$  and  $y$  directions as in equation (4.2).  $\mathbf{I}$  represents the image and  $W$  represents a window in the image.

$$\begin{aligned} \mathbf{I}_x &= \mathbf{I} \otimes [-1 \ 0 \ 1] \\ \mathbf{I}_y &= \mathbf{I} \otimes [-1 \ 0 \ 1]^T \end{aligned} \quad (4.2)$$

Let  $\lambda_1, \lambda_2$  be the eigenvalues of matrix  $\mathbf{M}$ . If both  $\lambda_1, \lambda_2$  are small, it means a flat region. If one is large and the other small, it means an edge. If both  $\lambda_1, \lambda_2$  are large, it means a corner. The cornerness metric can be defined as equation (4.3). We know that trace of a matrix is the sum of its eigenvalues, and the determinant is the product.

$$\text{Cornerness} = \det(\mathbf{M}) - k \text{trace}^2(\mathbf{M}) = \lambda_1 \lambda_2 - k(\lambda_1^2 + 2\lambda_1 \lambda_2 + \lambda_2^2) \quad (4.3)$$

Where  $\det(\mathbf{M})$  is the determinant of matrix  $\mathbf{M}$ ,  $\text{trace}(\mathbf{M})$  is the trace of matrix  $\mathbf{M}$ , and the value for  $k$  as used was 0.04, as per Bruce and Kornprobst (2009). The expression will be large when  $\lambda_1$  and  $\lambda_2$  are about the same size.

One of the drawbacks of the Harris corner detector is that it is not invariant to scale and the position of the corner will change as the scale changes. To detect the corners as consistently as possible, a more reliable, scale invariant corner detector was sought. Two most common kernels for achieving some degree of scale invariance are DoG (Difference of Gaussian) and LoG (Laplacian of Gaussian). DoG was suggested by Lowe (1999) and can be expressed as equation (4.4).

$$\text{DoG} = G(x, y, k\sigma_n) - G(x, y, \sigma_n) \quad (4.4)$$

Where  $G$  is

$$G(x, y, \sigma_n) = \frac{1}{2\pi\sigma_n^2} e^{-(x^2+y^2)/2\sigma_n^2} \quad (4.5)$$

And Mikolajczyk and Schmid (2001, 2004) expressed LoG as interest point detection kernel by equation (4.6).

$$LoG = \sigma_I^2 (L_{xx}(X, \sigma_I) + L_{yy}(X, \sigma_I)) \quad (4.6)$$

Where  $G$  is described in equation (4.5)

And Mikolajczyk and Schmid (2001, 2004) showed the Harris-Laplace Corner Detector algorithm, which uses LoG as characteristic scale criteria. The Harris Laplace Corner Detector Algorithm was chosen as the base platform for corner detector algorithm because it estimates cornerness measure of points which have maximum LoG through variant scales. In this research, we considered a color image which has red, green and blue bands. Therefore, the suggested step is different than the research of Mikolajczyk and Schmid (2004) in the view of handling multi bands. The suggested algorithm consists of two steps. The first step is the multi-scale corner detection and the second step is an iterative selection of the characteristic scale and the cornerness measure of the corner points. The first step is described as follows.

a) Decide the integration scale and differentiation scale as equation (4.7) and (4.8). The integration scale determines current scale where Harris points are detected and differentiation scale determines search space for corner.

$$\text{If } (n = 1), \sigma_{I(1)} = 1.5, \sigma_{D(1)} = 0.7\sigma_{I(1)} \quad (4.7)$$

$$\text{If } (n > 1), \sigma_{D(n)} = 1.2^{n-1}\sigma_{D(n-1)}, \sigma_{I(n)} = \frac{\sigma_{D(n)}}{0.7} \quad (4.8)$$

b) Calculate  $\mathbf{L}_x(X, \sigma_D), \mathbf{L}_y(X, \sigma_D)$  for each band of image by Gaussian Kernel with scale  $\sigma_D$ . First, set the size of windows as equation (4.9).

$$\mathbf{x} = [\text{int}(-3\sigma_D) : \text{int}(3\sigma_D)] \quad (4.9)$$

Then, create Gaussian derivative masks as equation (4.10) and (4.11).

$$\mathbf{dx} = \mathbf{x} \times \frac{1}{\sqrt{2\pi}\sigma_D^3} e^{-\mathbf{x}^2 / 2\sigma_D^2} \quad (4.10)$$

$$\mathbf{dy} = \mathbf{dx}^T \quad (4.11)$$

Then implement convolution to each band of images as equation (4.12) and (4.13).

$$L_x(X, \sigma_D) = I * \mathbf{dx} \quad (4.12)$$

$$L_y(X, \sigma_D) = I * \mathbf{dy} \quad (4.13)$$

c) Calculate second moment matrix of color image. Mikolajczyk and Schmid (2004) defined second moment matrix for monochrome image as equation (4.14).

$$\mu(X, \sigma_I, \sigma_D) = \sigma_D^2 g(\sigma_I) * \begin{bmatrix} \mathbf{L}_x^2(X, \sigma_D) & \mathbf{L}_x \mathbf{L}_y(X, \sigma_D) \\ \mathbf{L}_x \mathbf{L}_y(X, \sigma_D) & \mathbf{L}_y^2(X, \sigma_D) \end{bmatrix} \quad (4.14)$$

Stöttinger (2007) described the second moment matrix for the colored image as equation (4.15) and it was used as the second moment matrix for cornerness measure in this research.

$$\mu(X, \sigma_I, \sigma_D) = \sigma_D^2 G(\sigma_I) * \begin{bmatrix} \mathbf{R}_x^2 + \mathbf{G}_x^2 + \mathbf{B}_x^2 & \mathbf{R}_x \mathbf{R}_y + \mathbf{G}_x \mathbf{G}_y + \mathbf{B}_x \mathbf{B}_y \\ \mathbf{R}_x \mathbf{R}_y + \mathbf{G}_x \mathbf{G}_y + \mathbf{B}_x \mathbf{B}_y & \mathbf{R}_y^2 + \mathbf{G}_y^2 + \mathbf{B}_y^2 \end{bmatrix} \quad (4.15)$$

To implement equation (4.15), set the window size as equation (4.16)

$$W = 6\sigma_I + 1 \quad (4.16)$$

Then implement convolution by the Gaussian filter with above size and standard deviation  $\sigma_I$ . For example, the [1,1] element of  $\mu(X, \sigma_I, \sigma_D)$  can be estimated as equation (4.17).



$$\mu(X, \sigma_I, \sigma_D)_{(1,1)} = \sigma_D^2 g(\sigma_I) * (\mathbf{R}_x^2 + \mathbf{G}_x^2 + \mathbf{B}_x^2) \quad (4.17)$$

d) Calculate the cornerness metric by equation (4.18) and choose points which have cornerness larger than the given threshold.

$$\text{cornerness} = \det(\mu(X, \sigma_I, \sigma_D)) - k \times \text{trace}^2(\mu(X, \sigma_I, \sigma_D)) \quad (4.18)$$

The procedure for corner detection was shown from a) to d) as the first step. The locations of the corner points are decided only in the first scale. The second step from e) to h) is composed of the calculation of the LoG of image at each scale and the verification of maximum LoG attainment and decision of cornerness measure for each detected point.

e) For each corner from d), calculate the LoG for each point as equation (4.15). To implement equation (4.15), we created rotationally symmetric Laplacian of Gaussian filter of size of equation (4.15) with standard deviation  $\sigma_I$ . Then, we filtered each band of image with created LoG filter. The LoG of entire band was calculated as equation (4.19)

$$LoG = \sum_i^{R,G,B} LoG_i \quad (4.19)$$

f) If  $n=1$ , calculate  $LoG_{n+1}$  and compare with  $LoG_n$  of each detected point. If  $LoG_n$  is larger, then we keep this cornerness measure estimated in this scale.

g) If  $1 < n < N_{\max}$  (maximum number of step), calculate  $LoG_{n-1}$ ,  $LoG_{n+1}$  and compare with  $LoG_n$  of each point. If  $LoG$  of certain scale is the largest, then we keep the cornerness measure from this scale.

h) Go to a) and increase  $n$  by 1 and repeat a) – g) until  $n = N_{\max}$

i) Finally each point has a cornerness measure estimated in characteristic scale where points have maximum  $LoG$ .

#### 4.2 Matching by Cross Correlation & RANSAC

According to Gonzalez, Woods and Eddins (2004), the best match of  $w(x,y)$  in  $f(x,y)$  is the location of the maximum value in the resulting correlation image when we treat  $w(x,y)$  as a spatial filter and compute the sum of products (or a normalized version of it) for each location of  $w$  in  $f$ . Therefore, we created  $n$  by  $n$  pixel windows for each corner in the first image in the sequence, then computed the correlation at each point in the second image, and extracted maximum values in both directions from and to the second image. The correlation at a point can be computed as equation (4.20),

$$c(u, v) = \frac{\sum (u_i - \bar{u}) \times (v_i - \bar{v})}{\left[ \sum (u_i - \bar{u})^2 \times \sum (v_i - \bar{v})^2 \right]^{\frac{1}{2}}} \quad (4.20)$$

Where  $c$  is the correlation,  $u$  and  $v$  are a digital number (0-255 for 16 bit image) of each pixel.

The cross correlation was implemented in both ways (left image to right image, then right image to left image) and a pair of points in the first and the second image which have the largest cross correlation in both ways were decided as the matched points. As O'Neill and Denos (1996) outlined, image pyramids were created for  $n$  steps by downsampling image by  $2^{n-1}$  to make cross correlation matching more robust. Then, matching by cross correlation was implemented  $n$  times to minimize false matching. Next, the points which survived multi-scale cross correlation matching were decided. However, it was found out that there were still falsely matched interest points between two images, and those falsely matched points were removed by Random Sample Consensus (RANSAC). RANSAC was developed as a paradigm for fitting a model to experimental data to detect inliers and outliers (Fischler & Bolles, 1981). By iterating  $N$  times, the parameters of the model are estimated by randomly picked minimum data, and the best model is chosen as giving the most inliers within the threshold. The iteration number  $N$  is described as equation (4.21).

$$N = \frac{\log(1-p)}{\log(1-(1-e)^s)} \quad (4.21)$$

Where  $e$  is the probability that a point is an outlier,  $S$  is the number of points in a sample,  $N$  is the number of iterations, and  $p$  is the desired probability in a good sample.

The model for RANSAC is the coplanarity condition expressed as essential matrix, which is described in chapter 4.3. By randomly selecting eight pairs of points, the parameters of the essential matrix can be calculated by equation (4.38) at each iteration. We can find the essential matrix which gives the most number of inliers given threshold  $t$  such as equation (4.22).

$$\begin{bmatrix} u & v & 1 \end{bmatrix}_1 \mathbf{E}_{12} \begin{bmatrix} u \\ v \\ 1 \end{bmatrix}_2 < t \quad (4.22)$$

Where  $u = \frac{x - x_0 + (x - x_0)(K_1 r^2 + K_2 r^4 + K_3 r^6) + P_1(r^2 + 2(x - x_0)^2) + 2P_2(x - x_0)(y - y_0)}{-f}$  and

$v = \frac{y - y_0 + (y - y_0)(K_1 r^2 + K_2 r^4 + K_3 r^6) + P_2(r^2 + 2(y - y_0)^2) + 2P_1(x - x_0)(y - y_0)}{-f}$ , which will be

explained in section 4.5.

Then outliers which do not satisfy equation (4.22) were removed and the only inliers were determined as final matched points. The inliers were input to following relative orientation algorithm.

### 4.3 Relative Orientation by Eight Point Algorithm

The exterior orientation parameters ( $\omega, \varphi, \kappa, b_x, b_y, b_z$ ) can be estimated by the eight point algorithm (Theiss, 2000) with the essential matrix (E). Given two vectors of  $a$  and  $b$ ,

$$\vec{a} = \begin{bmatrix} \mathbf{a}_x \\ \mathbf{a}_y \\ \mathbf{a}_z \end{bmatrix} \text{ and } \vec{b} = \begin{bmatrix} \mathbf{b}_x \\ \mathbf{b}_y \\ \mathbf{b}_z \end{bmatrix} \quad (4.23)$$

If we arrange the elements of  $\vec{b}$  into skew-symmetric matrix,

$$\mathbf{K} = \begin{bmatrix} \mathbf{0} & -\mathbf{b}_z & \mathbf{b}_y \\ \mathbf{b}_z & \mathbf{0} & -\mathbf{b}_x \\ -\mathbf{b}_y & \mathbf{b}_x & \mathbf{0} \end{bmatrix} \quad (4.24)$$

$$\vec{b} \times \vec{a} = \mathbf{K}\vec{a} \quad (4.25)$$

The collinearity equation is,

$$\mathbf{M} \begin{bmatrix} X - X_L \\ Y - Y_L \\ Z - Z_L \end{bmatrix} = \frac{1}{k} \begin{bmatrix} x - x_0 \\ y - y_0 \\ -f \end{bmatrix} = \frac{1}{k} \begin{bmatrix} 1 & 0 & -x_0 \\ 0 & 1 & -y_0 \\ 0 & 0 & -f \end{bmatrix} \begin{bmatrix} x \\ y \\ 1 \end{bmatrix} = \frac{1}{k} \mathbf{C} \begin{bmatrix} x \\ y \\ 1 \end{bmatrix} \quad (4.26)$$

Where  $X_L, Y_L, Z_L$  are location of the camera in the ground coordinate system,  $x_0, y_0, f$  are principal point offset and focal length,  $k$  is scale factor, and  $\mathbf{M}$  is the rotation matrix of the camera such as equation (4.27).

$$\mathbf{M} = \begin{bmatrix} \cos \phi \cos \kappa & \cos \omega \sin \kappa + \sin \omega \sin \phi \cos \kappa & \sin \omega \sin \kappa - \cos \omega \sin \phi \cos \kappa \\ -\cos \phi \sin \kappa & \cos \omega \cos \kappa - \sin \omega \sin \phi \sin \kappa & \sin \omega \cos \kappa + \cos \omega \sin \phi \sin \kappa \\ \sin \phi & -\sin \omega \cos \phi & \cos \omega \cos \phi \end{bmatrix} \quad (4.27)$$

Where  $\omega, \phi, \kappa$  is the rotation about  $X, Y$ , and  $Z$  axis.

Therefore from equation (4.26),

$$\mathbf{a} = \begin{bmatrix} X - X_L \\ Y - Y_L \\ Z - Z_L \end{bmatrix} = \frac{1}{k} \mathbf{M}^T \mathbf{C} \begin{bmatrix} x \\ y \\ 1 \end{bmatrix} \quad (4.28)$$

The coplanarity condition between  $\vec{\mathbf{a}}_1$  and  $\vec{\mathbf{a}}_2$  is

$$\vec{\mathbf{b}} \cdot (\vec{\mathbf{a}}_1 \times \vec{\mathbf{a}}_2) = 0 \quad (4.29)$$

$$\vec{\mathbf{a}}_1 \cdot \vec{\mathbf{b}} \times \vec{\mathbf{a}}_2 = 0 \quad (4.30)$$

$$\therefore \vec{\mathbf{a}}_1^T \mathbf{K}_b \vec{\mathbf{a}}_2 = 0 \quad (4.31)$$

$$\therefore \frac{1}{k_1} \frac{1}{k_2} [x_1 \quad y_1 \quad 1] \mathbf{C}_1^T \mathbf{M}_1 \mathbf{K}_b \mathbf{M}_2^T \mathbf{C}_2 \begin{bmatrix} x_2 \\ y_2 \\ 1 \end{bmatrix} = 0 \quad (4.32)$$

Where  $\mathbf{K}_b$  is equivalent with  $\mathbf{K}$  in equation (4.24).

$$\therefore [x_1 \quad y_1 \quad 1] \mathbf{C}_1^T \mathbf{E} \mathbf{C}_2 \begin{bmatrix} x_2 \\ y_2 \\ 1 \end{bmatrix} = 0 \quad (4.33)$$

Where  $\mathbf{E} = \mathbf{M}_1 \mathbf{K}_b \mathbf{M}_2^T$ .

$$\therefore [x_1 - x_{0_1} \quad y_1 - y_{0_1} \quad -f_1] \mathbf{E} \begin{bmatrix} x_2 - x_{0_2} \\ y_2 - y_{0_2} \\ -f_1 \end{bmatrix} = 0 \quad (4.34)$$

The matrix  $\mathbf{E} = \mathbf{M}_1 \mathbf{K}_b \mathbf{M}_2^T$  is called the essential matrix. The fundamental matrix can be computed as

$$\mathbf{F} = \mathbf{C}_1^T \mathbf{M}_1 \mathbf{K}_b \mathbf{M}_2^T \mathbf{C}_2 \quad (4.35)$$

Then coplanarity condition becomes,

$$\begin{bmatrix} x_1 & y_1 & 1 \end{bmatrix} \mathbf{F} \begin{bmatrix} x_2 \\ y_2 \\ 1 \end{bmatrix} = 0 \quad (4.36)$$

And

$$\begin{bmatrix} u & v & 1 \end{bmatrix}_1 \mathbf{E}_{12} \begin{bmatrix} u \\ v \\ 1 \end{bmatrix}_2 = 0 \quad (4.37)$$

Where  $\mathbf{E}_{ij}$  is the essential matrix defined by image i and j  $u = \frac{x - x_0}{c}, v = \frac{y - y_0}{c}$ .

Therefore,

$$F = (u_1 e_{11} + v_1 e_{21} + e_{31})u_2 + (u_1 e_{12} + v_1 e_{22} + e_{32})v_2 + (u_1 e_{13} + v_1 e_{23} + 1) = 0 \quad (4.38)$$

Where  $e_{ij}$  is the  $(i,j)^{\text{th}}$  element of the essential matrix.

And equation (4.38) is equivalent to equation (4.39).



$$\begin{bmatrix} u_1 u_2 & u_1 v_2 & u_1 & v_1 u_2 & v_1 v_2 & v_1 & u_2 & v_2 \end{bmatrix}_i \begin{bmatrix} e_{11} \\ e_{12} \\ e_{13} \\ e_{21} \\ e_{22} \\ e_{23} \\ e_{31} \\ e_{32} \end{bmatrix} = [-1] \quad (4.39)$$

Since there are eight parameters in equation (4.39), eight observations give a unique solution to the essential matrix. According to Horn (1990), the baseline elements can be computed from equation (4.40) and the rotation elements can be computed from equation (4.41).

$$\mathbf{b}\mathbf{b}^T = \frac{1}{2} \text{Trace}(\mathbf{E}\mathbf{E}^T) \mathbf{I} - \mathbf{E}\mathbf{E}^T \quad (4.40)$$

Where  $\mathbf{b} = [b_x \ b_y \ b_z]^T$ .

$$(\mathbf{b} \cdot \mathbf{b})\mathbf{R} = \text{Cofactors}(\mathbf{E})^T - \mathbf{B}\mathbf{E} \quad (4.41)$$

Where  $\mathbf{B}$  is equivalent to  $\mathbf{K}$  in equation (4.24) and  $\mathbf{R}$  is the rotation matrix equivalent to  $\mathbf{M}$  in equation (4.27).

Although the eight point algorithm is simple and straightforward, it gives multiple solutions and it is not as robust as least squares adjustment of coplanarity equation because of the small number of points. However, it could be used as an initial approximation of parameters for camera calibration by geometric reasoning and confirming by convergence and iteration number check.

#### 4.4 Relative Orientation by Coplanarity and Scale Restraint Conditions

The relative orientation by coplanarity and scale restraint conditions can be explained as follows.

The baseline vector is

$$\vec{\mathbf{b}} = \begin{bmatrix} \mathbf{b}_x \\ \mathbf{b}_y \\ \mathbf{b}_z \end{bmatrix} = \begin{bmatrix} X_{L_2} - X_{L_1} \\ Y_{L_2} - Y_{L_1} \\ Z_{L_2} - Z_{L_1} \end{bmatrix} \quad (4.42)$$

And for the image space coordinate for each pair of image,

$$\vec{\mathbf{a}}_1 = \begin{bmatrix} u_1 \\ v_1 \\ w_1 \end{bmatrix} = \mathbf{M}_1^T \begin{bmatrix} \bar{x} \\ \bar{y} \\ -f \end{bmatrix}_1, \quad \vec{\mathbf{a}}_2 = \begin{bmatrix} u_2 \\ v_2 \\ w_2 \end{bmatrix} = \mathbf{M}_2^T \begin{bmatrix} \bar{x} \\ \bar{y} \\ -f \end{bmatrix}_2 \quad (4.43)$$

Where  $\bar{x} = x - x_0 + (x - x_0)(K_1 r^2 + K_2 r^4 + K_3 r^6) + P_1(r^2 + 2(x - x_0)^2) + 2P_2(x - x_0)(y - y_0)$  and

$$\bar{y} = y - y_0 + (y - y_0)(K_1 r^2 + K_2 r^4 + K_3 r^6) + P_2(r^2 + 2(y - y_0)^2) + 2P_1(x - x_0)(y - y_0)$$

Then, coplanarity condition becomes equivalent to equation (4.44)

$$\mathbf{F} = \begin{vmatrix} \mathbf{b}_x & \mathbf{b}_y & \mathbf{b}_z \\ \mathbf{u}_1 & \mathbf{v}_1 & \mathbf{w}_1 \\ \mathbf{u}_2 & \mathbf{v}_2 & \mathbf{w}_2 \end{vmatrix} = 0 \quad (4.44)$$

For the first model, we can fix one ( $b_x$ ) of six exterior orientation parameters and unknown parameters are five ( $b_y, b_z, \omega, \phi, \kappa$ ). Equation (4.44) can be solved by the General Least Squares approach, whose condition equation is the form of

$$\mathbf{A}\mathbf{v} + \mathbf{B}\mathbf{\Delta} = \mathbf{f} \quad (4.45)$$

and

$$\mathbf{A} = [\partial\mathbf{F}/\partial\mathbf{x}_1 \quad \partial\mathbf{F}/\partial\mathbf{y}_1 \quad \partial\mathbf{F}/\partial\mathbf{x}_2 \quad \partial\mathbf{F}/\partial\mathbf{y}_2] \quad (4.46)$$

Where  $\mathbf{x}_1, \mathbf{y}_1, \mathbf{x}_2, \mathbf{y}_2$  are the coordinates of corresponding points in a pair of images.

$$\mathbf{B} = \begin{bmatrix} \frac{\partial\mathbf{F}}{\partial\mathbf{b}_y} & \frac{\partial\mathbf{F}}{\partial\mathbf{b}_z} & \frac{\partial\mathbf{F}}{\partial\omega} & \frac{\partial\mathbf{F}}{\partial\phi} & \frac{\partial\mathbf{F}}{\partial\kappa} \end{bmatrix} \quad (4.47)$$

$$\mathbf{f} = -\mathbf{F}_0 = - \begin{vmatrix} \mathbf{b}_x & \mathbf{b}_y & \mathbf{b}_z \\ \mathbf{u}_1 & \mathbf{v}_1 & \mathbf{w}_1 \\ \mathbf{u}_2 & \mathbf{v}_2 & \mathbf{w}_2 \end{vmatrix} \quad (4.48)$$

Where  $\mathbf{v}$  is the residual vector for  $\mathbf{x}_1, \mathbf{y}_1, \mathbf{x}_2, \mathbf{y}_2$  and  $\Delta$  is the corrections to the parameters.

From the second pair of images, we have to include the scale restraint equation for at least one point and the number of unknown parameters becomes six including  $b_x$ . For three image rays vectors (equation (4.49) – equation (4.51)), the three ray intersection condition becomes equation (4.53).

$$\bar{\mathbf{a}}_1 = \begin{bmatrix} a_{1x} \\ a_{1y} \\ a_{1z} \end{bmatrix} = \mathbf{M}_1^T \begin{bmatrix} \bar{x} \\ \bar{y} \\ -f \end{bmatrix} \quad (4.49)$$

$$\bar{\mathbf{a}}_2 = \begin{bmatrix} a_{2x} \\ a_{2y} \\ a_{2z} \end{bmatrix} = \mathbf{M}_2^T \begin{bmatrix} \bar{x} \\ \bar{y} \\ -f \end{bmatrix} \quad (4.50)$$

$$\bar{\mathbf{a}}_3 = \begin{bmatrix} a_{3x} \\ a_{3y} \\ a_{3z} \end{bmatrix} = \mathbf{M}_3^T \begin{bmatrix} \bar{x} \\ \bar{y} \\ -f \end{bmatrix} \quad (4.51)$$

$$\bar{\mathbf{d}}_1 = \bar{\mathbf{a}}_1 \times \bar{\mathbf{a}}_2$$

$$\bar{\mathbf{d}}_2 = \bar{\mathbf{a}}_2 \times \bar{\mathbf{a}}_3 \quad (4.52)$$

$$\mathbf{f} = \frac{\begin{vmatrix} \mathbf{a}_{1x} & \mathbf{d}_{1x} & \mathbf{b}_{1x} \\ \mathbf{a}_{1y} & \mathbf{d}_{1y} & \mathbf{b}_{1y} \\ \mathbf{a}_{1z} & \mathbf{d}_{1z} & \mathbf{b}_{1z} \end{vmatrix}}{\begin{vmatrix} \mathbf{a}_{1x} & \mathbf{d}_{1x} & \mathbf{a}_{2x} \\ \mathbf{a}_{1y} & \mathbf{d}_{1y} & \mathbf{a}_{2y} \\ \mathbf{a}_{1z} & \mathbf{d}_{1z} & \mathbf{a}_{2z} \end{vmatrix}} + \frac{\begin{vmatrix} \mathbf{b}_{2x} & \mathbf{d}_{2x} & \mathbf{a}_{3x} \\ \mathbf{b}_{2y} & \mathbf{d}_{2y} & \mathbf{a}_{3y} \\ \mathbf{b}_{2z} & \mathbf{d}_{2z} & \mathbf{a}_{3z} \end{vmatrix}}{\begin{vmatrix} \mathbf{a}_{2x} & \mathbf{d}_{2x} & \mathbf{a}_{3x} \\ \mathbf{a}_{2y} & \mathbf{d}_{2y} & \mathbf{a}_{3y} \\ \mathbf{a}_{2z} & \mathbf{d}_{2z} & \mathbf{a}_{3z} \end{vmatrix}} = 0 \quad (4.53)$$

To compose condition equation,

$$\mathbf{a} = \text{Jacobian}(\mathbf{f}, \mathbf{l})$$

$$\mathbf{b} = \text{Jacobian}(\mathbf{f}, \mathbf{\Delta}) \quad (4.54)$$

Where  $\mathbf{l}$  is the vector of observations,  $\mathbf{\Delta}$  is the vector of parameters.

The scale restraint equation can also be expressed in computer vision terminology. According to Forsyth and Ponce (2011), the minimum distance between the rays  $R_1$ ,  $R_2$  and  $R_3$  is reached at the points  $P_1$ ,  $P_2$  and  $P_3$  so that the line joining each point is perpendicular to  $R_1$ ,  $R_2$  and  $R_3$  if they do not intersect as shown as equation (4.55).

$$\overrightarrow{O_1 P_1} = z_1^i \overrightarrow{O_1 p_1} = \overrightarrow{O_1 O_i} + z_i \overrightarrow{O_i p_i} + \lambda_i (\overrightarrow{O_1 p_1} \times \overrightarrow{O_i p_i}) \text{ for } i = 2, 3 \quad (4.55)$$

If cameras are calibrated and the projection matrices of the second and the third cameras are  $(R_2^T - R_2^T t_2)$  and  $(R_3^T - R_3^T t_3)$ , equation (4.55) can be expressed in the first camera's coordinate system as equation (4.56).

$$z_1^i = t_i + z_i R_i p_i + \lambda_i (p_1 \times R_i p_i) \text{ for } i = 2, 3. \quad (4.56)$$

Then, the scale restraint condition can be expressed as  $z_1^2 = z_1^3$ .

And the condition equation becomes equation (4.57). Equation (4.57) will be explained in section 5.1 in more detail. Equation (4.57) is solved by nonlinear General Least Squares method from equation (4.58) to equation (4.65).

$$\mathbf{A}\mathbf{v} + \mathbf{B}\mathbf{\Delta} = \mathbf{f}$$

$$\begin{bmatrix} \mathbf{A}_1 & & & & & \\ & \mathbf{A}_2 & & & & \\ & & \mathbf{a}_2 & & & \\ & & & \mathbf{I} & & \\ & & & & \mathbf{A}_3 & \\ & & & & & \mathbf{a}_3 \\ & & & & & & \mathbf{I} \\ & & & & & & & \ddots \\ & & & & & & & & \mathbf{A}_n \\ & & & & & & & & & \mathbf{a}_n \end{bmatrix} \mathbf{V} + \begin{bmatrix} \mathbf{B}_1 & & & & & \\ & \mathbf{B}_2 & & & & \\ & & \mathbf{b}_2 & & & \\ & & & -\Phi & & \\ & & & & \mathbf{I} & \\ & & & & & \mathbf{B}_3 \\ & & & & & & \mathbf{b}_3 \\ & & & & & & & -\Phi \\ & & & & & & & & \mathbf{I} \\ & & & & & & & & & \vdots \\ & & & & & & & & & & \mathbf{B}_n \\ & & & & & & & & & & & \mathbf{b}_n \end{bmatrix} \begin{bmatrix} \Delta_1 \\ \Delta_2 \\ \Delta_3 \\ \vdots \\ \Delta_n \end{bmatrix} = \begin{bmatrix} \mathbf{F}_1 \\ \mathbf{F}_2 \\ \mathbf{f}_2 \\ \mathbf{0} \\ \mathbf{F}_3 \\ \mathbf{f}_3 \\ \mathbf{0} \\ \vdots \\ \mathbf{F}_n \\ \mathbf{f}_n \end{bmatrix} \quad (4.57)$$

Where  $\mathbf{A}$ ,  $\mathbf{B}$ , and  $\mathbf{F}$  are the matrix presented in coplanarity condition.  $\mathbf{a}$ ,  $\mathbf{b}$  and  $\mathbf{f}$  are the matrix presented in scale restraint condition.  $\Phi$  is the state transition matrix.  $\mathbf{V}$  is residual vector and  $\mathbf{\Delta}$  is parameter vectors

$$\mathbf{Q} = \frac{1}{\sigma_0^2} \mathbf{\Sigma} \quad (4.58)$$

Where  $\mathbf{Q}$  is cofactor matrix,  $\mathbf{\Sigma}$  is covariance matrix and  $\sigma_0$  is the reference standard deviation. We assumed one pixel of variance of each observation and  $\mathbf{\Sigma}$  became the identity matrix.

Then, the equivalent cofactor matrix is

$$\mathbf{Q}_e = \mathbf{A} \mathbf{Q} \mathbf{A}^T \quad (4.59)$$

Then normal equation becomes equation (4.60).

$$\mathbf{N} = \mathbf{B}^T \mathbf{Q}_e^{-1} \mathbf{B} = \mathbf{B}^T \mathbf{W}_e \mathbf{B} \quad (4.60)$$

$$\mathbf{t} = \mathbf{B}^T \mathbf{W}_e \mathbf{f} \quad (4.61)$$

Then update to the parameter becomes equation (4.62).

$$\mathbf{\Delta} = \mathbf{N}^{-1} \mathbf{t} \quad (4.62)$$

The residual can be calculated by equation (4.63).

$$\mathbf{v} = \mathbf{Q}\mathbf{A}^T \mathbf{W}_e (\mathbf{f} - \mathbf{B}\Delta) \quad (4.63)$$

The observations and parameters can be updated like equation (4.64)

$$\hat{\mathbf{l}} = \mathbf{l} + \mathbf{v}, \mathbf{X}^0 = \mathbf{X}^0 + \Delta \quad (4.64)$$

And the objective function is like equation (4.65).

$$\varphi = \mathbf{v}^T \mathbf{W} \mathbf{v} \quad (4.65)$$

#### 4.5 Camera Calibration

In this research, the camera was calibrated by the Unified Least Squares approach with initial approximation by relative orientation algorithm. The exterior orientation parameters of each image and the object space coordinate of target points and camera parameters such as principal point offset  $(x_0, y_0)$ , focal length  $(f)$ , radial lens distortion  $(K_1, K_2, K_3)$ , and tangential lens distortion  $(P_1, P_2)$  were carried as parameters. The initial approximations of camera parameters were chosen as nominal values. However, the exterior orientation parameters and object space coordinate couldn't be estimated by simple relative orientation with the fixed value of  $b_x$  and the zero initial approximation of the rest of parameters since the image was rotated by a large amount of angles. Therefore, an eight



point algorithm was applied to get the initial approximation of exterior orientation parameters for relative orientation.

Four possible sets of exterior orientation were calculated by the eight point algorithm between each image pair and their ambiguity was resolved by geometric reasoning. Once exterior orientations are initially approximated, they were confirmed by nonlinear estimation in the conventional relative orientation algorithm with General Least Squares. Now, we have the initial approximation of exterior orientation parameters for calibration. Since we know the initial approximation of interior orientations and exterior orientations, we can initially approximate model space coordinate of each measured points in the first pair of stereo images by intersection from equation (4.66) – (4.67).

$$X - X_L = (Z - Z_L) \frac{m_{11}(x - x_0) + m_{21}(y - y_0) + m_{31}(-f)}{m_{13}(x - x_0) + m_{23}(y - y_0) + m_{33}(-f)} \quad (4.66)$$

$$Y - Y_L = (Z - Z_L) \frac{m_{12}(x - x_0) + m_{22}(y - y_0) + m_{32}(-f)}{m_{13}(x - x_0) + m_{23}(y - y_0) + m_{33}(-f)} \quad (4.67)$$

Where  $(X_L, Y_L, Z_L)$  is the local origin of object space coordinates at the perspective center,  $m_{ij}$  is the  $(i, j)$  element of rotation matrix,  $(x_0, y_0)$  is the principal distance,  $f$  is the focal length.

Now, calibration could be implemented by the condition equation such as equation (4.68) – equation (4.72) by carrying interior  $(x_0, y_0, f, K_1, K_2, K_3, P_1, P_2)$

and exterior orientation ( $X_L, Y_L, Z_L, \omega, \Phi, \kappa$ ) and object space coordinate ( $X, Y, Z$ ) of corner points as parameters.

$$F_1 = x - x_0 + \frac{x - x_0}{r} (K_1 r^3 + K_2 r^5 + K_3 r^7) + P_1 (r^2 + 2(x - x_0)^2) + 2P_2 (x - x_0)(y - y_0) + f \frac{U}{W} = 0 \quad (4.68)$$

$$r = [(x - x_0)^2 + (y - y_0)^2]^{1/2}$$

$$F_2 = y - y_0 + \frac{y - y_0}{r} (K_1 r^3 + K_2 r^5 + K_3 r^7) + P_2 (r^2 + 2(y - y_0)^2) + 2P_1 (x - x_0)(y - y_0) + f \frac{V}{W} = 0 \quad (4.69)$$

$$U = m_{11}(X - X_L) + m_{12}(Y - Y_L) + m_{13}(Z - Z_L) \quad (4.70)$$

$$V = m_{21}(X - X_L) + m_{22}(Y - Y_L) + m_{23}(Z - Z_L) \quad (4.71)$$

$$W = m_{31}(X - X_L) + m_{32}(Y - Y_L) + m_{33}(Z - Z_L) \quad (4.72)$$

Where  $K_1, K_2, K_3$  are the coefficients of radial distortion,  $P_1, P_2$  are the coefficients of de-centering distortion.

By using minimal constraints of seven exterior orientation parameters, we can use the Unified Least Squares approach to solve the problem. In this research, the variance for  $(X_{L1}, Y_{L1}, Z_{L1}, \omega_1, \varphi_1, \kappa_1, X_{L2})$  were assumed to be  $1.0\text{e-}12$  and the rest of them were given by  $1.0\text{e}+12$ . The unknown parameters -

interior orientation parameters ( $x_0, y_0, f, K_1, K_2, K_3, P_1, P_2$ ), exterior orientation parameters of each image ( $\omega_i, \phi_i, \kappa_i, X_{Li}, Y_{Li}, Z_{Li}$ ) and the object space coordinates ( $X_i, Y_i, Z_i$ ) of each measured points can be estimated by Unified Least Squares. According to Mikhail et al. (2001), the Unified Least Squares approach assumes that all the variables of the mathematical formulation are observations. For the composition of weight matrix to each observation, if an observation has large variance, they are assigned zero weight. Otherwise, infinity of weight can be assigned to observation for zero variance observation such as constant.

The Unified Least Squares procedure is explained in Mikhail et al. (2001) as equation (4.73) to (4.81). Since estimated parameters are regarded as estimated observations, equation (4.73) can be composed.

$$\hat{\mathbf{x}} = \mathbf{x}^0 + \Delta = \mathbf{l}_x + \mathbf{v}_x \quad (4.73)$$

$$\mathbf{v}_x - \Delta = \mathbf{f}_x = \mathbf{x}^0 - \mathbf{l}_x \quad (4.74)$$

Where  $\mathbf{x}^0$ ,  $\mathbf{l}_x$  are vector of parameter approximation and parameter observations.

Combining condition equation of General Least Squares and equation (4.75) gives

$$\begin{bmatrix} \mathbf{A} & \mathbf{0} \\ \mathbf{0} & \mathbf{I} \end{bmatrix} \begin{bmatrix} \mathbf{v} \\ \mathbf{v}_x \end{bmatrix} + \begin{bmatrix} \mathbf{B} \\ -\mathbf{I} \end{bmatrix} \Delta = \begin{bmatrix} \mathbf{f} \\ \mathbf{f}_x \end{bmatrix} \quad (4.75)$$

$$\dot{\mathbf{A}}\dot{\mathbf{v}} + \dot{\mathbf{B}}\Delta = \dot{\mathbf{f}} \quad (4.76)$$

And total cofactor matrix becomes

$$\dot{\mathbf{Q}} = \begin{bmatrix} \mathbf{Q} & \mathbf{0} \\ \mathbf{0} & \mathbf{Q}_{xx} \end{bmatrix} \quad (4.77)$$

Therefore,

$$\dot{\mathbf{Q}}_e = \dot{\mathbf{A}}\dot{\mathbf{Q}}\dot{\mathbf{A}}^T = \begin{bmatrix} \dot{\mathbf{A}}\dot{\mathbf{Q}}\dot{\mathbf{A}}^T & \mathbf{0} \\ \mathbf{0} & \mathbf{Q}_{xx} \end{bmatrix} = \begin{bmatrix} \mathbf{Q}_e & \mathbf{0} \\ \mathbf{0} & \mathbf{Q}_{xx} \end{bmatrix} \quad (4.78)$$

$$\dot{\mathbf{N}} = \dot{\mathbf{B}}^T \dot{\mathbf{W}}_e \dot{\mathbf{B}} = [\mathbf{B}^T \mathbf{W}_e \mathbf{B} + \mathbf{W}_{xx}] = (\mathbf{N} + \mathbf{W}_{xx}) \quad (4.79)$$

$$\dot{\mathbf{t}} = \dot{\mathbf{B}}^T \dot{\mathbf{W}}_e \dot{\mathbf{f}} = \mathbf{B}^T \mathbf{W}_e \mathbf{f} - \mathbf{W}_{xx} \mathbf{f}_x = (\mathbf{t} - \mathbf{W}_{xx} \mathbf{f}_x) \quad (4.80)$$

$$\Delta = \dot{\mathbf{N}}^{-1} \dot{\mathbf{t}} = (\mathbf{N} + \mathbf{W}_{xx})^{-1} (\mathbf{t} - \mathbf{W}_{xx} \mathbf{f}_x) \quad (4.81)$$

#### 4.6 Absolute Orientation

In this research, two-step procedure with relative and absolute orientation was chosen for orienting images. In this two-step procedure, the absolute orientation is implemented to fit the model from relative orientation to the real world ground control coordinates system. The absolute orientation procedure begins with the calculation of object space coordinates of control points by intersection using the exterior orientation parameters estimated from relative orientation. For the first step of the intersection procedure, the image space coordinate was measured for control points. Then X, Y, and Z coordinates in the object space coordinate system can be calculated by solving equation (4.66) – (4.67). The second step is the transformation between intersected coordinates and ground coordinates of control points. We can use either seven-parameter or polynomial transformation.

According to Mikhail et al. (2001), seven-parameter transformation contains a uniform scale changes ( $\mu$ ), three rotations,  $\beta_1$ ,  $\beta_2$ , and  $\beta_3$  and three translations,  $t_1$ ,  $t_2$  and  $t_3$ . Equation (4.82) shows the general form of seven parameter transformation.

$$\mathbf{y} = \mu \mathbf{M} \mathbf{x} + \mathbf{t} \quad (4.82)$$

Where  $\mathbf{M}$  is the rotation matrix described in equation (4.83) and  $\mathbf{t}$  is the vector of three translations.

$$\mathbf{M} = \begin{bmatrix} \cos \beta_2 \cos \beta_3 & \cos \beta_1 \sin \beta_3 + \sin \beta_1 \sin \beta_2 \cos \beta_3 & \sin \beta_1 \sin \beta_3 - \cos \beta_1 \sin \beta_2 \cos \beta_3 \\ -\cos \beta_2 \sin \beta_3 & \cos \beta_1 \cos \beta_3 - \sin \beta_1 \sin \beta_2 \sin \beta_3 & \sin \beta_1 \cos \beta_3 + \cos \beta_1 \sin \beta_2 \sin \beta_3 \\ \sin \beta_2 & -\sin \beta_1 \cos \beta_2 & \cos \beta_1 \cos \beta_2 \end{bmatrix} \quad (4.83)$$

In our case, the vector  $\mathbf{x}$  represents the intersected coordinates and vector  $\mathbf{y}$  represents the coordinates of control points. And the condition equation becomes equation (4.84)

$$F = \mu \mathbf{M} \mathbf{x} + \mathbf{t} - \mathbf{y} = 0 \quad (4.84)$$

The second method for absolute orientation is the polynomial transformation. The most well-known polynomial transformation is Shum adjustment developed at the National Research Council of Canada (NRC). (Mikhail et al., 2001) and the condition equation is described as equation (4.85) – (4.87).

$$x' = x + a_1 + a_3 x - a_4 y + a_5 (x^2 - y^2) - 2a_6 xy + a_7 (x^3 - 3xy^2) - a_8 (3x^2 y - y^3) + \dots \quad (4.85)$$

$$y' = y + a_2 + a_4 x + a_3 y + a_6 (x^2 - y^2) + 2a_5 xy + a_7 (3x^2 y - y^3) + a_8 (x^3 - 3x^2 y) + \dots \quad (4.86)$$

$$\begin{aligned}
z' = & z + b_0 - 2b_2x + 2b_1y \\
& + c_1x^2 + c_2x^3 + c_3x^4 \\
& + d_1xy + d_2x^2y + d_3x^3y + d_4x^4y + \\
& + e_1y^2 + e_2xy^2
\end{aligned} \tag{4.87}$$

By absolute orientation either with seven parameter transformation or polynomial transformation, we can estimate misclosures at check points. We will compare the misclosures from bundle block adjustment with minimal constraints, seven parameter transformation and polynomial transformation. In practice, the order of the polynomial should be chosen by strip length and the amount of control point data. Low redundancy polynomial estimation produces unexpected undulations away from the support points.

#### 4.7 Bundle Block Adjustment

According to Mikhail et al. (2001), a single image is regarded as a bundle of image rays and a position and orientation of such a bundle can be estimated by bundle block adjustment with given ground control information and the rays in the bundle. The bundle adjustment is also regarded as the most accurate and flexible method of triangulation. We implemented three kinds of bundle block adjustment. The first case is bundle block adjustment for calibrated dataset. In this case, we carry exterior orientations of camera, ground control points with known accuracy and pass point information as parameters. This is the most ideal case because camera parameters are estimated in a robust environment and control points information are most realistic. However, it is the method of high

cost because control point information acquisition is a very labor intensive and tedious procedure. The second case is the bundle block adjustment with self calibration. In this case, we carried principal point offset, focal length, radial lens distortion, tangential lens distortion as additional parameters. Although this procedure does not require prior information of camera parameters, it still requires a large number of control point information. The third case is bundle block adjustment with minimal constraints which requires seven fixed parameters. After bundle block adjustment, we can transform the result to the ground coordinate system by seven parameter transformation as described in chapter 4.6. This procedure has same condition with the procedures of relative and absolute orientation approaches suggested in this research. Therefore, bundle block adjustment with minimal constraints and seven parameter transformation will be the criteria of accuracy assessment of the suggested research. All of the three types of bundle block adjustment will be implemented and the accuracies will be shown in both the image space as residuals and ground space by misclosures at check points. The control point information was acquired by GPS surveying as described in section 3.3 and pass point information was acquired in GIS environment. Pass points should be included to make stronger geometry. Therefore, the pass points were chosen so that the locations should be as uniformly distributed on the entire image space as possible. For the measurement in GIS environment, georeferenced aerial photography with 1m resolution was used as reference data and the location of pass points were measured. Bundle block adjustment is implemented by Unified Least Squares



and the condition equations are equation (4.68) and equation (4.69). The interior orientation parameters were estimated by camera calibration procedure described in chapter 4.5 and they were used in condition equations for the experiment with calibrated camera.

#### 4.8 Post Adjustment Statistics

After least squares adjustment, we can assess the precision of the result by post adjustment statistics. According to Bethel (2004), the post adjustment statistics are composed of two main parts. The first part is the global test and confidence interval estimation, and the second is the confidence region estimation by error ellipses or ellipsoids. For the global test, the test statistic is computed by equation (4.88).

$$Test\ statistic = \frac{\mathbf{v}^T \mathbf{W} \mathbf{v}}{\sigma_0^2} \sim \chi_r^2 \quad (4.88)$$

where  $\mathbf{v}$  is the residual vector,  $\mathbf{W}$  is the weight matrix and  $\sigma_0$  is the reference variable.

The *chi* square test is performed for test statistics with null hypothesis of Equation (4.89) and alternate hypothesis of Equation (4.90).

$$H_0 : \sigma^2 = \sigma_0^2 \quad (4.89)$$

$$H_0 : \sigma^2 > \sigma_0^2 \quad (4.90)$$

If null hypothesis is accepted, we can use the covariance matrix as the original form as equation (4.91) and proceed to Z test to estimate confidence interval.

$$\Sigma_{\Delta\Delta} = \sigma_0^2 \mathbf{Q}_{\Delta\Delta} \quad (4.91)$$

For the confidence region estimation, the Eigen value and Eigen vector should be calculated. Eigen value decides the size of error ellipsoid in major and minor axes and Eigen vector decides the angle of those axes. For example with semi major axis,

$$\sigma'_x = \sqrt{\lambda_1} \quad (4.92)$$

Then, the size of semi major axis become Equation (4.93)

$$L_1 = C \cdot \sigma'_x \quad (4.93)$$

where C can be estimated by equation (4.94)

$$C = \sqrt{\chi_{n,P}^2} \quad (4.94)$$

where  $\chi$  is the inverse of the chi square cumulative distribution function.

For rejected null hypothesis, we should use alternate form of covariance matrix such as equation (4.95) and proceed to  $t$  test to estimate confidence interval.

$$\hat{\Sigma}_{\Delta\Delta} = \hat{\sigma}_0^2 \mathbf{Q}_{\Delta\Delta} \quad (4.95)$$

For the confidence region estimation, most of procedure is same with the case of accepted hypothesis except equation (4.94). For the rejected case, the inverse of  $F$  cumulative distribution function is used to estimate  $C$  as described in Equation (4.96).

$$C = \sqrt{2F_{n,dof,P}} \quad (4.96)$$

It should be noted that the covariance matrix should be estimated differently for KF compared to SLS or CLS. For SLS and CLS, cofactor matrix can be estimated from the inverse of Normal equation such as Equation (4.97).

$$\mathbf{Q}_{\Delta\Delta} = \mathbf{N}^{-1} \quad (4.97)$$

For KF, Dolloff (2012) derived the covariance matrix ( $P_{multi}$ ) as below equation

(4.98) for the vector  $\begin{bmatrix} X_k^+ & X_{k+q}^+ & X_{k+p+q}^+ \end{bmatrix}^T$ .

$$\mathbf{Q}_{\Delta\Delta} = P_{multi} = \begin{bmatrix} P_k^+ & P_k^+ A_k^{k+qT} & P_k^+ A_k^{k+qT} A_{k+q}^{k+q+pT} \\ \cdot & P_{k+q}^+ & P_{k+q}^+ A_{k+q}^{k+q+pT} \\ \cdot & \cdot & P_{k+q+p}^+ \end{bmatrix} \quad (4.98)$$

Where,  $P_k^+$  is the updated estimate's covariance,  $k$ ,  $k+q$  and  $k+q+p$  are times.

$A_k^{k+q}$  is computed from equation (4.99) and (4.100)

$$A_k^{k+q} = (I - G_{k+q} H_{k+q}) \Phi_{k+q-1} (I - G_{k+q-1} H_{k+q-1}) \Phi_{k+q-2} \cdots (I - G_{k+1} H_{k+1}) \quad (4.99)$$

Where  $G_k$  is Kalman gain,  $H_k$  is the partial derivative of condition equation to the parameter vectors (equivalent to  $B$  matrix in the least square), and  $\Phi$  is the state transition matrix.

## CHAPTER 5. ESTIMATION STRATEGIES

Once we have matched points from image pairs, we can estimate five exterior orientation parameters  $(b_y, b_z, \omega, \phi, \kappa)$  for the first model and six exterior orientation parameters  $(b_x, b_y, b_z, \omega, \phi, \kappa)$  from the second model. For the first model, one of the six orientation parameters has to be fixed and  $b_x$  was chosen. The relative orientation by coplanarity and scale restraint condition was explained in section 4.4. To solve the relative orientation problem, three approaches were considered. The first method is Simultaneous Least Square (SLS), the second is Cantilever Least Square (CLS), and the last is Kalman Filter Least Square (KF).

### 5.1 Simultaneous Least Squares

In SLS solution, the relative orientation problem with coplanarity and scale restraint conditions for entire models are solved at the same time by General Least Squares. Equation (5.1) shows the exemplary equation for  $n$  epochs of models. Note that this includes equations for the dynamic model, but it is estimated in batch mode rather than sequentially.

$$\begin{bmatrix} \mathbf{A}_1 & & & & & & & & \\ & \mathbf{A}_2 & & & & & & & \\ & & \mathbf{a}_2 & & & & & & \\ & & & \mathbf{I} & & & & & \\ & & & & \mathbf{A}_3 & & & & \\ & & & & & \mathbf{a}_3 & & & \\ & & & & & & \mathbf{I} & & \\ & & & & & & & \ddots & \\ & & & & & & & & \mathbf{A}_n \\ & & & & & & & & & \mathbf{a}_n \end{bmatrix} \mathbf{V} + \begin{bmatrix} \mathbf{B}_1 & & & & & & & & \\ & \mathbf{B}_2 & & & & & & & \\ & & \mathbf{b}_2 & & & & & & \\ & & & -\Phi & & & & & \\ & & & & \mathbf{I} & & & & \\ & & & & & \mathbf{B}_3 & & & \\ & & & & & & \mathbf{b}_3 & & \\ & & & & & & & -\Phi & \\ & & & & & & & & \mathbf{I} \\ & & & & & & & & & \vdots \\ & & & & & & & & & & \mathbf{B}_n \\ & & & & & & & & & & & \mathbf{b}_n \end{bmatrix} \begin{bmatrix} \Delta_1 \\ \Delta_2 \\ \Delta_3 \\ \vdots \\ \Delta_n \end{bmatrix} = \begin{bmatrix} \mathbf{F}_1 \\ \mathbf{F}_2 \\ \mathbf{f}_2 \\ \mathbf{0} \\ \mathbf{F}_3 \\ \mathbf{f}_3 \\ \mathbf{0} \\ \vdots \\ \mathbf{F}_n \\ \mathbf{f}_n \end{bmatrix} \quad (5.1)$$

where  $\mathbf{A}$ ,  $\mathbf{B}$ , and  $\mathbf{F}$  are the matrix presented in the coplanarity condition.  $\mathbf{a}$ ,  $\mathbf{b}$  and  $\mathbf{f}$  are the matrix presented in scale restraint condition.  $\Phi$  is the state transition matrix.  $\mathbf{V}$  is residual vector and  $\Delta$  is parameter vectors. For example,  $\mathbf{A}_3$  and  $\mathbf{a}_3$  can be solved by equation (4.46) and (4.55). And  $\mathbf{B}_3$  and  $\mathbf{b}_3$  are represented as,

$$\mathbf{B}_3 = \begin{bmatrix} \frac{\partial \mathbf{F}_3}{\partial \omega_2} & \frac{\partial \mathbf{F}_3}{\partial \varphi_2} & \frac{\partial \mathbf{F}_3}{\partial \kappa_2} & \frac{\partial \mathbf{F}_3}{\partial bx_3} & \frac{\partial \mathbf{F}_3}{\partial by_3} & \frac{\partial \mathbf{F}_3}{\partial bz_3} & \frac{\partial \mathbf{F}_3}{\partial \omega_3} & \frac{\partial \mathbf{F}_3}{\partial \varphi_3} & \frac{\partial \mathbf{F}_3}{\partial \kappa_3} \end{bmatrix} \quad (5.2)$$

And

$$\mathbf{b}_3 = \begin{bmatrix} \frac{\partial \mathbf{f}_3}{\partial \omega_1} & \frac{\partial \mathbf{f}_3}{\partial \varphi_1} & \frac{\partial \mathbf{f}_3}{\partial \kappa_1} & \frac{\partial \mathbf{f}_3}{\partial bx_2} & \frac{\partial \mathbf{f}_3}{\partial by_2} & \frac{\partial \mathbf{f}_3}{\partial bz_2} & \frac{\partial \mathbf{f}_3}{\partial \omega_2} & \frac{\partial \mathbf{f}_3}{\partial \varphi_2} & \frac{\partial \mathbf{f}_3}{\partial \kappa_2} & \frac{\partial \mathbf{f}_3}{\partial bx_3} & \frac{\partial \mathbf{f}_3}{\partial by_3} & \frac{\partial \mathbf{f}_3}{\partial bz_3} & \frac{\partial \mathbf{f}_3}{\partial \omega_3} & \frac{\partial \mathbf{f}_3}{\partial \varphi_3} & \frac{\partial \mathbf{f}_3}{\partial \kappa_3} \end{bmatrix} \quad (5.3)$$

And the weight matrix can be expressed as,

$$\mathbf{W} = \begin{bmatrix} \mathbf{W}_1 & & & & & \\ & \mathbf{W}_2 & & & & \\ & & \mathbf{w}_2 & & & \\ & & & \mathbf{w}_{t2} & & \\ & & & & \mathbf{W}_3 & \\ & & & & & \mathbf{w}_3 \\ & & & & & & \mathbf{w}_{t3} \\ & & & & & & & \ddots \\ & & & & & & & & \mathbf{W}_n \\ & & & & & & & & & \mathbf{w}_n \end{bmatrix} \quad (5.4)$$

Where  $\mathbf{W}_i$  is the weight for coplanarity condition,  $\mathbf{w}_i$  is the weight for scale restraint condition,  $\mathbf{w}_{tk}$  is the weight for state transition, which is the inverse of the covariance matrix estimated from trajectory information by equation (5.5).

$$\mathbf{Q}_{ww(i,i)_k} = (\mathbf{X}_{(i,i)_{k+1}} - \mathbf{X}_{(i,i)_k})^2 \quad (5.5)$$

Where  $\mathbf{X}$  is the exterior orientation parameters,  $\mathbf{k}$  is the epoch number.

## 5.2 Cantilever Least Squares

The exterior orientation parameters can be estimated sequentially and they can be added to the parameters of the previous model to solve relative orientation of the next epoch. This process is called Cantilever Least Squares (CLS) because it shows cantilever effect by the accumulation of systematic error.

For example, we can estimate five exterior orientation parameters such as  $b_{y1}, b_{z1}, \omega_1, \phi_1, \kappa_1$  by solving equation (5.6).

$$\mathbf{A}_1 \mathbf{V}_1 + \mathbf{B}_1 \Delta_1 = \mathbf{F}_1 \quad (5.6)$$

Where  $\mathbf{A}_1, \mathbf{B}_1, \mathbf{F}_1$  are from the coplanarity condition, and  $\Delta_1 = \begin{bmatrix} b_{y1} \\ b_{z1} \\ \omega_1 \\ \phi_1 \\ \kappa_1 \end{bmatrix}$

After we estimate five orientation parameters for the model by General Least Squares, we can estimate six orientation parameters for the second model by solving equation (5.7) by the General Least Squares.

$$\begin{bmatrix} \mathbf{A}_2 & \mathbf{a}_2 \end{bmatrix} \mathbf{V}_2 + \begin{bmatrix} \mathbf{B}_2 \\ \mathbf{b}_2 \end{bmatrix} \Delta_2 = \begin{bmatrix} \mathbf{F}_2 \\ \mathbf{f}_2 \end{bmatrix} \quad (5.7)$$

Where  $\mathbf{A}_2, \mathbf{B}_2, \mathbf{F}_2$  are from the coplanarity condition,  $\mathbf{a}_2, \mathbf{b}_2, \mathbf{f}_2$  are from the scale

restraint condition and  $\Delta_2 = \begin{bmatrix} b_{x2} \\ b_{y2} \\ b_{z2} \\ \omega_2 \\ \phi_2 \\ \kappa_2 \end{bmatrix}$ .



$\mathbf{A}_2$  and  $\mathbf{a}_2$  can be solved as in equation (4.46) and (4.55).  $\mathbf{B}_2$  and  $\mathbf{b}_2$  are shown in equation (5.8) and (5.9).

$$\mathbf{B}_2 = \begin{bmatrix} \frac{\partial \mathbf{F}_2}{\partial b x_2} & \frac{\partial \mathbf{F}_2}{\partial b y_2} & \frac{\partial \mathbf{F}_2}{\partial b z_2} & \frac{\partial \mathbf{F}_2}{\partial \omega_2} & \frac{\partial \mathbf{F}_2}{\partial \varphi_2} & \frac{\partial \mathbf{F}_2}{\partial \kappa_2} \end{bmatrix} \quad (5.8)$$

And

$$\mathbf{b}_2 = \begin{bmatrix} \frac{\partial \mathbf{f}_2}{\partial b x_2} & \frac{\partial \mathbf{f}_2}{\partial b y_2} & \frac{\partial \mathbf{f}_2}{\partial b z_2} & \frac{\partial \mathbf{f}_2}{\partial \omega_2} & \frac{\partial \mathbf{f}_2}{\partial \varphi_2} & \frac{\partial \mathbf{f}_2}{\partial \kappa_2} \end{bmatrix} \quad (5.9)$$

The exterior orientation parameters from next models can also be estimated by the same manner.

### 5.3 Kalman Filtering Least Squares

The adaptation of KF to strip formation by relative orientation is a contribution of this proposed research. For KF in this experiment, linearized Kalman Filtering with dynamic model was used. The condition equation for KF is same with CLS except equation (5.8). In KF, the coplanarity condition can be composed by the current and the next model as shown in equation (5.10).

$$\mathbf{B}_2 = \begin{bmatrix} \frac{\partial \mathbf{F}_2}{\partial b x_2} & \frac{\partial \mathbf{F}_2}{\partial b y_2} & \frac{\partial \mathbf{F}_2}{\partial b z_2} & \frac{\partial \mathbf{F}_2}{\partial \omega_2} & \frac{\partial \mathbf{F}_2}{\partial \varphi_2} & \frac{\partial \mathbf{F}_2}{\partial \kappa_2} \\ 0 & 0 & 0 & \frac{\partial \mathbf{F}_3}{\partial \omega_2} & \frac{\partial \mathbf{F}_3}{\partial \varphi_2} & \frac{\partial \mathbf{F}_3}{\partial \kappa_2} \end{bmatrix} \quad (5.10)$$

Grewal and Andrews (2001) described discrete linearized Kalman Filtering and it was applied to this experiment. Table 5.1 shows Grewal and Andrews' (2001) equations and those applied in this experiment.

Table 5.1 The description of matrix of linearized Kalman Filtering

	Grewal and Andrews (2001)	Experiment
Nonlinear nominal trajectory model	$\mathbf{x}_k^{\text{nom}} = f_{k-1}(\mathbf{x}_{k-1}^{\text{nom}})$	$\begin{bmatrix} b_x \\ b_y \\ b_z \\ \omega \\ \varphi \\ \kappa \end{bmatrix}_k^{\text{nom}} = \begin{bmatrix} b_x \\ b_y \\ b_z \\ \omega \\ \varphi \\ \kappa \end{bmatrix}_{k-1}^{\text{nom}}$
Linearized perturbed trajectory model	$\delta \mathbf{x}_k = \left. \frac{\partial f_{k-1}}{\partial \mathbf{x}} \right _{\mathbf{x}=\mathbf{x}_{k-1}^{\text{nom}}} \delta \mathbf{x}_{k-1} + \mathbf{w}_{k-1}$	$\begin{bmatrix} \Delta b_x \\ \Delta b_y \\ \Delta b_z \\ \Delta \omega \\ \Delta \varphi \\ \Delta \kappa \end{bmatrix}_k = \mathbf{I}_{(6,6)} \begin{bmatrix} \Delta b_x \\ \Delta b_y \\ \Delta b_z \\ \Delta \omega \\ \Delta \varphi \\ \Delta \kappa \end{bmatrix}_{k-1} + \mathbf{w}_{k-1}$
Nonlinear measurement model	$\mathbf{z}_k = \mathbf{h}_k(\mathbf{x}_k) + \mathbf{v}_k$	$F = \begin{bmatrix} b_x & b_y & b_z \\ u_1 & v_1 & w_1 \\ u_2 & v_2 & w_2 \end{bmatrix} = 0$ $F = \frac{ A_1 }{ A_2 } + \frac{ A_3 }{ A_4 } = 0$

Table 5.1 Continued.

Linearized approximation equation	$\hat{\delta \mathbf{x}}_k(-) = \Phi_{k-1}^{[1]} \hat{\delta \mathbf{x}}_{k-1}(+),$ $\Phi_{k-1}^{[1]} \approx \left. \frac{\partial f_{k-1}}{\partial \mathbf{x}} \right _{\mathbf{x}=\mathbf{x}_{k-1}^{nom}}$	$\begin{bmatrix} \Delta b_x \\ \Delta b_y \\ \Delta b_z \\ \Delta \omega \\ \Delta \varphi \\ \Delta \kappa \end{bmatrix}_k = \mathbf{I}_{(6,6)} \begin{bmatrix} \Delta b_x \\ \Delta b_y \\ \Delta b_z \\ \Delta \omega \\ \Delta \varphi \\ \Delta \kappa \end{bmatrix}_{k-1}$
Conditioning the predicted perturbation on the measurement	$\hat{\delta \mathbf{x}}_k(+) = \hat{\delta \mathbf{x}}_k(-) +$ $\bar{\mathbf{K}}_k [\mathbf{z}_k - \mathbf{h}_k(\mathbf{x}_k^{nom}) - \mathbf{H}_k^{[1]} \hat{\delta \mathbf{x}}_k(-)]$ $\mathbf{H}_k^{[1]} \approx \left. \frac{\partial \mathbf{h}_k}{\partial \mathbf{x}} \right _{\mathbf{x}=\mathbf{x}_k^{nom}}$	$\Delta_k = \Delta_k^- + \bar{\mathbf{K}}_k (\mathbf{f}_k - \mathbf{B}_k \Delta_k^-)$ $, \text{ where } \Delta = \begin{bmatrix} \Delta b_x \\ \Delta b_y \\ \Delta b_z \\ \Delta \omega \\ \Delta \varphi \\ \Delta \kappa \end{bmatrix}$
Computing the <i>a priori</i> covariance matrix	$\mathbf{P}_k(-) = \Phi_{k-1}^{[1]} \mathbf{P}_{k-1}(+) \Phi_{k-1}^{[1]T} + \mathbf{Q}_{k-1}$	$\mathbf{Q}_{xx_k}^- = \mathbf{I}_{(6,6)} \mathbf{Q}_{xx_{k-1}} \mathbf{I}^T + \mathbf{Q}_{ww}$
Computing Kalman gain	$\bar{\mathbf{K}}_k =$ $\mathbf{P}_k(-) \mathbf{H}_k^{[1]T} [\mathbf{H}_k^{[1]} \mathbf{P}_k(-) \mathbf{H}_k^{[1]T} + \mathbf{R}_k]^{-1}$	$\bar{\mathbf{K}}_k =$ $\mathbf{Q}_{xx_k}^- \mathbf{B}_k^T (\mathbf{B}_k \mathbf{Q}_{xx_k}^- \mathbf{B}_k^T + \mathbf{Q}_{e_k})^{-1}$
Computing the a posteriori covariance matrix	$\mathbf{P}_k(+) = \{\mathbf{I} - \bar{\mathbf{K}}_k \mathbf{H}_k^{[1]}\} \mathbf{P}_k(-)$	$\mathbf{Q}_{xx_k} = (\mathbf{I} - \bar{\mathbf{K}}_k \mathbf{B}_k) \mathbf{Q}_{xx_k}^-$

It should be noted that equation (4.98) was used for post adjustment statistics for Kalman Filtering. In this research, the type of Kalman Filtering is discrete time, nonlinear, linearized Kalman Filtering, and fixed interval smoothing

was used as the smoothing algorithm. Figure 5.1 shows the types of Kalman Filtering and Smoothing. The hatched block is the type of Kalman Filtering and Smoothing algorithm used in this research.

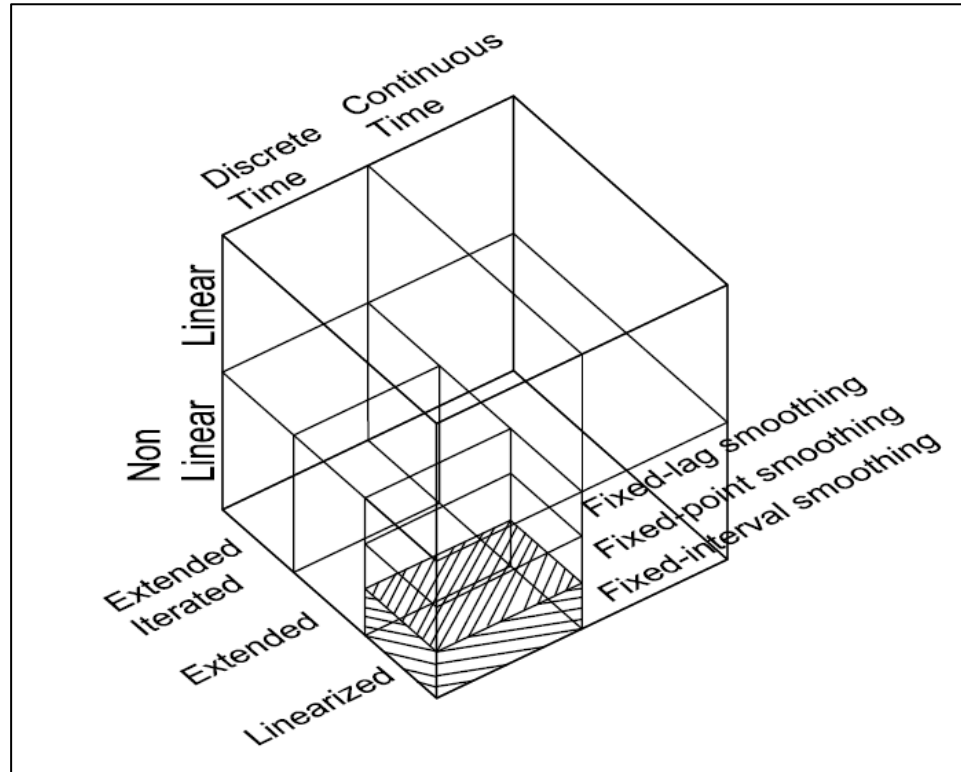


Figure 5.1 The types of Kalman Filtering  
(can also be done without smoothing)

For the linearized perturbed trajectory model used in this research, the white noise term can be estimated by equation (5.11) since the state transition term in the Linearized approximation equation in table 5.1 is the identity matrix.

$$w_{k-1} = \delta \mathbf{x}_k - \delta \mathbf{x}_{k-1} \quad (5.11)$$

Therefore,

$$\mathbf{Q}_{k-1}(i,i) = \text{Var}(X_{i_k}) + \text{Var}(X_{i_{k-1}}) - 2\text{Cov}(X_{i_k}, X_{i_{k-1}}) \quad (5.12)$$

And covariance of parameters can be estimated from SLS. It should be noted that the state variables in a linearized Kalman filtering are incremental quantities, and not total quantities. And Kalman Filtering algorithm was applied forward and backward iteratively until we could get stable solution for the parameters. This process is called forward and backward Kalman smoothing and it is explained as follows using the notation of Grewal and Andrews (2001).

(a) Computation of Kalman gain

Kalman gain is computed by equation (5.13).

$$\mathbf{K}_k = \mathbf{P}_k^- \mathbf{H}_k^T (\mathbf{H}_k \mathbf{P}_k^- \mathbf{H}_k^T + \mathbf{R}_k)^{-1} \quad (5.13)$$

(b) Update of estimate with measurement  $\mathbf{z}_k$

The parameters are updated like equation (5.14) with measurement  $\mathbf{z}_k$  and Kalman gain  $\mathbf{K}_k$ .

$$\hat{\mathbf{x}}_k = \hat{\mathbf{x}}_k^- + \mathbf{K}_k (\mathbf{z}_k - \mathbf{H}_k \hat{\mathbf{x}}_k^-) \quad (5.14)$$

(c) Computation of Error covariance for updated estimate

The error covariance can be computed like equation (5.15)

$$\mathbf{P}_k = (\mathbf{I} - \mathbf{K}_k \mathbf{H}_k) \mathbf{P}_k^- \quad (5.15)$$

(d) Projection ahead

Then, the parameters and the error covariance matrix can be predicted like equation (5.16) and (5.17)

$$\hat{\mathbf{x}}_{k+1}^- = \Phi_k \hat{\mathbf{x}}_k \quad (5.16)$$

$$\mathbf{P}_{k+1}^- = \Phi_k \mathbf{P}_k \Phi_k^T + \mathbf{Q}_k \quad (5.17)$$

Where  $\Phi_k$  is state transition matrix,  $\mathbf{Q}_k$  is the covariance matrix of state transition equation for white noise term

(e) Computation of smoothing gain

The smoothing gain is computed as equation (5.18).

$$\mathbf{K}_{s_i} = \mathbf{P}_{k|k} \Phi_{k+1|k}^T \mathbf{P}_{k+1|k}^{-1} \quad (5.18)$$

(f) Updates of the estimates of the increment of the parameter

Then, updated estimates can be computed as in equation (5.19).

$$\mathbf{x}_{i|n} = \mathbf{x}_{i|i} + \mathbf{K}_{s_i} (\mathbf{x}_{i+1|n} - \mathbf{x}_{i+1|i}) \quad (5.19)$$

(g) Computation of covariance matrix

The covariance matrix is computed by

$$\mathbf{P}_{k|n} = \mathbf{P}_{k|k} + \mathbf{K}_{s_i} (\mathbf{P}_{k+1|n} - \mathbf{P}_{i+1|i}) \mathbf{K}_{s_i}^T \quad (5.20)$$

(h) State vector update

Update state vector elements for each frame as

$$(\mathbf{X}_i)_k = (\mathbf{X}_i)_{k-1} + \mathbf{x}_{i|n} \quad (5.21)$$

(g) Convergence check

Compute the objective function as equation (5.22)

$$\varphi = \mathbf{v}^T \mathbf{W} \mathbf{v} \quad (5.22)$$

Compute the percentage change in the objective function. If the percentage change is less than a threshold, it is regarded as converged. Otherwise the procedure described above should be repeated by forward and backward sweep until the convergence criteria is met.

## CHAPTER 6.APPLICATIONS

### 6.1 APPLICATION1: Camera Calibration

For this project, camera calibration is an essential step and is carried out using added parameters in a bundle block adjustment (BBA) as described in section 4.5. For the calibration imagery, there were three approaches to image acquisition and target layout. In every case, the variable zoom is set to the widest angle setting and the focus is set to “infinity”. These settings and their potential for inconsistency are addressed later. The three approaches were:

- Terrestrial imagery of a “natural” (urban) scene at ~ 30m object distance. This was further subdivided into three cases, with the third case having stronger B/H geometry.
- Terrestrial imagery of a synthetic target array at 3 – 4 m object distance.
- Aerial imagery of the project site, no special attention given to attitude diversity.

See Figure 6.1 for illustration of these three approaches.

In order to quantify the importance and effect of the parameters of camera calibration, methods akin to sensitivity analysis and error propagation were employed.



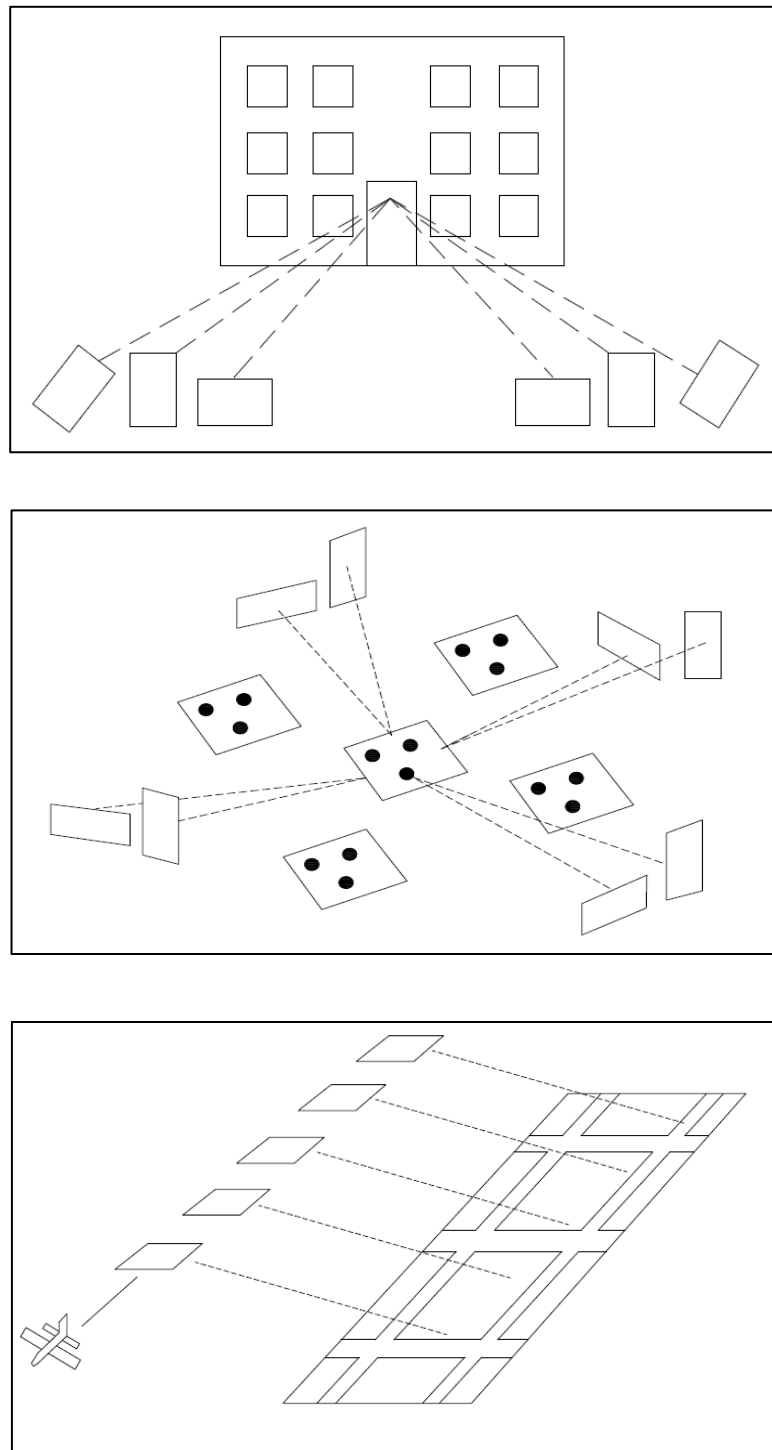


Figure 6.1 Three Calibration Approaches

### 6.1.1 Calibration from Urban, Laboratory Scene

The camera was first calibrated using the imagery in figure 6.2 by the procedure described in section 4.5. The parameters carried in the bundle block adjustment (BBA) were principal point offsets ( $x_0$ ,  $y_0$ ), focal length ( $f$ ), the coefficients for radial lens distortion ( $K_1$ ,  $K_2$ ,  $K_3$ ), decentering distortion ( $P_1$ ,  $P_2$ ), the exterior orientation parameters ( $X_{Li}$ ,  $Y_{Li}$ ,  $Z_{Li}$ ,  $\omega_i$ ,  $\phi_i$ ,  $\kappa_i$ ) of each image, and the X, Y, Z coordinates of each pass point. Figure 6.2 shows the images of the calibration scene. 40 points in the first pair were measured to estimate the object space coordinates. 20 points in each subsequent image were then measured. To generate initial approximations for the nonlinear BBA, I used the relative orientation algorithm described earlier, starting with the eight point algorithm followed by conventional, coplanarity based relative orientation. To resolve the scale, the length between two object points was measured by a steel tape and fixed. The *a priori* standard deviations for interior orientation parameters were chosen as in table 6.1

Table 6.1 *A Priori* Standard Deviation of Interior Orientation Parameters

PAR	$x_0$ (pixel)	$y_0$ (pixel)	$f$ (pixel)	$K_1$ (pixel)	$K_2$ (pixel)	$K_3$ (pixel)	$P_1$ (pixel)	$P_2$ (pixel)
$\sigma$	1000	1000	1000	100	100	100	100	100

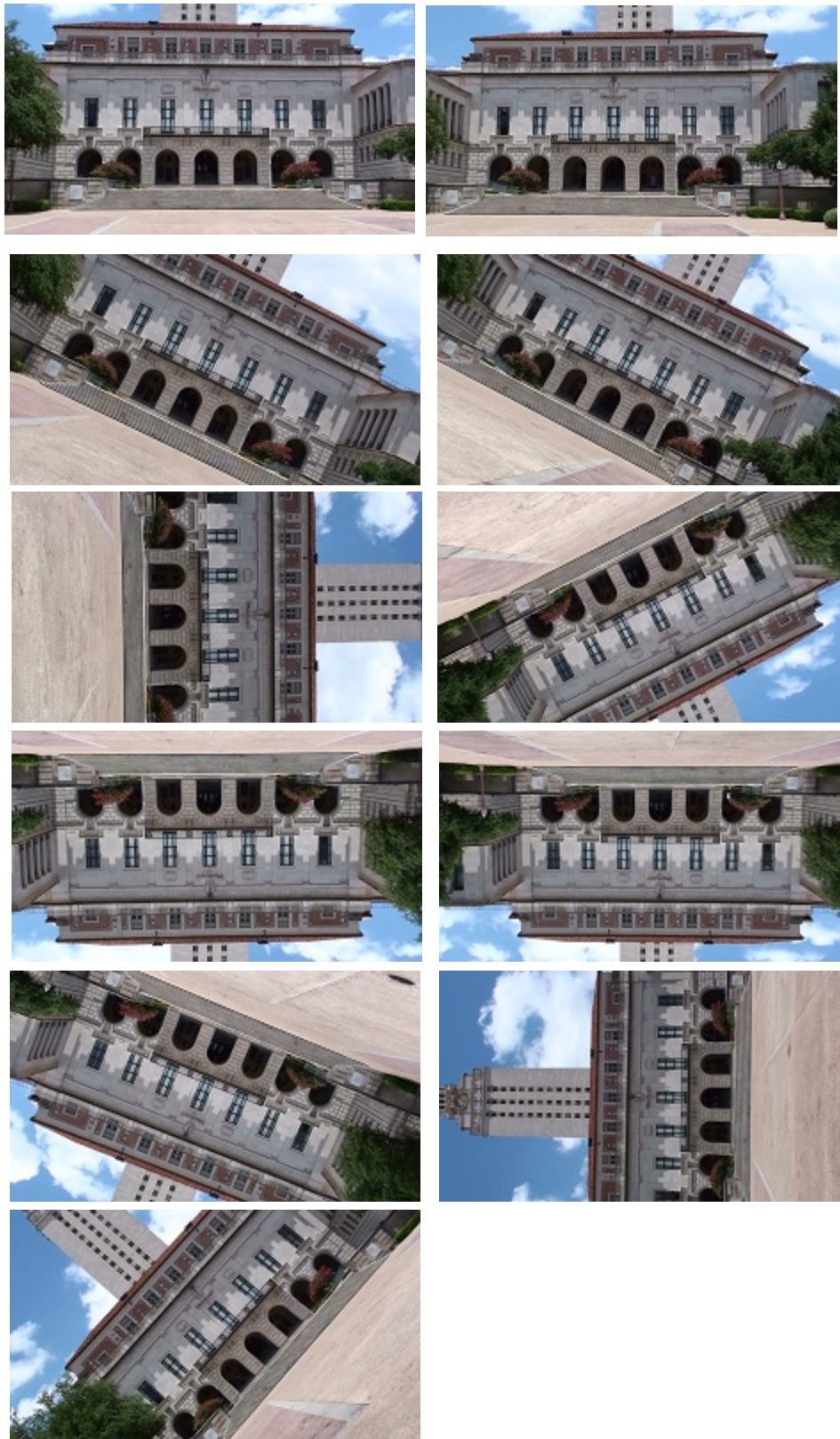


Figure 6.2 Calibration Target for Urban 1 and 2





Figure 6.3 Calibration Target for Urban 3

Therefore, we can establish a weight matrix for all of the parameters in the unified least squares adjustment problem. The calibration was performed twice (different points) with the dataset in figure 6.2 and once more with the dataset in figure 6.3 (wider baseline). There were three estimations done with this approach. Table 6.2 shows the result of the first calibration. It is seen in table 6.2, that for most of the lens distortion parameters, the corresponding sigma is greater in magnitude than the parameter value. This indicates that they are not particularly significant, yet necessary. Table 6.3 shows the observation residuals. The residuals show the calibration was satisfactory in the image space. Table 6.4 shows the correlation matrix of the estimated calibration parameters and we can see that some pairs have very high correlation. Especially,  $K_1$ ,  $K_2$ , and  $K_3$  are highly correlated with each other. Also,  $(P_1, x_0)$  and  $(P_2, y_0)$  are highly correlated parameters. There are two consequences to this high correlation: (1) the estimation itself becomes numerically unstable (high condition number), and (2) the meaning of an individual parameter value is not as significant. Therefore, it is important to compare the combination effect of all the parameters rather than comparing individual parameters. Figure 6.4 shows the location of the pass points (all points on all images overlaid). Figure 6.5 shows the radial and decentering distortion grid plot and figure 6.6 shows the quiver plot of the first calibration attempt. Those two figures show the effect of calibration from all of the parameters.

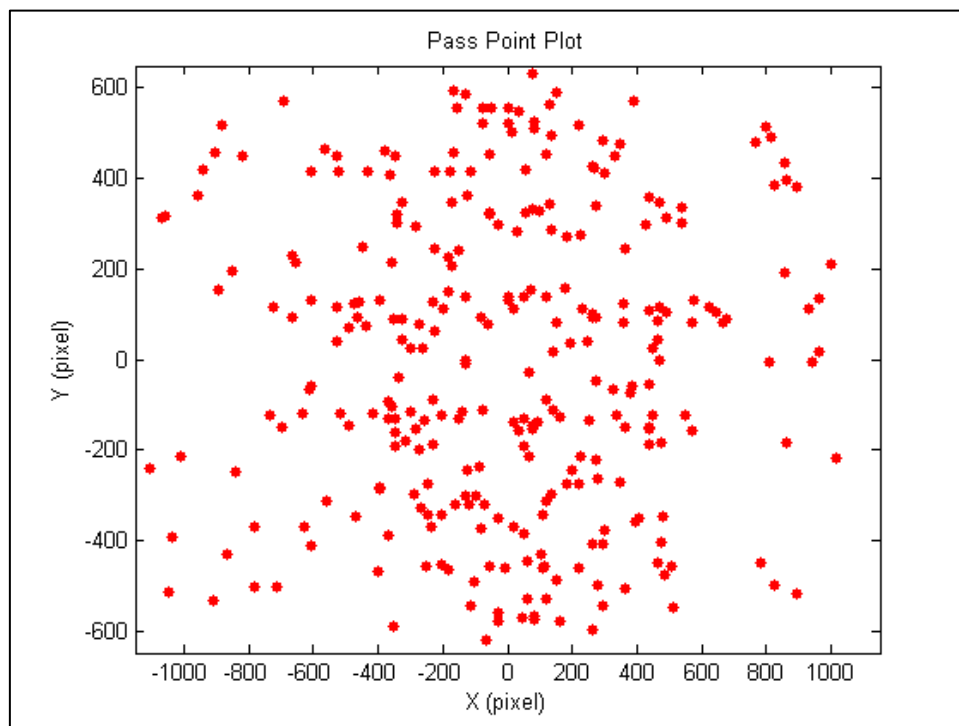


Figure 6.4 Pass Point plot of Urban 1  
(all points on all images overlaid)

Table 6.2 The Result of Calibration (Urban 1)

parameter	unit	value	$\sigma$	$\sigma$ (pixel)
$x_0$	(pixel)	-9.99	13.75	13.75
$y_0$	(pixel)	-2.56	11.02	11.02
$f$	(pixel)	2647.22	73.41	73.41
$K_1$		-1.46E-08	1.05E-08	2.22
$K_2$		3.07E-15	19.93E-15	3.87
$K_3$		-1.80E-21	9.43E-21	2.00
$P_1$		1.58E-07	8.65E-07	0.32
$P_2$		6.55E-07	6.45E-07	0.24
Condition Number	1.70e+014			

Table 6.3 RMS of Residuals (Urban 1, units=pixels)

residual	$v_x$	$v_y$	Mean
RMS	0.67	0.72	0.70

Table 6.4 Correlation Matrix for Calibration Parameters (Urban1)

	$x_0$	$y_0$	$f$	$K_1$	$K_2$	$K_3$	$P_1$	$P_2$
$x_0$	1.00	-0.01	0.10	-0.09	0.05	-0.04	-0.96	0.01
$y_0$	-0.01	1.00	-0.01	0.04	-0.03	0.02	0.07	-0.93
$f$	0.10	-0.01	1.00	-0.12	0.00	0.02	-0.01	0.05
$K_1$	-0.09	0.04	-0.12	1.00	-0.93	0.88	0.02	0.02
$K_2$	0.05	-0.03	0.00	-0.93	1.00	-0.99	0.01	-0.03
$K_3$	-0.04	0.02	0.02	0.88	-0.99	1.00	0.00	0.04
$P_1$	-0.96	0.07	-0.01	0.02	0.01	0.00	1.00	-0.05
$P_2$	0.01	-0.93	0.05	0.02	-0.03	0.04	-0.05	1.00

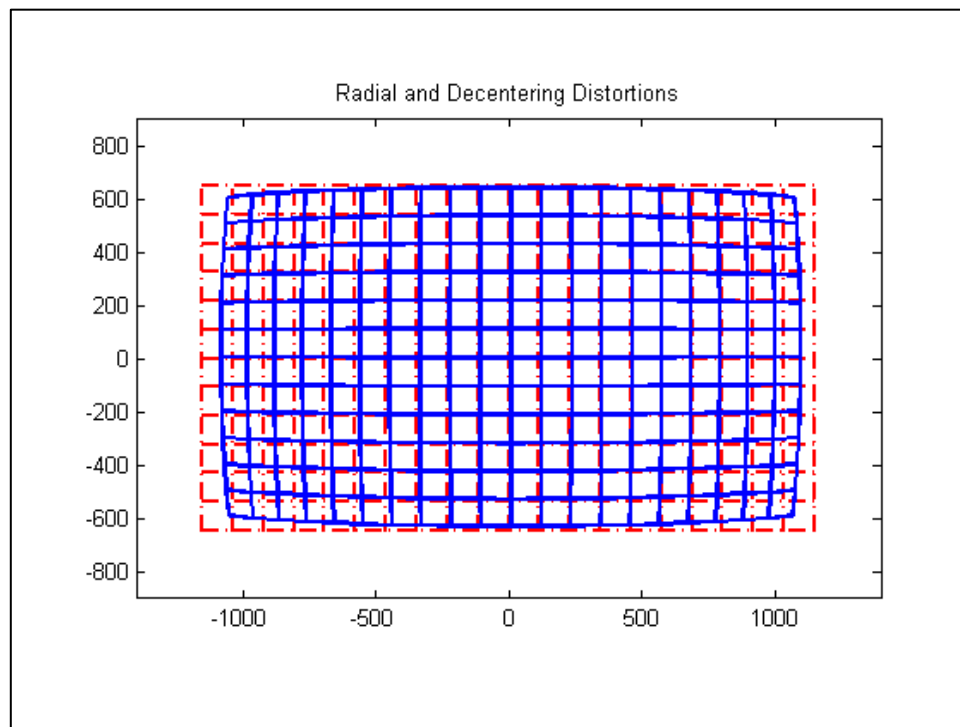


Figure 6.5 Grid Plot of Radial and Decentering Distortions of Urban 1 (Effects are exaggerated by  $\times 3$ )

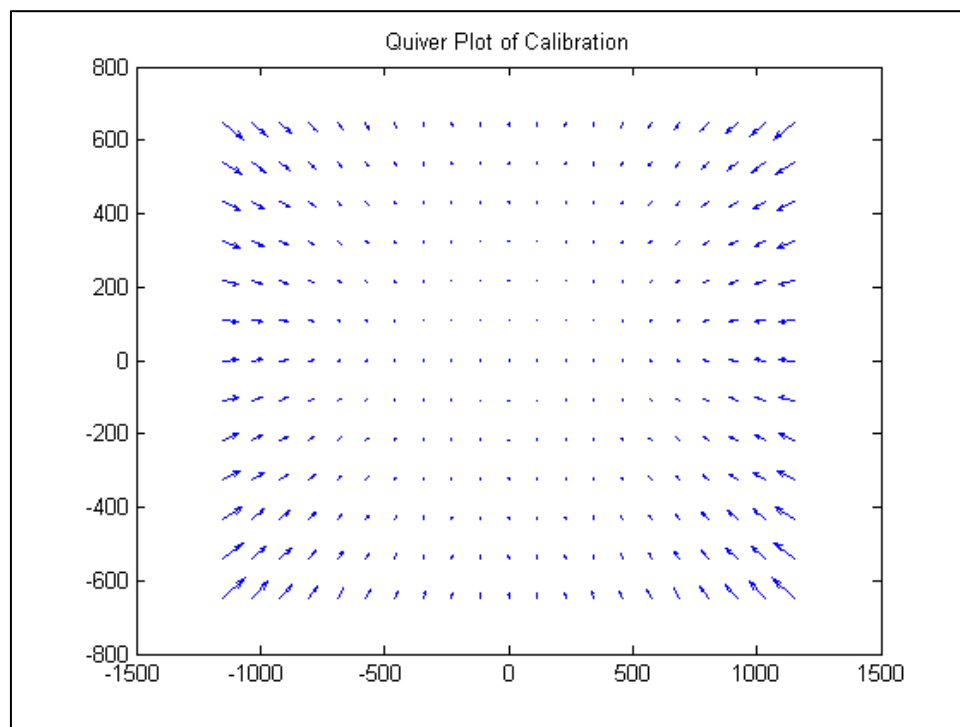


Figure 6.6 Quiver Plot of Urban 1 (Effects are exaggerated by  $\times 3$ )



Table 6.5 shows the result of the second of three calibration estimates using imagery from the urban scene. As before the uncertainty of the distortion parameters is quite large. Table 6.6 shows the observation residual. The residuals were also in a satisfactory range. Table 6.7 shows the correlation matrix of the calibration parameters and we can see the high correlations as before. Figure 6.7 shows the location of pass points with all points from all photographs overlaid. Figure 6.8 shows the grid plot of radial and decentering distortions and figure 6.9 shows the quiver plot of the second calibration. The radial and decentering plot and quiver plot show a similar shape as the first attempt.

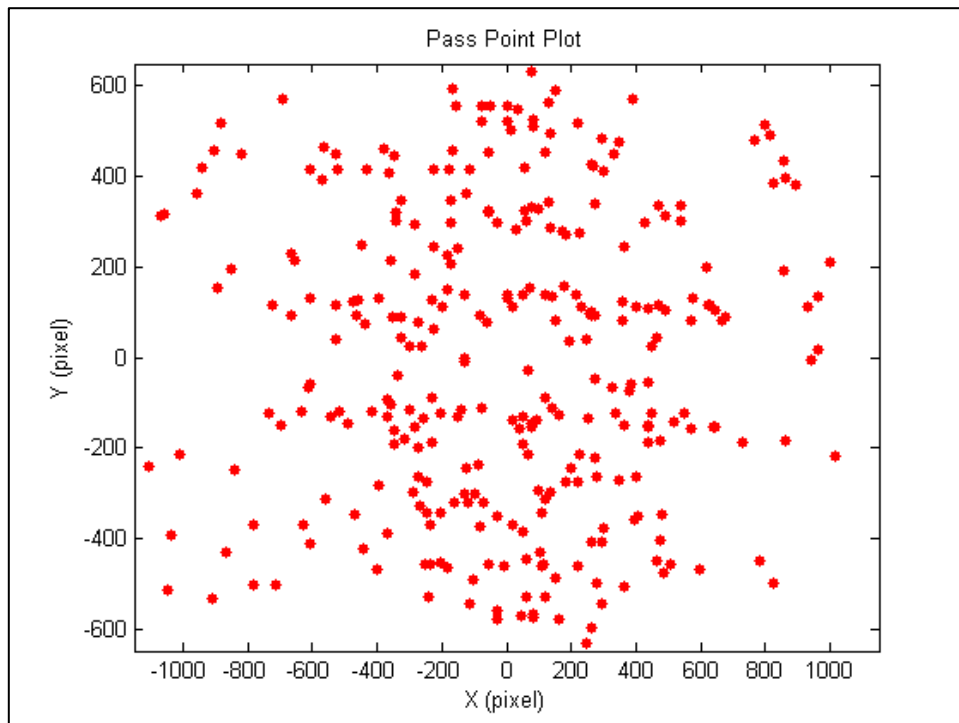


Figure 6.7 Pass Point plot of Urban 2  
(all points on all images overlaid)

Table 6.5 The Result of Calibration (Urban 2)

parameter	unit	value	$\sigma$	$\sigma$ (pixel)
$x_0$	(pixel)	-3.94	13.79	13.79
$y_0$	(pixel)	-22.33	12.04	12.04
$f$	(pixel)	2659.30	73.59	73.59
$K_1$		-1.56E-08	1.03E-08	2.19
$K_2$		1.16E-14	1.88E-14	3.65
$K_3$		-6.43E-21	8.93E-21	1.90
$P_1$		-2.39E-07	8.32E-07	0.31
$P_2$		14.28E-07	6.87E-07	0.26
Condition Number	1.70e+014			

Table 6.6 RMS of Residuals (Urban 2, units=pixels)

residual	$v_x$	$v_y$	mean
RMS	0.65	0.80	0.73

Table 6.7 Correlation Matrix of the Calibration Parameters (Urban 2)

	$x_0$	$y_0$	$f$	$K_1$	$K_2$	$K_3$	$P_1$	$P_2$
$x_0$	1.00	0.10	0.11	-0.04	0.00	0.02	-0.96	-0.09
$y_0$	0.10	1.00	-0.09	0.03	-0.01	0.00	-0.04	-0.93
$f$	0.11	-0.09	1.00	-0.15	-0.06	0.10	-0.02	0.09
$K_1$	-0.04	0.03	-0.15	1.00	-0.92	0.86	0.00	0.02
$K_2$	0.00	-0.01	-0.06	-0.92	1.00	-0.98	0.03	-0.05
$K_3$	0.02	0.00	0.10	0.86	-0.98	1.00	-0.04	0.06
$P_1$	-0.96	-0.04	-0.02	0.00	0.03	-0.04	1.00	0.04
$P_2$	-0.09	-0.93	0.09	0.02	-0.05	0.06	0.04	1.00

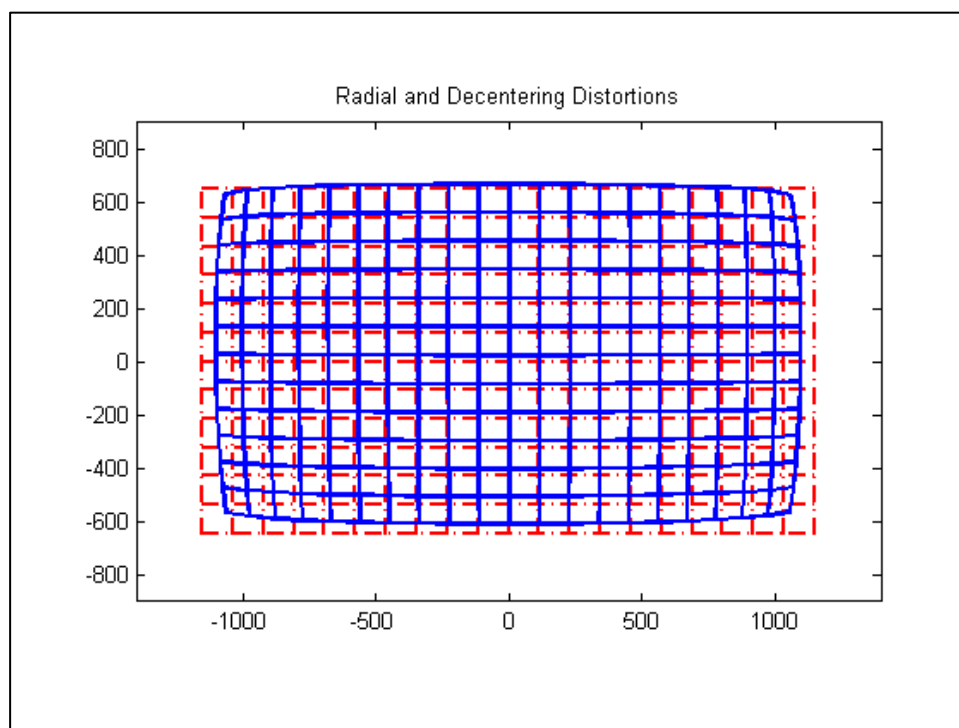


Figure 6.8 Grid Plot of Radial and Decentering Distortions of Urban 2 (Effects are exaggerated by  $\times 3$ )

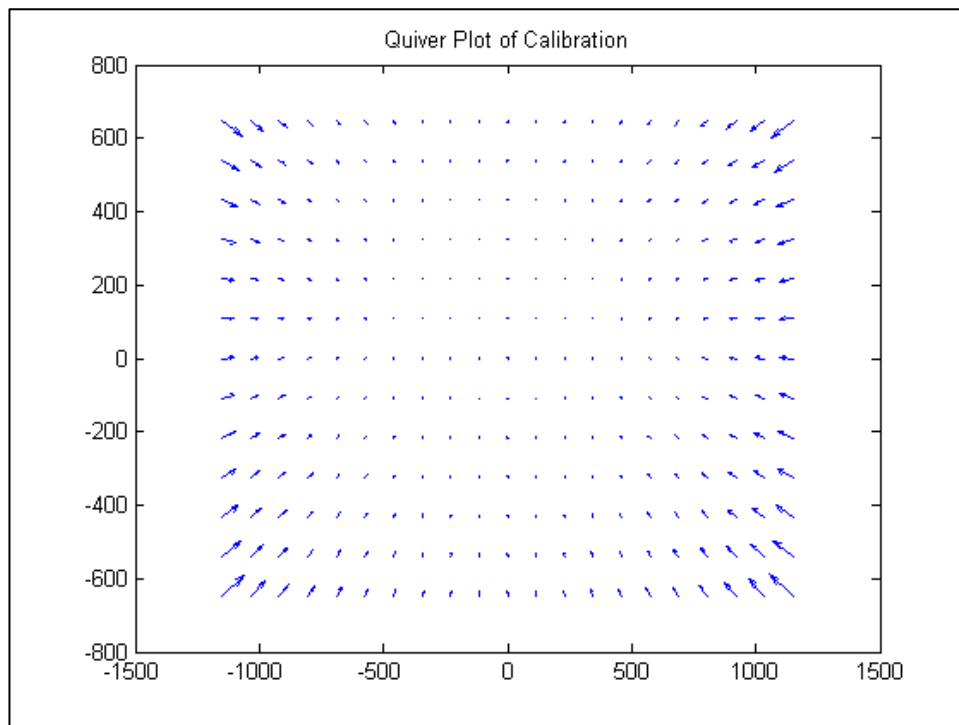


Figure 6.9 Quiver Plot of Urban 2 (Effects are exaggerated by  $\times 3$ )

Table 6.8 shows the result of the third of three calibration estimates using imagery from the urban scene. Table 6.9 shows the observation residuals. Table 6.10 shows the correlation matrix for the parameter vector. The correlations are similar to earlier results but the uncertainty was reduced for  $y_0$  and focal length. The cause of this will be discussed in subsequent pages. Figure 6.10 shows the location of pass points (all points on all photographs overlaid). Figure 6.11 shows the grid plot of radial and decentering distortion and figure 6.12 shows the quiver plot of the third calibration (urban imagery).

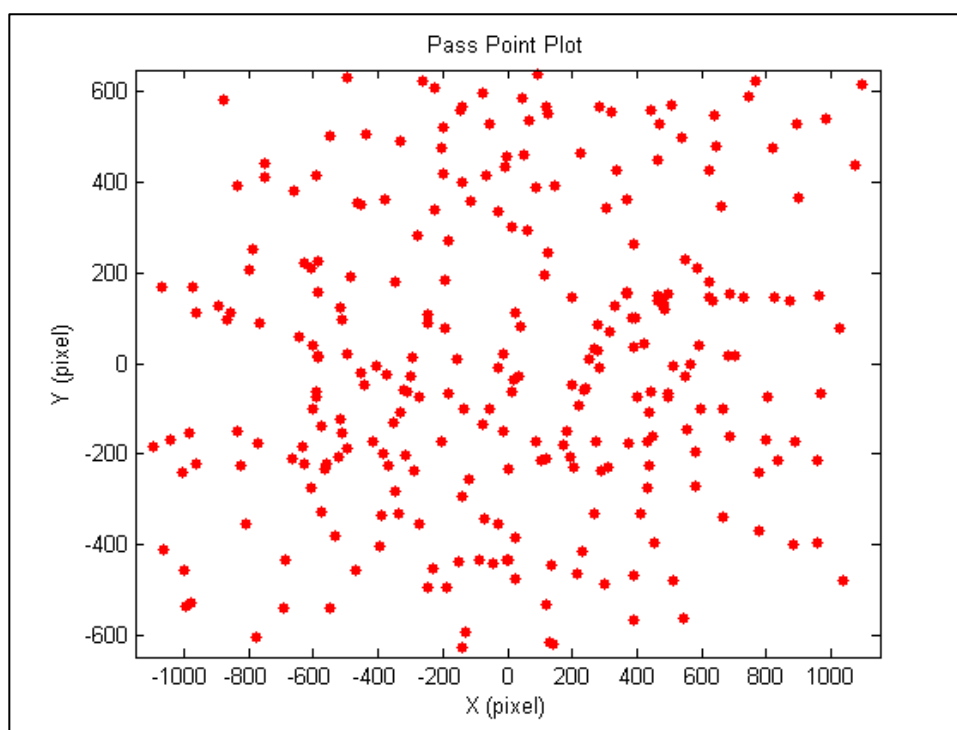


Figure 6.10 Pass Point Plot of Urban 3  
(all points on all images overlaid)

Table 6.8 The Result of Calibration (Urban 3)

parameter	unit	value	$\sigma$	$\sigma$ (pixel)
$x_0$	(pixel)	-3.78	11.85	11.85
$y_0$	(pixel)	-4.85	7.61	7.61
$f$	(pixel)	2763.18	49.35	49.35
$K_1$		-6.73E-09	10.24E-09	2.17
$K_2$		-1.49E-14	1.37E-14	2.66
$K_3$		8.61E-21	6.06E-21	1.29
$P_1$		-12.01E-07	6.34E-07	0.24
$P_2$		8.38E-07	3.9E-07	0.15
Condition Number	1.74e+14			

Table 6.9 RMS of Residuals (Urban 3, units=pixels)

residual	$v_x$	$v_y$	total
RMS	0.68	0.71	0.70

Table 6.10 Correlation Matrix of Calibration Parameters (Urban 3)

	$x_0$	$y_0$	$f$	$K_1$	$K_2$	$K_3$	$P_1$	$P_2$
$x_0$	1.00	0.19	0.01	0.13	-0.11	0.08	-0.96	-0.13
$y_0$	0.19	1.00	0.10	0.08	-0.07	0.06	-0.19	-0.84
$f$	0.01	0.10	1.00	-0.09	0.02	-0.02	-0.02	-0.08
$K_1$	0.13	0.08	-0.09	1.00	-0.93	0.86	-0.09	0.03
$K_2$	-0.11	-0.07	0.02	-0.93	1.00	-0.98	0.09	0.00
$K_3$	0.08	0.06	-0.02	0.86	-0.98	1.00	-0.07	0.00
$P_1$	-0.96	-0.19	-0.02	-0.09	0.09	-0.07	1.00	0.13
$P_2$	-0.13	-0.84	-0.08	0.03	0.00	0.00	0.13	1.00

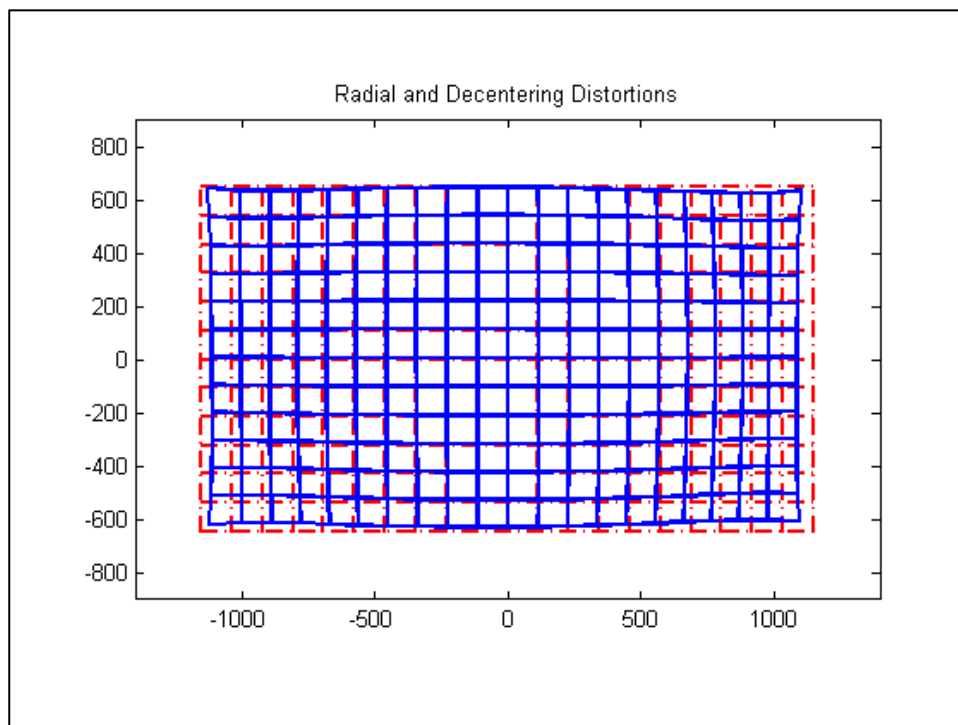


Figure 6.11 Grid Plot of Radial and Decentering Distortions of Urban 3 (Effects are exaggerated by  $\times 3$ )

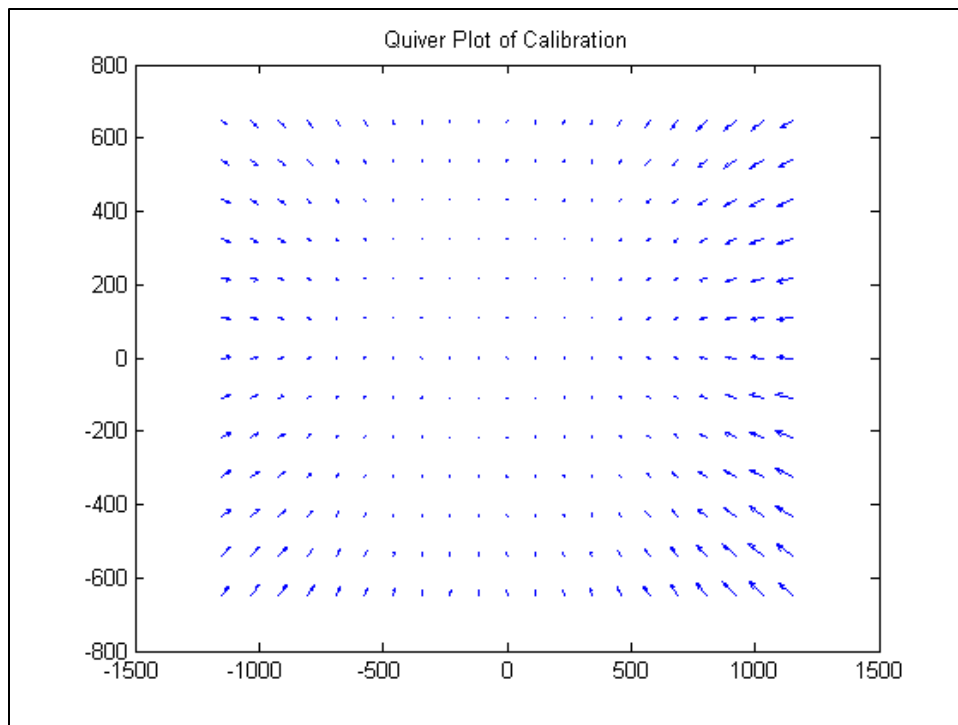


Figure 6.12 Quiver Plot of Urban 3 (Effects are exaggerated by  $\times 3$ )

To gain more insight into the camera calibration, two more conventional calibrations with signalized targets were implemented as shown in figures 6.13 and 6.14. In conventional calibration, space resection was used to initially approximate exterior orientation parameters. To get angle diversity, the video was taken at the each four corners of the room and the camera was rotated about 90 degrees once at each corner. Therefore there are total eight images for each experiment and table 6.11 – table 6.14 shows the result of calibration.

This experiment has another purpose which is to investigate the stability of the zoom optics. The camcorder was zoomed in and zoomed out a lot between each image. Similarity of calibration parameters would imply stability of the optics and it will be assessed by comparing the estimated parameters, the grid plot, and the quiver plot.

Both of the laboratory experiments showed small residuals in image space. When we compare two experiments with each other, they showed a similar overall tendency as shown in the radial and decentering plots, the quiver plots, Figures 6.16 – 6.17 and Figures 6.19 - 6.20. However, the fourth experiment showed positive  $y_0$  (5.03) whereas the fifth experiment showed negative  $y_0$  (-20.12). Also,  $P_2$  of Laboratory 2 was larger than that of Laboratory 1 by more than factor of 10. As mentioned above, the zooming in and out seemed to affect the calibration and the mechanical compartments in a consumer level camcorder don't seem to be as stable as photogrammetric quality equipment with fixed magnification optics. When we compare the last two experiments and the first

three experiments, the last two showed larger magnitude radial distortion compared to the first three experiments.



Figure 6.13 Calibration Targets for Laboratory 1





Figure 6.14 Calibration Targets for Laboratory 2

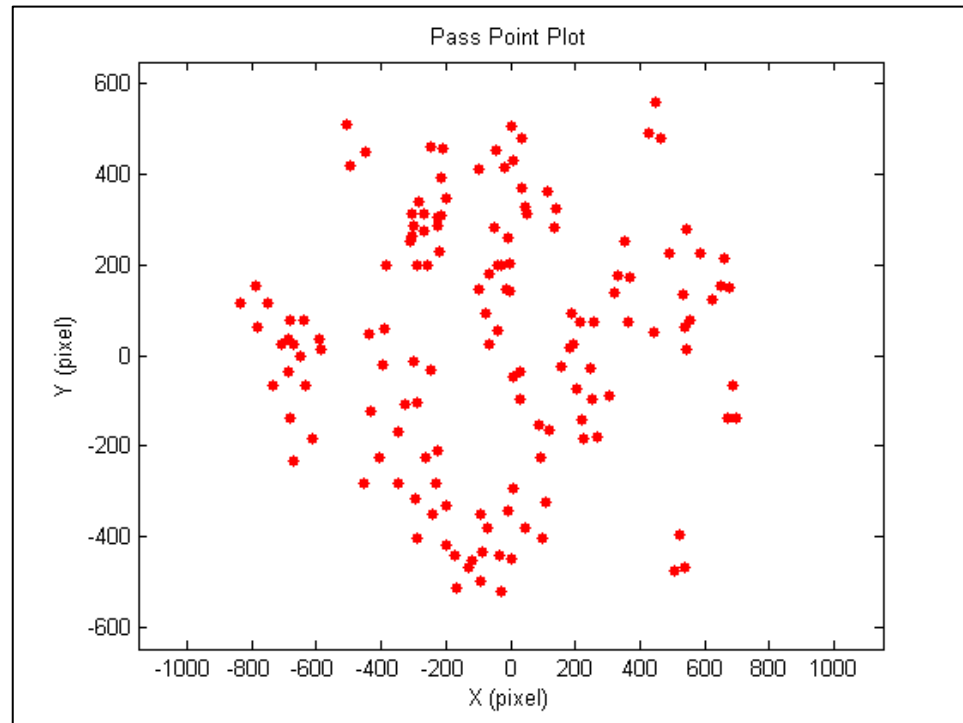


Figure 6.15 Pass Point Plot of Laboratory 1  
(all points on all images overlaid)

Table 6.11 The Result of Calibration (Laboratory 1)

parameter	unit	value	$\sigma$	$\sigma$ (pixel)
$x_0$	(pixel)	11.36	29.70	29.70
$y_0$	(pixel)	5.03	28.45	28.45
$f$	(pixel)	2749.38	19.72	19.72
$K_1$		-2.14E-08	1.68E-08	3.56
$K_2$		2.33E-14	4.69E-14	9.10
$K_3$		-1.63E-20	3.94E-20	8.38
$P_1$		-1.30E-06	1.75E-06	0.65
$P_2$		0.08E-06	1.76E-06	0.66
Condition Number	9.10*e+11			

Table 6.12 RMS of Residuals (Laboratory 1, units=pixels)

residual	$v_x$	$v_y$	Mean
RMS	0.22	0.27	0.25

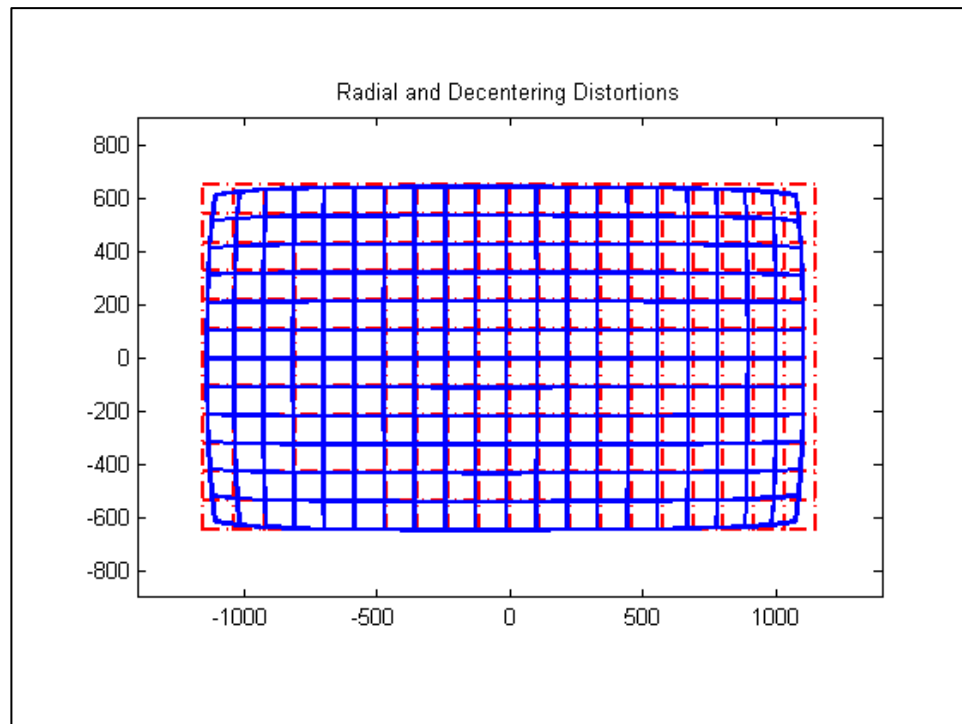


Figure 6.16 Radial and Decentering Distortions of Laboratory 1

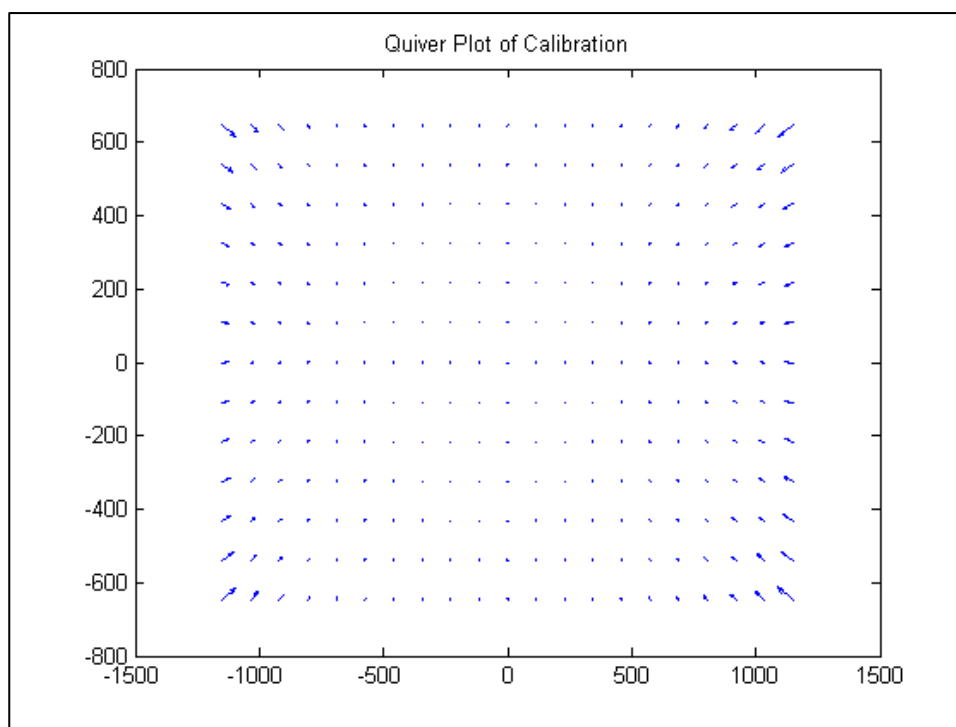


Figure 6.17 Quiver Plot of Laboratory 1

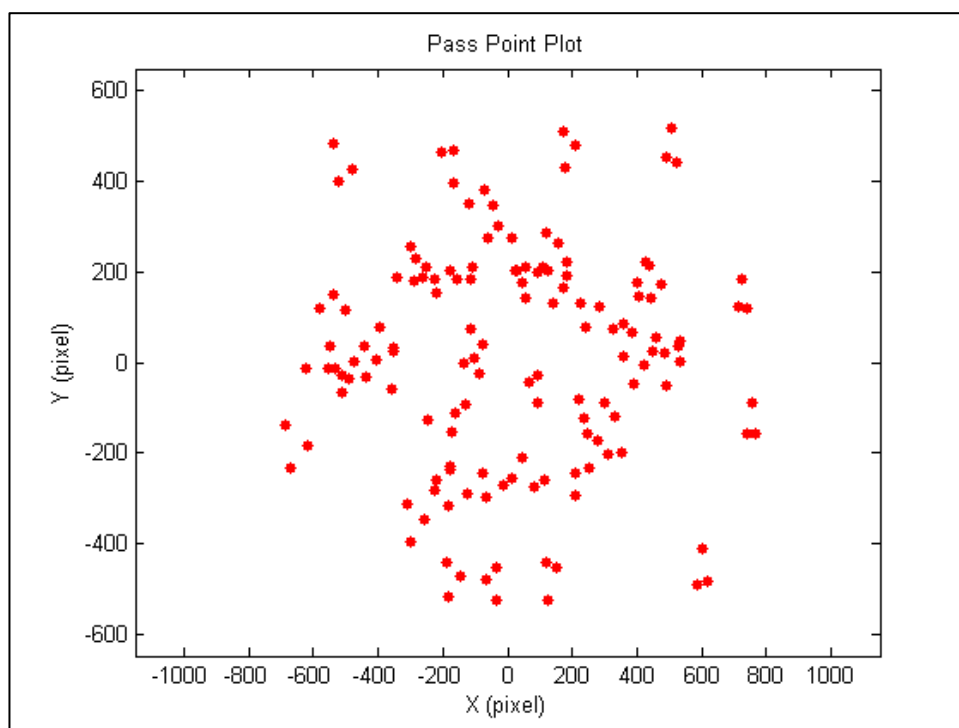
Figure 6.18 Pass Point Plot of Laboratory 2  
(all points on all images overlaid)

Table 6.13 The Result of Calibration (Laboratory 2)

parameter	unit	value	$\sigma$	$\sigma$ (pixel)
$x_0$	(pixel)	8.45	31.48	31.48
$y_0$	(pixel)	-20.12	33.30	33.30
$f$	(pixel)	2733.23	23.27	23.27
$K_1$		-2.67E-08	2.25E-08	4.77
$K_2$		3.76E-14	7.77E-14	15.08
$K_3$		-2.81E-20	8.06E-20	17.12
$P_1$		-1.52E-06	1.88E-06	0.70
$P_2$		0.95E-06	2.09E-06	0.78
condition Number	1.25e+013			

Table 6.14 RMS of Residuals (Laboratory 2, units=pixels)

residual	$v_x$ (pixel)	$v_y$ (pixel)	Mean (pixel)
RMS	0.22	0.25	0.23

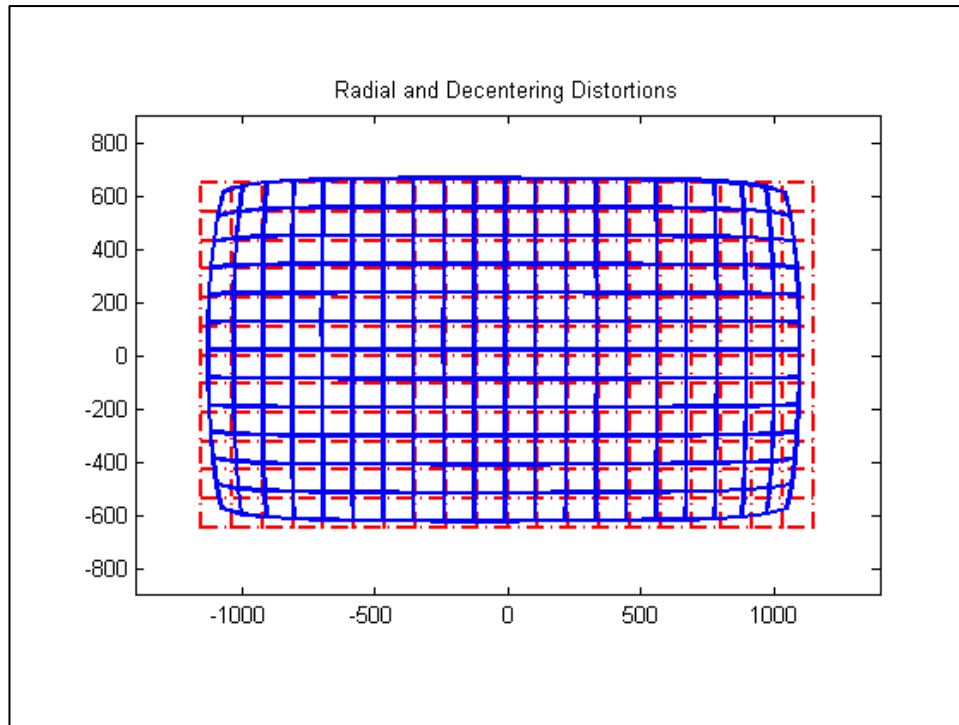


Figure 6.19 Radial and Decentering Distortions of Laboratory 2

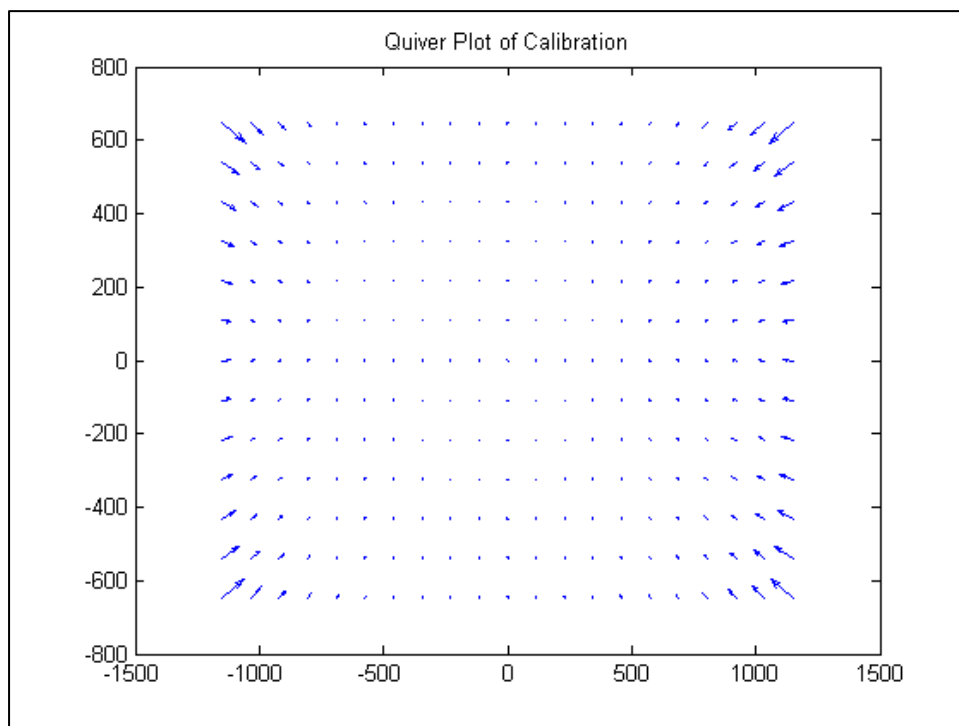


Figure 6.20 Quiver Plot of Laboratory 2

Since we have multiple results, not completely consistent, an independent method was chosen to evaluate them. A bundle block adjustment was performed with the aerial dataset from section 6.3 and the misclosures were compared at check points. The misclosure at the check points was used as a metric for calibration quality. The results are summarized in the table 6.15.

Table 6.15 The Comparison of Misclosures at Checkpoints for Each Calibration. Units are meters in object space. “group1” and “group2” refer to swapping the role of control and check points.

	RMS x (m)	RMS y (m)	RMS z (m)	RMS (m)
group1				
Urban 1	3.71	2.94	3.05	3.25
Urban 2	3.23	2.69	2.61	2.86
Urban 3	1.70	1.07	1.72	1.53
Laboratory 1	2.49	1.88	2.09	2.17
Laboratory 2	3.78	2.38	3.03	3.11
group2				
Urban 1	2.37	1.30	2.39	2.08
Urban 2	2.05	1.04	1.98	1.75

Table 6.15 Continued.

Urban 3	1.43	0.93	1.39	1.27
Laboratory 1	2.23	1.17	2.33	1.98
Laboratory 2	2.37	1.34	2.73	2.23
overall RMS				
Urban 1	3.11	2.27	2.74	2.73
Urban 2	2.71	2.04	2.32	2.37
Urban 3	1.57	1.00	1.56	1.41
Laboratory 1	2.36	1.57	2.21	2.08
Laboratory 2	3.15	1.93	2.88	2.71

To put table 6.15 in context, the ground sample distance (pixel size) in the oblique images ranged from 0.3 m to 3 m (foreground vs. background). As we can see in table 6.15, the bundle block adjustment with the camera parameters from the third calibration resulted in the smallest misclosures at the checkpoints. Table 6.16 shows the standard deviation for all internal camera parameters transformed into pixel units. The purpose of table 6.16 is to give an intuitive feeling for the influence of a parameter's uncertainty. Note also that in circumstances with high correlation, individual sigmas are often quite large whereas the uncertainty of the group of parameters is much smaller. Recall that



the first three were done with points from an urban scene, the fourth and fifth runs were from signalized targets in a lab setting. Since the calibration target points in experiment 4 and 5 cover only small portion of images, it gave poorer result than experiment 3. Therefore, the third calibration results were finally chosen as camera parameters which were used in the strip formation experiments in this research. The first reason why the third calibration showed the best determination of the camera parameters may be that the object distance was closer to the “infinity” focus distance. The second reason is that the photos were taken with a wider baseline and this made stronger geometry compared to the first and second calibration. The third reason is that the points were uniformly distributed including corners (figure 6.10) compared to the fourth (figure 6.15) and fifth cases (figure 6.18).

Table 6.16 The Comparison of Standard Deviations (units=pixels)

	$\sigma_{x_0}$	$\sigma_{y_0}$	$\sigma_f$	$\sigma_{K_1}$	$\sigma_{K_2}$	$\sigma_{K_3}$	$\sigma_{P_1}$	$\sigma_{P_2}$	Mean
calibration 1	13.75	11.02	73.41	2.22	3.87	2.00	0.32	0.24	13.35
calibration 2	13.79	12.04	73.59	2.19	3.65	1.90	0.31	0.26	13.47
calibration 3	11.85	7.61	49.35	2.17	2.66	1.29	0.24	0.15	9.42
calibration 4	29.7	28.45	19.72	3.56	9.1	8.38	0.65	0.66	12.53
calibration 5	31.48	33.3	23.27	4.77	15.08	17.12	0.7	0.78	15.81

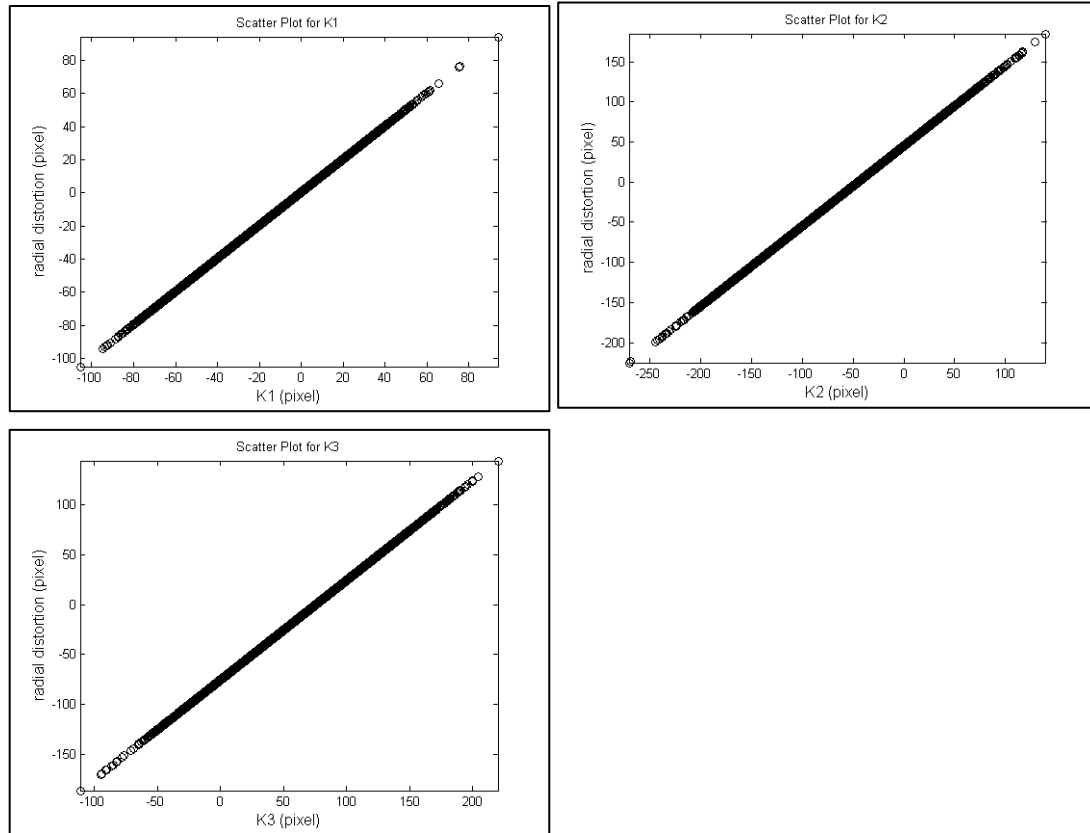


Figure 6.21 Radial Distortion according to  $K_1$ ,  $K_2$  and  $K_3$

For the results of Urban 3, the sensitivity of radial distortion to each coefficient of radial distortion was analyzed. By adding noise with sigma ten thousand times in table 6.8 to one of parameters of  $K_1$ ,  $K_2$  and  $K_3$ , the total radial lens distortion was plotted as figure 6.21. The range of radial distortion caused by each parameters were 199, 410, 331 pixels for each  $K_1$ ,  $K_2$  and  $K_3$ . Those ranges were too large because it was estimated without considering correlation between each parameter. Therefore, the sensitivity analysis for independent parameters was not relevant in this case. Therefore, ten thousand  $K_1$ ,  $K_2$ ,  $K_3$  was

randomly generated by perturbing  $K_1$ ,  $K_2$ ,  $K_3$  with  $\sigma$  considering the correlation between each parameter described in table 6.10. The range of the radial distortion contributed from  $K_1$ ,  $K_2$ , and  $K_3$  became 188, 153, 45 pixels and it was found out that the range of the radial distortion from  $K_2$ ,  $K_3$  were reduced. Figure 6.22 shows the point distribution without and with correlation.

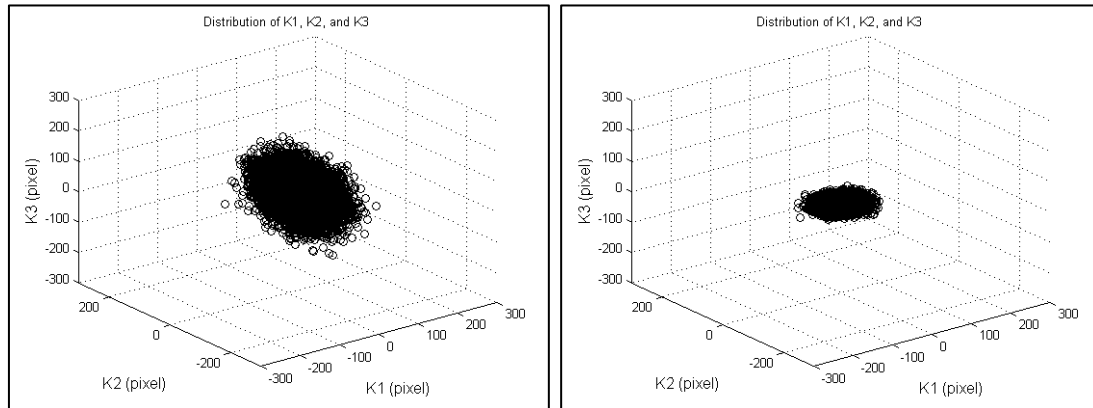


Figure 6.22 The distribution of the contribution of  $K_1$ ,  $K_2$  and  $K_3$  (Left: Uncorrelated, Right: Correlated)

### 6.1.2 Calibration from Aerial Imageries

For the experiments in aerial strip formation, calibrated camera parameters from section 6.1 were used as described. However, prior calibration is not available always and it is useful to compare the results from an uncalibrated sensor using “self-calibration” versus the results from a calibrated sensor. The same dataset and configuration described in section 6.3 were used with the “nominal” interior orientation parameters found in table 6.17.

Table 6.17 Interior Orientation Parameters for Uncalibrated Camera

PAR	$x_0$ (px)	$y_0$ (px)	$f$ (px)	$K_1$	$K_2$	$K_3$	$P_1$	$P_2$
value	0	0	2341.6	0	0	0	0	0

For “self-calibration”, a camera can be calibrated in BBA by carrying the camera interior parameters as before, but with project imagery rather than special calibration imagery. For the BBA, equations (4.68) and (4.69) are used as condition equations. The parameters carried are interior ( $x_0$ ,  $y_0$ ,  $f$ ,  $K_1$ ,  $K_2$ ,  $K_3$ ,  $P_1$ ,  $P_2$ ) and exterior orientation ( $X_L$ ,  $Y_L$ ,  $Z_L$ ,  $\omega$ ,  $\phi$ ,  $\kappa$ )<sub>i</sub>, and object space coordinate ( $X$ ,  $Y$ ,  $Z$ )<sub>j</sub> of control points and pass points in the ground or object coordinate system. The BBA was solved by Unified Least Squares (also known as regularization or Bayesian parameter estimation), and the *a priori* standard deviations for interior orientation parameters are given in table 6.18. The *a priori* standard deviations for the rest of the parameters are the same as section 6.5. Table 6.19 shows the result of self calibration.

Table 6.18 *A Priori* Standard Deviations for Interior Orientation Parameters (sigmas chosen to represent “unknown” parameters)

	$x_0$ (pixel)	$y_0$ (pixel)	$f$ (pixel)	$K_1$ (pixel)	$K_2$ (pixel)	$K_3$ (pixel)	$P_1$ (pixel)	$P_2$ (pixel)
$\sigma$	1000	1000	1000	100	100	100	100	100

Table 6.19 The Result of Self Calibration Using Aerial Imagery (groups interchange of control and check points)

parameter	unit	Value	$\sigma$	$\sigma$ (pixel)
1 <sup>st</sup> group				
$x_0$	(pixel)	-247.41	56.20	56.20
$y_0$	(pixel)	160.03	98.95	98.95
$f$	(pixel)	2908.79	70.91	70.91
$K_1$	1.00E-07	1.18	0.14	2.93
$K_2$	1.00E-13	-1.28	0.17	3.23
$K_3$	1.00E-20	3.59	0.58	1.23
$P_1$	1.00E-05	4.25	0.20	0.73
$P_2$	1.00E-07	8.53	7.37	0.28
2 <sup>nd</sup> group				
$x_0$	(pixel)	-13.09	39.01	39.01
$y_0$	(pixel)	1.16	93.62	93.62
$f$	(pixel)	2848.20	79.27	79.27
$K_1$	1.00E-08	8.51	2.17	4.60
$K_2$	1.00E-13	-3.26	0.35	6.81
$K_3$	1.00E-19	1.70	0.16	3.35
$P_1$	1.00E-06	-6.27	1.71	0.64
$P_2$	1.00E-06	8.52	0.76	0.28

Table 6.20 RMS of Residuals for Self Calibration (units=pixels)

	x	y
group 1	0.43	0.48
group 2	0.36	0.82

Table 6.21 RMS Misclosure at Check Points (units=meters)

	x	y	z	total
group 1	42.26	20.05	33.90	33.35
group 2	19.22	10.39	16.78	15.91

Table 6.20 shows the RMS of observation residuals, which are in an acceptable range, and Table 6.21 shows the RMS misclosures at check points. The misclosures for self calibration were larger than those of calibration Urban 1,2,3, and Laboratory 1, 2. The advantages of doing calibration with the aerial project data are: (1) there are many points to cover all areas of the image format, and (2) the object distance truly matches the focus setting of “infinity”. The disadvantage is that there is very little angle diversity among the strip of imagery. If one planned to do calibration with aerial imagery, one would fly the strip three or four times, each with different camera orientation.

Considering all of the factors, experiment three was chosen to represent the best calibration for this camera. Recall it had angle diversity, long object distance, and small misclosures at the checkpoints for the aerial data.

## 6.2 APPLICATION 2: Automated Relative Orientation -Terrestrial Case

The automated relative orientation procedure was implemented with terrestrial video frames. The data was acquired from a moving car by taking videos of the Purdue ITAP building as described in table 6.22. The image frames were selected from the video stream with configuration parameters described in table 6.23. Figure 6.23 shows the input images for automated relative orientation procedure.

Table 6.22 Data Acquisition

Date/Time Taken	Vehicle Type	Instrument	Object	Speed
10/15/2009 17:00	Passenger Car	Sony High Definition Camcorder HDR-CX100 (30 FPS)	Purdue ITAP building	3.2 km/hr

Table 6.23 Data Description

Capturing Time-gap	Overlap Ratio	Width (px)	Height (px)	Format	No. Frame
3 sec	0.7	2304	1296	JPEG	5



Figure 6.23 Input Data to Automated Relative Orientation

The captured image frames were processed by the algorithms described in sections 4.1 and 4.2 to detect and match interest points in each adjacent pair of images, using algorithm tuning parameters described in table 6.24. To ensure uniform distribution of matched points, two points were chosen from each quadrangle of the overlapping region of image pairs as shown in figure 6.24. These eight points (four pairs) were chosen randomly many times to enumerate inliers and outliers by the RANSAC procedure. The correlation window size was



chosen to be large in this particular case because the patterns on the red bricks, the white panels, and the gray roof areas were ambiguous with small window size. To handle this problem, the correlation window size was chosen as the approximate, apparent height dimension of the brick region, the panel region and the roof region. For the scale restraint points, one point was measured manually considering the best position possible.

Table 6.24 Parameter Setup

Baseline (m)	Correlation Window (pixel)	RANSAC Threshold	Outlier Probability $e$	RANSAC Accuracy
2.6667	225×225	1.0e-2	0.5	99%

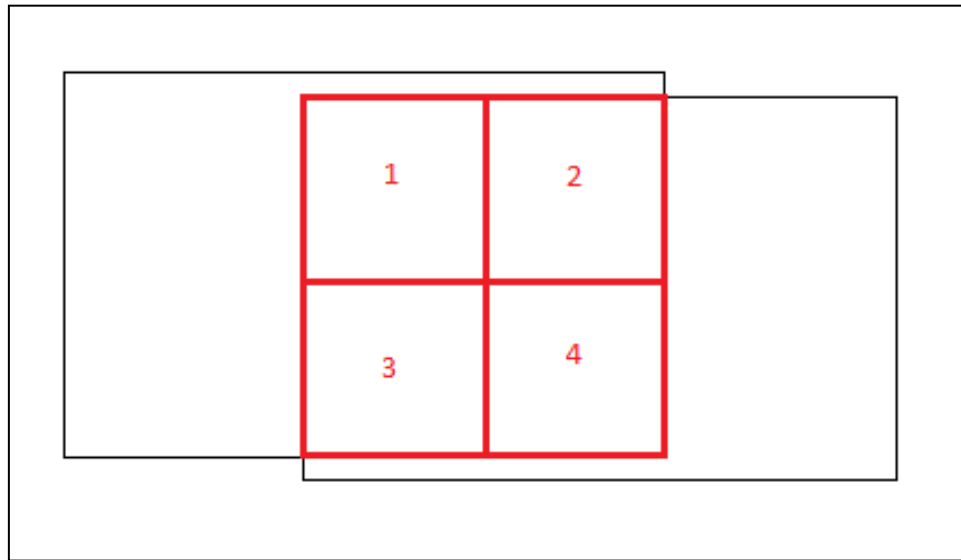


Figure 6.24 Subregion for Sampling Points

In figure 6.25, black and white checkerboard markers show the interest points detected and matched automatically for each pair of images, and I have found that the detection and matching were successful.

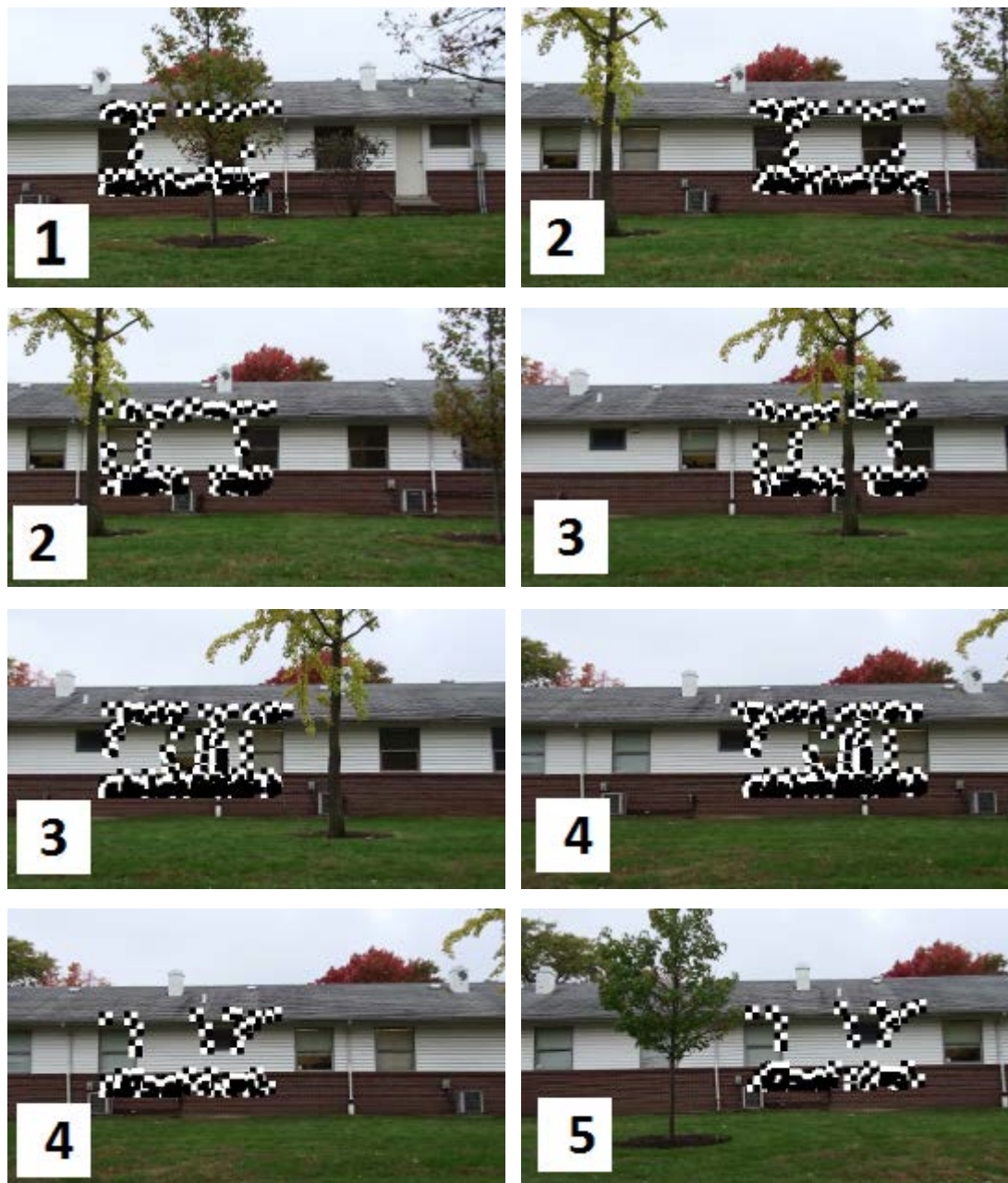


Figure 6.25 Matched Points in Terrestrial Images

With the coordinate information of the matched points, the strip formation problem by relative orientation could be solved by SLS, CLS, and KF as described in chapter 5. Since there is no control point information for this terrestrial case, the covariance of the white noise term for SLS was estimated from SLS without the state transition expression. For the first pair of images, one of the exterior orientation parameters must be fixed, and  $b_x$  was chosen to be fixed. Table 6.25 - Table 6.27 show the exterior orientation parameter estimation results from SLS, CLS and KF. Table 6.28 shows the observation residuals for each solution. SLS and KF showed similar residual RMS, and CLS had larger residual RMS. The residual RMS of every solution was less than 1 pixel and the relative orientation procedure was successful in image space.

Table 6.25 Exterior Orientation Parameters from SLS

image	$X_L$ (m)	$Y_L$ (m)	$Z_L$ (m)	$\omega$ (Rad)	$\phi$ (Rad)	$\kappa$ (Rad)
1	0.00	0.00	0.00	0.00	0.00	0.00
2	2.67	0.05	-0.04	0.00	0.01	0.01
3	5.34	0.09	-0.09	0.00	0.02	0.01
4	8.11	0.14	-0.14	0.00	0.00	0.01
5	10.94	0.18	-0.14	-0.01	-0.01	0.00

Table 6.26 Exterior Orientation Parameters from CLS

image	$X_L$ (m)	$Y_L$ (m)	$Z_L$ (m)	$\omega$ (Rad)	$\phi$ (Rad)	$\kappa$ (Rad)
1	0.00	0.00	0.00	0.00	0.00	0.00
2	2.67	0.05	-0.04	0.00	0.01	0.01
3	5.34	0.09	-0.09	0.00	0.02	0.01
4	8.11	0.14	-0.14	0.00	0.00	0.01
5	10.94	0.18	-0.14	-0.01	-0.01	0.00

Table 6.27 Exterior Orientation Parameters from KF

image	$X_L$ (m)	$Y_L$ (m)	$Z_L$ (m)	$\omega$ (Rad)	$\phi$ (Rad)	$\kappa$ (Rad)
1	0.00	0.00	0.00	0.00	0.00	0.00
2	2.67	0.05	-0.04	0.00	0.01	0.01
3	5.34	0.09	-0.09	0.00	0.02	0.01
4	8.11	0.14	-0.14	0.00	0.00	0.01
5	10.94	0.18	-0.14	-0.01	-0.01	0.00

Table 6.28 Observation Residuals of Each Solution (RMS, units=pixels)

	$v_x$	$v_y$
CLS	0.019	1.146
KF	0.003	0.331
SLS	0.003	0.295

Table 6.29 RMS Discrepancy of CLS and KF from SLS

	CLS (cm)	KF (cm)
RMS_X	0.01	0.01
RMS_Y	0.00	0.00
RMS_Z	0.01	0.08
RMS_Total	0.01	0.05

Table 6.29 shows the RMS discrepancy of selected pass points between CLS, SLS and KF. In table 6.29, the differences of each result were below centimeter level. Figures 6.26 - 6.28 show the comparisons of RMS of X, Y and Z coordinates of intersected points for each model. For these figures the SLS coordinate estimate is taken as the reference value and shifted to exactly zero, and the scale of y axis is exaggerated by 43. The KF and CLS are shown relative to this reference. This is not an absolute evaluation. For the aerial case, I chose to make an absolute evaluation by including control points and check points. We can see there is no significant difference between these approaches. This is likely due to the short length of the strip. Also, the precision of each solution was evaluated by estimating the error ellipsoid with 90% confidence level. As it can be seen in table 6.30 and figure 6.29, the KF's error ellipsoid was the smallest (factor of 0.8 to CLS in semi major axis). The SLS's error ellipsoid was the largest (factor of 3.4 to CLS in semi major axis). In figure 6.29, Z axis for error ellipsoid is camera axis, not elevation. The differing results describing precision conflict with (a) our intuition, which leads us to regard the simultaneous solution, SLS, as a more complete & rigorous model, and (b) later numerical results which

confirm that SLS yields the best absolute accuracy. My conclusion is that CLS and KF, by using simplified models, really understate the propagated variability of the point coordinates (precision). In the aerial and simulation cases, the external comparison of solution by estimation of misclosures of check points will be implemented to find the real accuracy. To expand the priori explanation of inconsistency between precision and accuracy, the model differences will be presented. The model differences will cause the estimated precisions of CLS and KF to be unrealistically small. When the EO parameters of any image are estimated from CLS and KF, the scale restraint equation included in the estimation is only one. For example, the EOs of image 3 are estimated by scale restraint equation composed from the image (1, 2, 3). However, the number of scale restraint equations is three in SLS when estimating the EO parameters of any one image. For example, the EOs of image 3 are estimated by three scale restraint equations composed from the image triplets (1, 2, 3), (2, 3, 4) and (3, 4, 5). See Figure 6.30. The SLS model is thus more complete and rigorous. This appears to inflate the precision estimates for SLS, but actually the precision estimates for CLS and KF are understated.

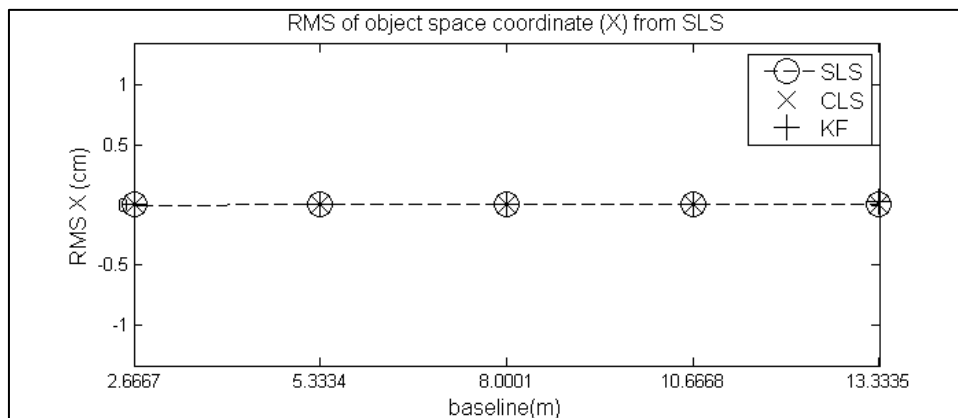


Figure 6.26 Comparison of X Coordinates

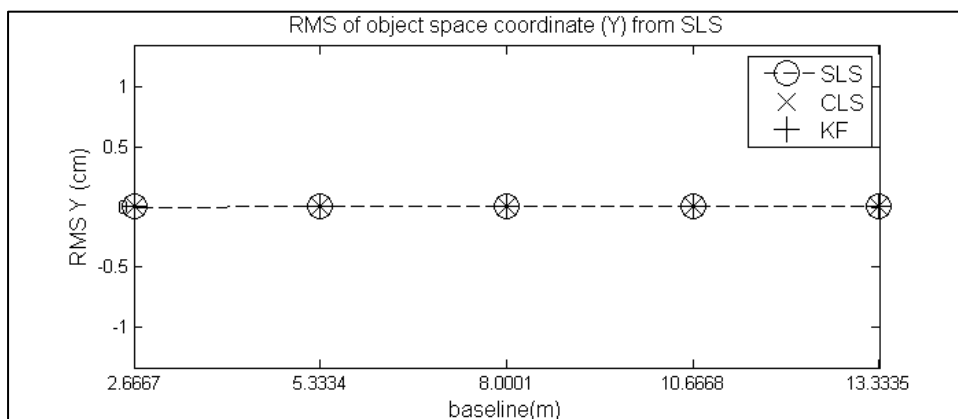


Figure 6.27 Comparison of Y Coordinates

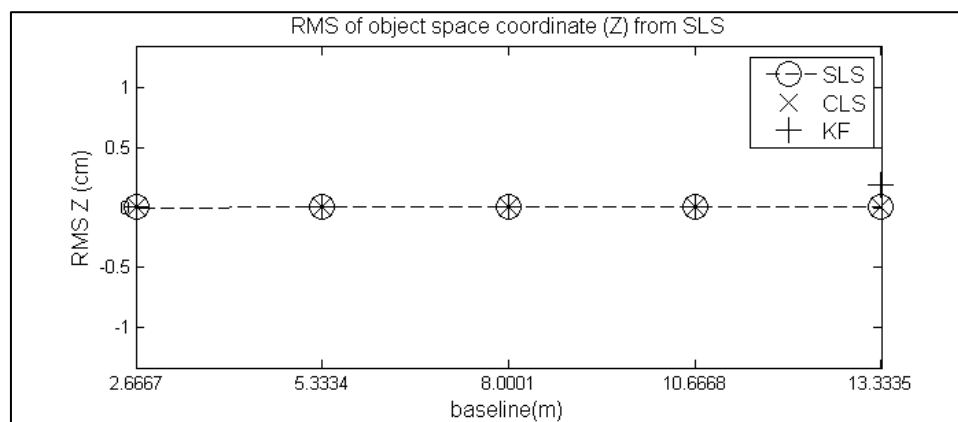


Figure 6.28 Comparison of Z Coordinates

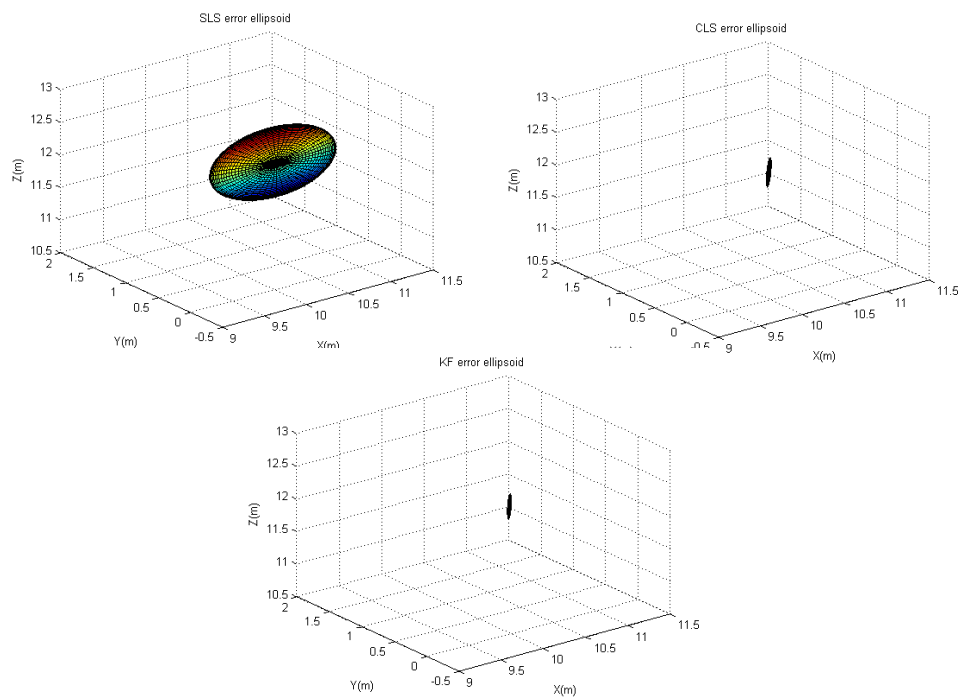
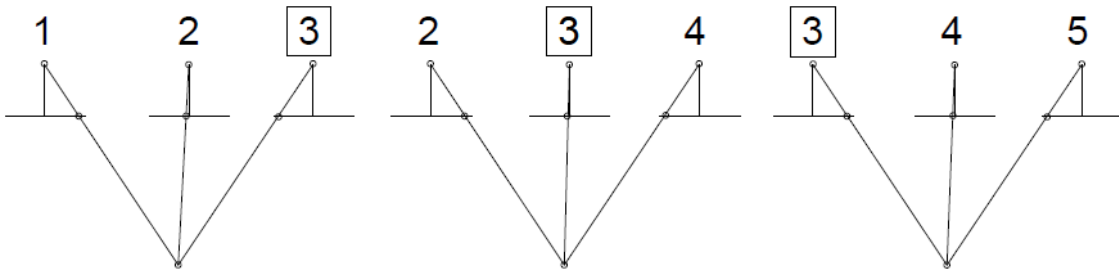
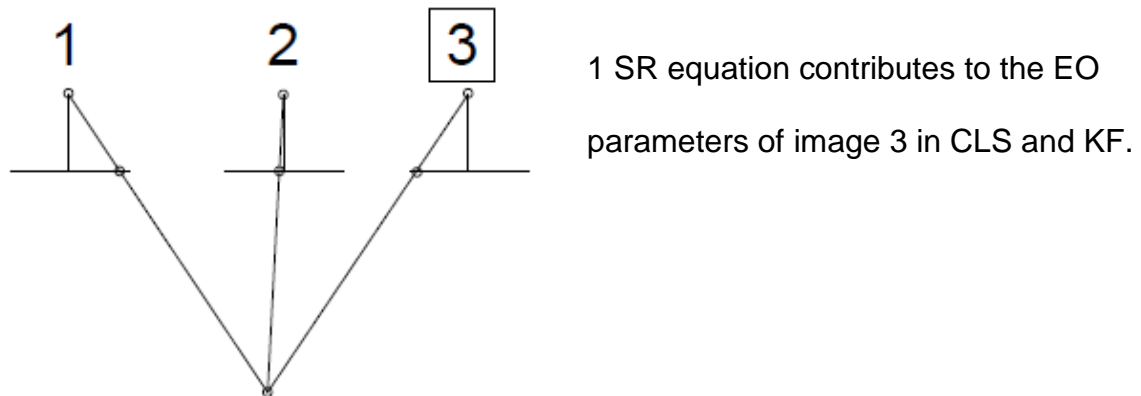


Figure 6.29 Error Ellipsoids from Each Approach (SLS Top Left, CLS: Top Right, KF: Bottom Center)

Table 6.30 Semi Major and Minor Axis of Error Ellipsoid

	semi major	semi minor 1	semi minor 2
SLS	0.74	0.65	0.04
CLS	0.22	0.02	0.01
KF	0.19	0.02	0.01





3 SR equations contribute to the EO parameters of image 3 in SLS.

Figure 6.30 Scale Restraint Equations

Table 6.31 shows the memory occupancy of each solution to see the extent of computing resources each solution requires. Ranking from high to low by memory resources yields: SLS, KF and CLS. CLS and KF showed far smaller values for memory occupancy because at each epoch, they only estimate the parameters in the state vector rather than the entire strip.

Table 6.31 Memory Occupancy of Each Solution

	CLS	SLS	KF
memory (MB)	2.51	93.34	2.89

### 6.3 APPLICATION 3: Automated Relative Orientation – Aerial Case

In this application, bundle block adjustment and absolute orientation were also implemented to assess the accuracies of SLS, KF, and CLS. By the use of control point information, absolute orientations with both seven parameter (rigid body) transformation and polynomial transformation were implemented. The results were assessed with the misclosures at check points. Also, a similar evaluation was done using check points from bundle block adjustment.

#### 6.3.1 Relative Orientation

The aerial data was acquired from a Cessna aircraft with the HD camcorder as shown in table 6.32. The image data was captured from a video stream as shown in Table 6.33. Figure 6.31 shows the images which were used for the experiment. There are 15 frames sampled at 2 second intervals (extracted for video stream), which cover most of the northern campus area of Purdue University, West Lafayette. The overlap ratio was approximately 0.8 in the foreground and a larger value in the background (the images are oblique). The base – height ratio in the foreground was approximately 0.17. Since this is weak

geometry for determining ground coordinates, a strategy to increase the base – height ratio was sought. The simplest way to get a dataset with a larger base height ratio is to increase sampling time between each image frame. In this case it did not require another photo mission, only selecting frames from the video stream with larger time interval between them.

Table 6.32 Aerial Data Acquisition

Date/Time Taken	Vehicle Type	Instrument	Flight area	Flight time	Note
5/3/2010 14:00	High-wing Cessna Aircraft (like a 172)	Sony High Definition Camcorder HDR-CX100 (30FPS)	Purdue Campus, West Lafayette, IN	45 minute	Bank during flight to permit oblique imagery capture through the passenger window

Table 6.33 Data Description

Sampling interval	Overlap Ratio	Width (px)	Height (px)	Format	No. original Frame	No. final frame (@ 4 sec)
2 seconds	0.8	2304	1296	JPEG	15	8

Table 6.34 The Parameters for Interest Point Detection and Matching

Harris Laplace Scale no.	Correlation window size (px)	Pyramid numbers for correlation	RANSAC accuracy	Expected matching error	RANSAC threshold
3	31	3	0.9	0.5	1.0e-2

However, this will decrease the performance of any cross correlation matching because the larger base causes more parallax. To address this problem, the following strategy was adopted. Let's call the originally selected frames 1, 2, 3,..., 15. If we adopt every second image in this sequence, the new strip will consist of 1, 3, 5, 7, 9, 11, 13, and 15. This new strip will have approximately twice the base - height ratio as the original strip. To address the issue of more difficult cross correlation, the following was done. Matching interest points was very successful between 1 and 2, 2 and 3, 3 and 4, etc. But it became challenging to match directly 1 and 3, 3 and 5, etc. So I retained the concept of matching between the original adjacent images 1 and 2, 2 and 3, etc. This was followed by matching the two sets of points on image 2, the 1-2 group and the 2-3 group. For every common point on image 2, we have implicitly found a match between image 1 and 3. So this strategy was used throughout the new strip. That means, of course, that for a photo collection mission, one needs to capture the images to be used in the strip formation, but also intermediate images to help with the matching/correspondence problem.

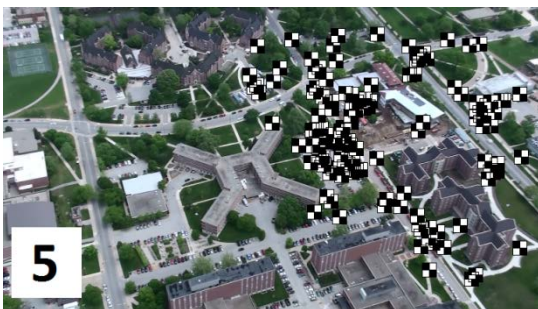
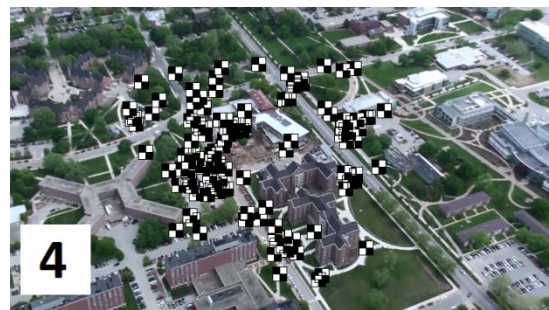
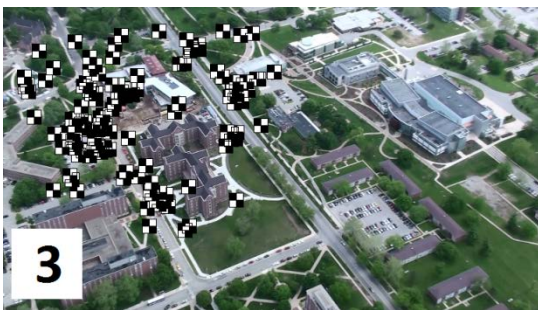
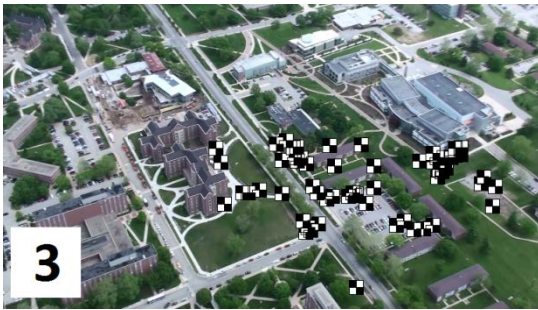
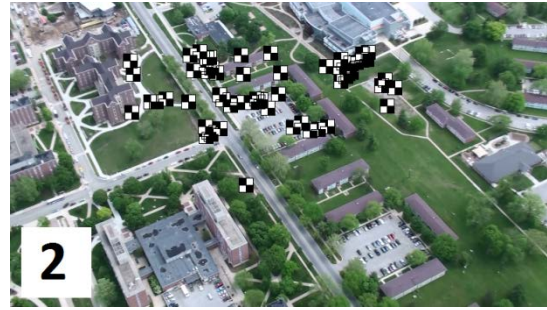
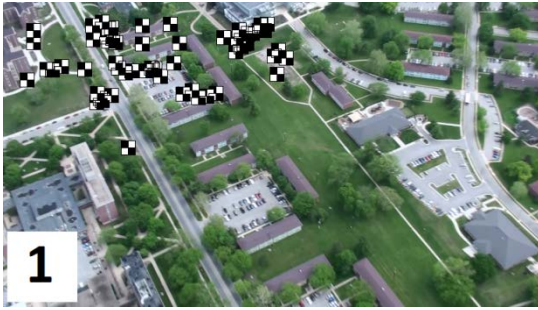
A related problem involves getting common points between image 1, 3, and 5 for the scale restraint equation. This was deemed too difficult for automation so one scale restraint point for each model was measured manually. Future research could address this high B/H matching problem. Table 6.34 shows the parameters for corner detection and matching and figure 6.32 shows the images selected for this experiment. As explained above, only the images in left columns (image 1, 3, 5, 7, 9, 11, 13, 15) were used as input for the strip formation by relative orientation. But the other (intermediate images) were used as described for the “bridge matching” procedure.



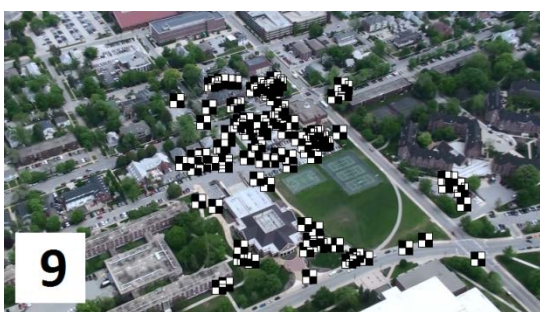
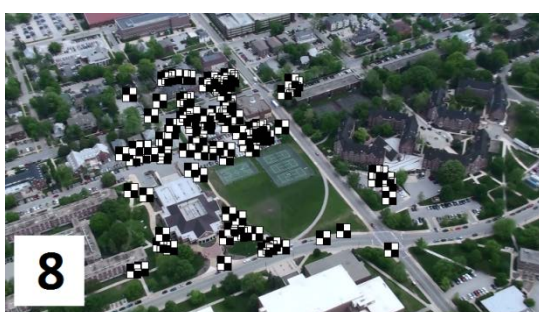
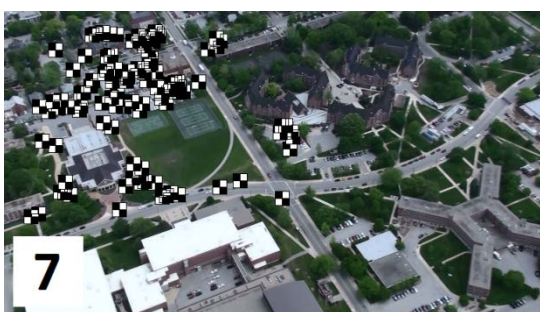
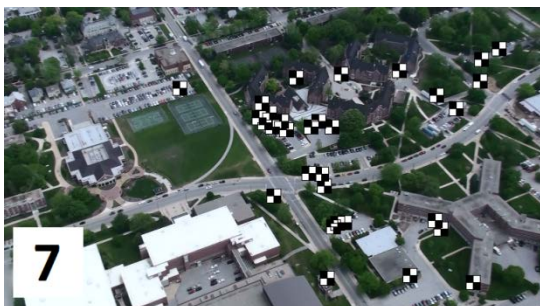
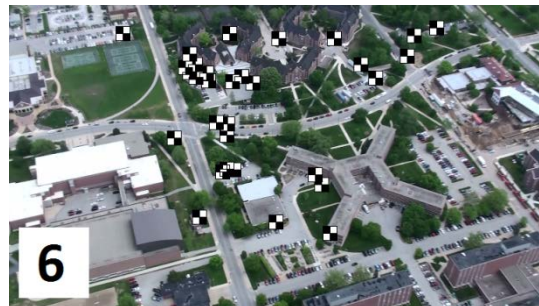
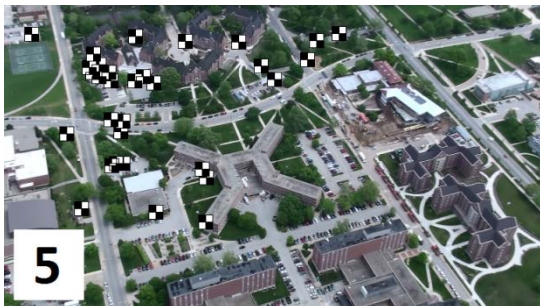


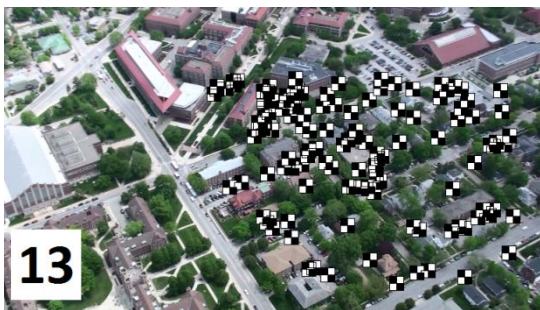
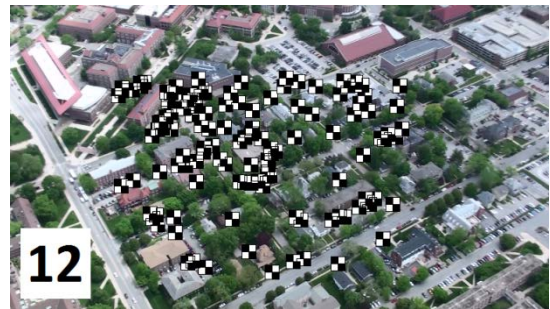
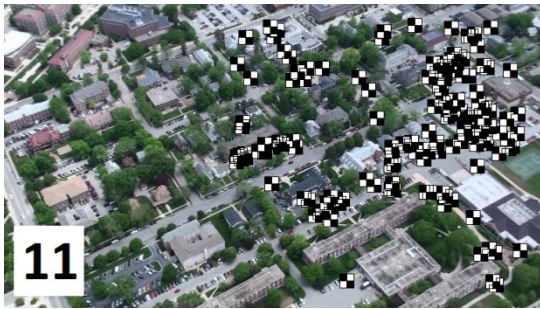
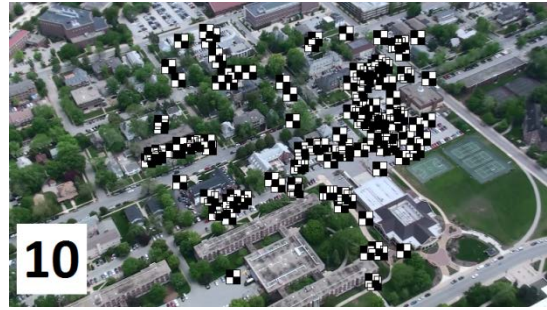
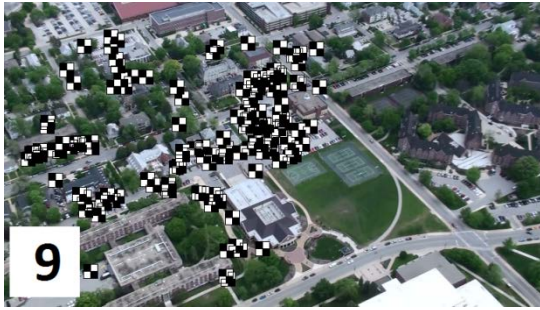


Figure 6.31 Aerial Dataset over Purdue Campus











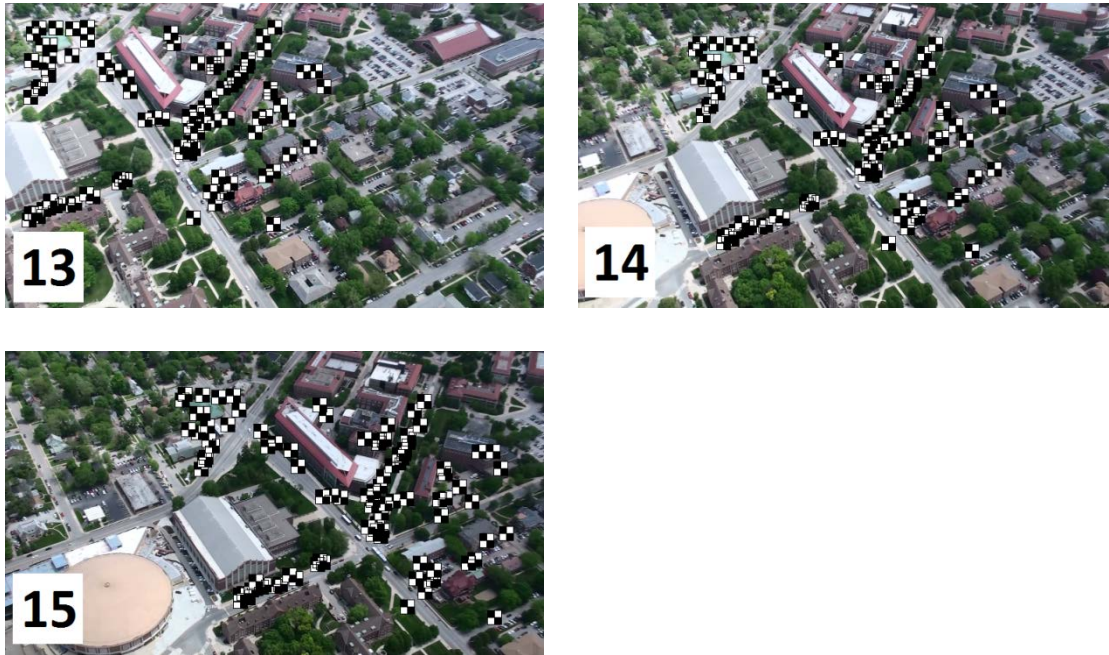


Figure 6.32 Matched Points for Each Pair of Images 1-3, 3-5, 5-7, 7-9, ... . The intermediate images are also shown. The images are organized as triplets.

In Figure 6.32, the black and white checkerboard markers show the interest points detected and matched automatically for each triplet of images, and using the strategy described earlier, the detection and matching were successful. With the coordinate data for the matched points, the relative orientation and strip formation problem could be solved by SLS, CLS, and KF as described in chapter 5. For the first model,  $b_x$  was fixed at its true value (187 m).

Table 6.35, 6.36 and 6.37 show the exterior orientation parameters estimated from each approach. Table 6.38 shows the RMS in image space of residuals from each solution. They are all in the sub-pixel range.

Table 6.35 Exterior Orientation Parameters from SLS

model	$X_L$ (m)	$Y_L$ (m)	$Z_L$ (m)	$\omega$ (Rad)	$\phi$ (Rad)	$\kappa$ (Rad)
1	0.00	0.00	0.00	0.00	0.00	0.00
2	187.38	-43.17	37.44	0.11	-0.03	0.03
3	367.67	-72.96	83.54	0.07	0.04	0.13
4	572.53	-121.83	99.97	0.03	-0.02	0.02
5	755.45	-153.31	135.70	0.07	-0.09	-0.01
6	938.85	-190.79	171.46	0.01	-0.09	-0.06
7	1111.21	-209.85	223.21	0.08	-0.10	-0.02
8	1282.81	-240.56	248.66	0.08	-0.11	0.02

Table 6.36 Exterior Orientation Parameters from KF

model	$X_L$ (m)	$Y_L$ (m)	$Z_L$ (m)	$\omega$ (Rad)	$\phi$ (Rad)	$\kappa$ (Rad)
1	0.00	0.00	0.00	0.00	0.00	0.00
2	187.38	-43.07	37.55	0.11	-0.03	0.03
3	367.63	-72.76	83.80	0.07	0.04	0.13
4	572.36	-121.60	100.19	0.03	-0.02	0.02
5	755.13	-153.05	135.87	0.07	-0.09	-0.01
6	938.56	-190.54	171.56	0.01	-0.09	-0.06
7	1110.97	-209.71	223.15	0.08	-0.10	-0.02
8	1282.61	-240.49	248.22	0.08	-0.11	0.02

Table 6.37 Exterior Orientation Parameters from CLS

model	$X_L$ (m)	$Y_L$ (m)	$Z_L$ (m)	$\omega$ (Rad)	$\phi$ (Rad)	$\kappa$ (Rad)
1	0.00	0.00	0.00	0.00	0.00	0.00
2	187.38	-43.07	37.55	0.11	-0.03	0.03
3	367.64	-72.85	83.63	0.07	0.04	0.13
4	572.47	-121.71	100.05	0.03	-0.02	0.02
5	755.36	-153.18	135.77	0.07	-0.09	-0.01
6	938.73	-190.65	171.50	0.01	-0.09	-0.06
7	1111.06	-209.71	223.23	0.08	-0.10	-0.02
8	1282.63	-240.41	248.67	0.08	-0.11	0.02

Table 6.38 Residual of Each Solution (RMS, units=pixels)

	$v_x$	$v_y$
SLS	0.09	0.43
KF	0.09	0.43
CLS	0.11	0.55

Figures 6.33-6.35 show the comparisons RMS error of X, Y, and Z coordinates of intersected points from each solution in ground space coordinate. To show the strip deformation, intersected points were transformed by seven parameter transformation using the control points from the first model. We can see that there is no significant cantilever effect for X and Y coordinate. We can see that increasing trend in Z coordinate. However, the shape of Z coordinate is direct rather than cantilever and the effect is expected to be removed by seven parameter transformation using total control points. Overall, SLS, KF, and CLS

showed no significant difference in the aerial case because numbers of strips are not enough to see the cantilever effect.

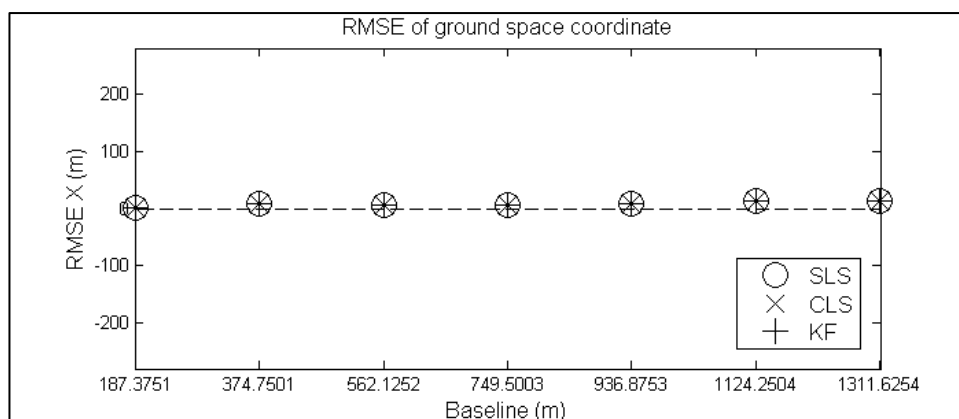


Figure 6.33 X Coordinate Comparison

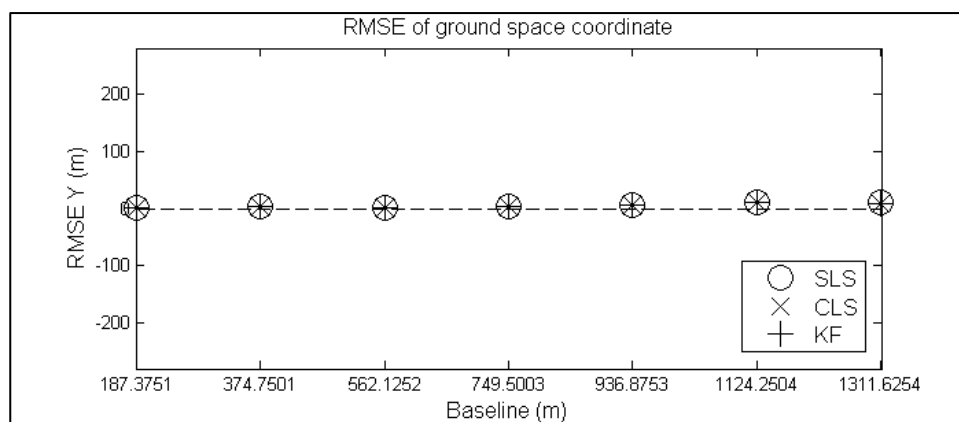


Figure 6.34 Y Coordinate Comparison

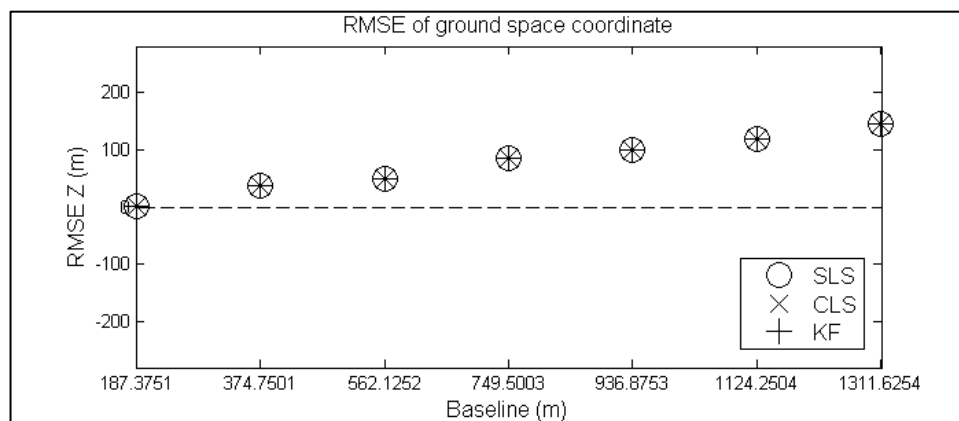


Figure 6.35 Z Coordinate Comparison

The precision of each solution was evaluated by estimating the error ellipsoid with 90% confidence level. As it can be seen in table 6.39, the KF's error ellipsoid was the smallest (factor of 0.49 to CLS in semi major axis) and it was shown that KF gave the most precise result. The SLS's error ellipsoid was the largest (factor of 3.12 to CLS in semi major axis by the reason explained in section 6.2). Figure 6.36 shows the example of error ellipsoid for one intersected point for each approach. A comparison was made between two different methods to assign values for the covariance of the dynamic model. Originally, parameter differences (equation 5.5) were used. As a comparison, this covariance was taken from *a posteriori* SLS results. A comparison of the confidence ellipsoid for an intersected point between these two methods is shown in Table 6.40, and in Figure 6.36.

Table 6.39 The Semi Major and Minor Axis of Error Ellipsoid (units=meters)

	semi major	semi minor 1	semi minor 2
SLS	43.64	21.33	13.94
CLS	13.99	1.70	0.48
KF	6.82	1.00	0.40

Table 6.41 shows the memory occupancy of each solution, and it was in descending order of SLS, KF and CLS. SLS showed far larger value than KF and CLS. The difference between CLS and KF was far smaller than KF and SLS. Therefore, we can see that KF is the very efficient approach compared to SLS.

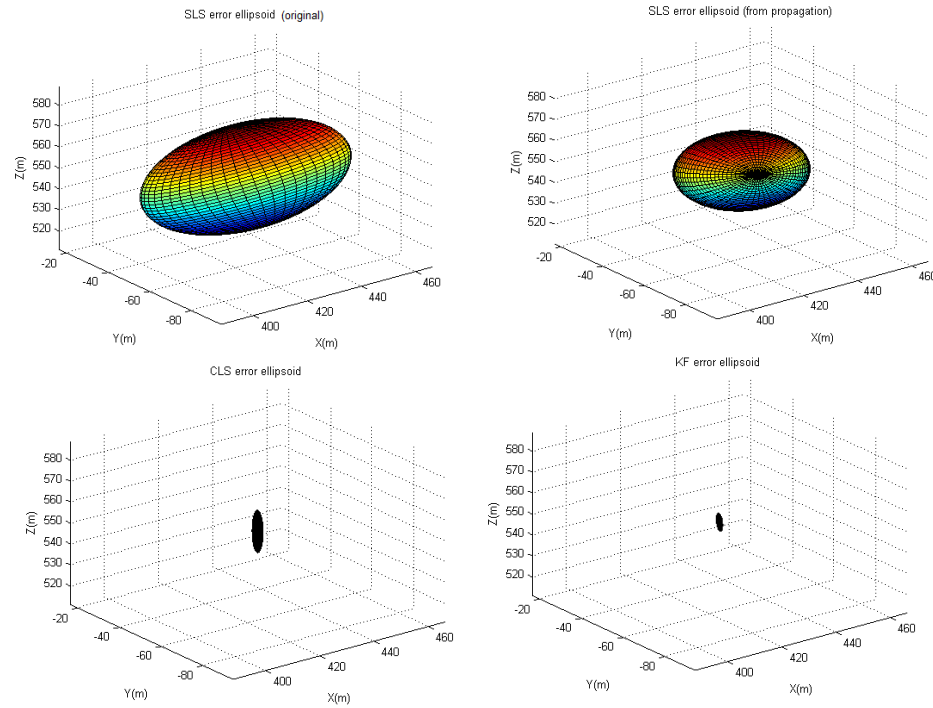


Figure 6.36 Error Ellipsoids from Each Approach (SLS w/ Apriori Covariance for White Noise: Top Left, SLS w/ Propagated Covariance for White Noise: Top Right, CLS: Bottom Left, KF: Bottom Right)

Table 6.40 Comparison of Confidence Ellipsoid for Original Selection of Dynamic Model Covariance versus Covariance from Propagation (Composite of All Points)

	semi major (m)	semi minor 1 (m)	semi minor 2 (m)
SLS original	43.64	21.33	13.94
SLS propagated	24.82	15.31	10.40

Table 6.41 Memory Occupancy of Each Solution

	CLS	SLS	KF
memory (MB)	3.58	162.06	4.43



### 6.3.2 Bundle Block Adjustment (BBA)

By using the aerial dataset in section 6.3.1, several bundle block adjustments (BBA) were implemented. The first BBA was implemented in a conventional way by applying the calibrated interior orientation parameters. The second procedure is the BBA with self calibration. The third procedure is the BBA with minimal constraints. The first two are over constrained using ground control points. The result from the third procedure will be transformed by seven parameter transformation and we will use the results from the third case as the reference for accuracy assessment for relative and absolute orientation because it is fair to compare the procedures with the same conditions. We have a total of 24 control points and we divided them into two groups with each 12 control points and used one group as control points and the other group as check points and did two experiments swapping control and check point groups. Therefore, there are a total six experiments implemented. Also, a total six of three ray pass points were used to strengthen the geometry. Additionally for BBA with minimal constraints, the corresponding points from section 6.3.1 were incorporated as pass points to give same conditions for comparison with relative orientation. Figure 6.37 and 6.38 show the configurations of control points (triangle), check points (large circle with dot), pass points (small circle) for the first and second experiment. For the BBA with minimal constraints, seven parameters were given very large weight to effectively fix them and those seven parameters were the six exterior orientation of the first image and  $X_L$  of the second image. Unified Least Squares was implemented to solve the BBA problems.

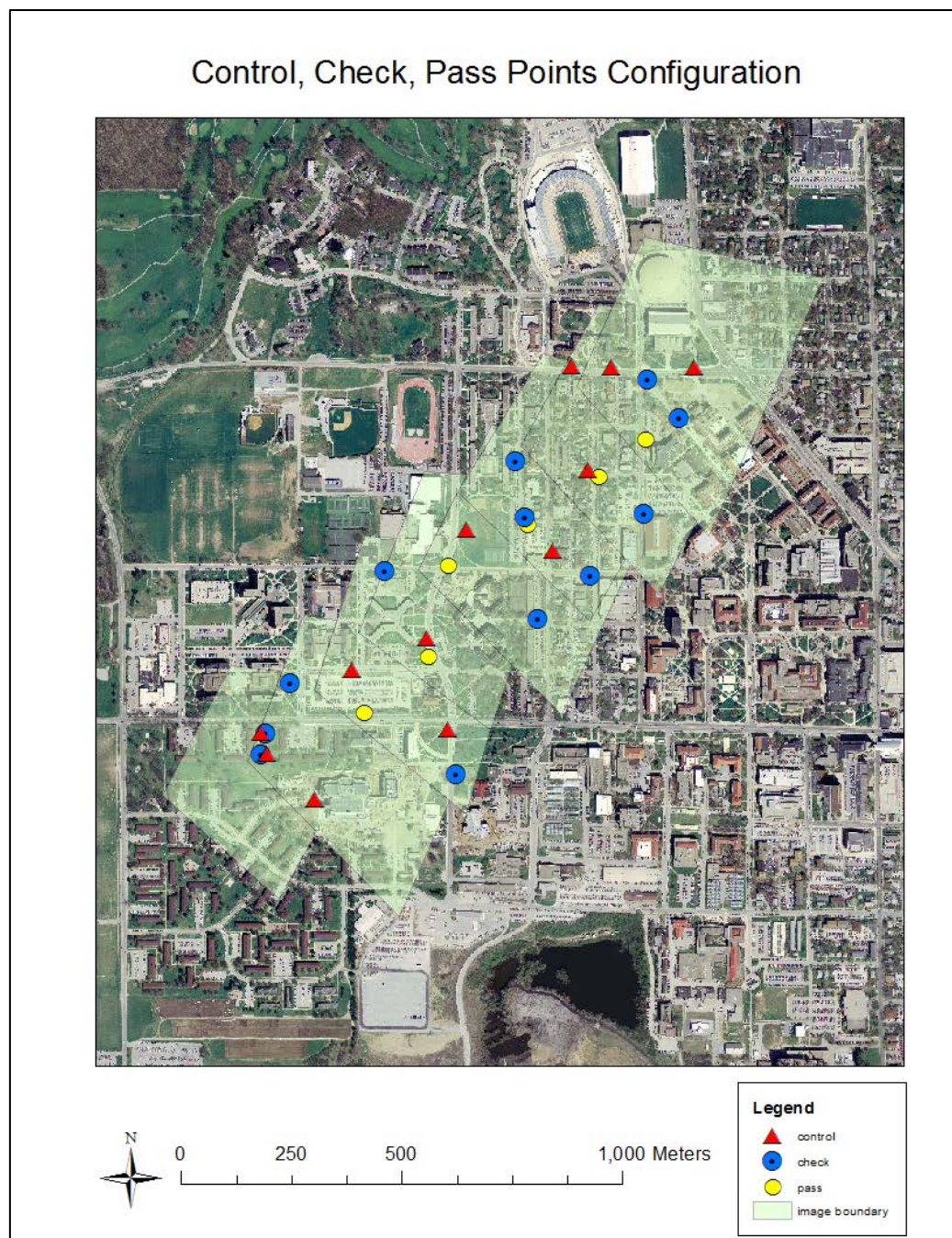


Figure 6.37 Control, Check and Pass Points Configuration (The First Group)



### Control, Check, Pass Points Configuration

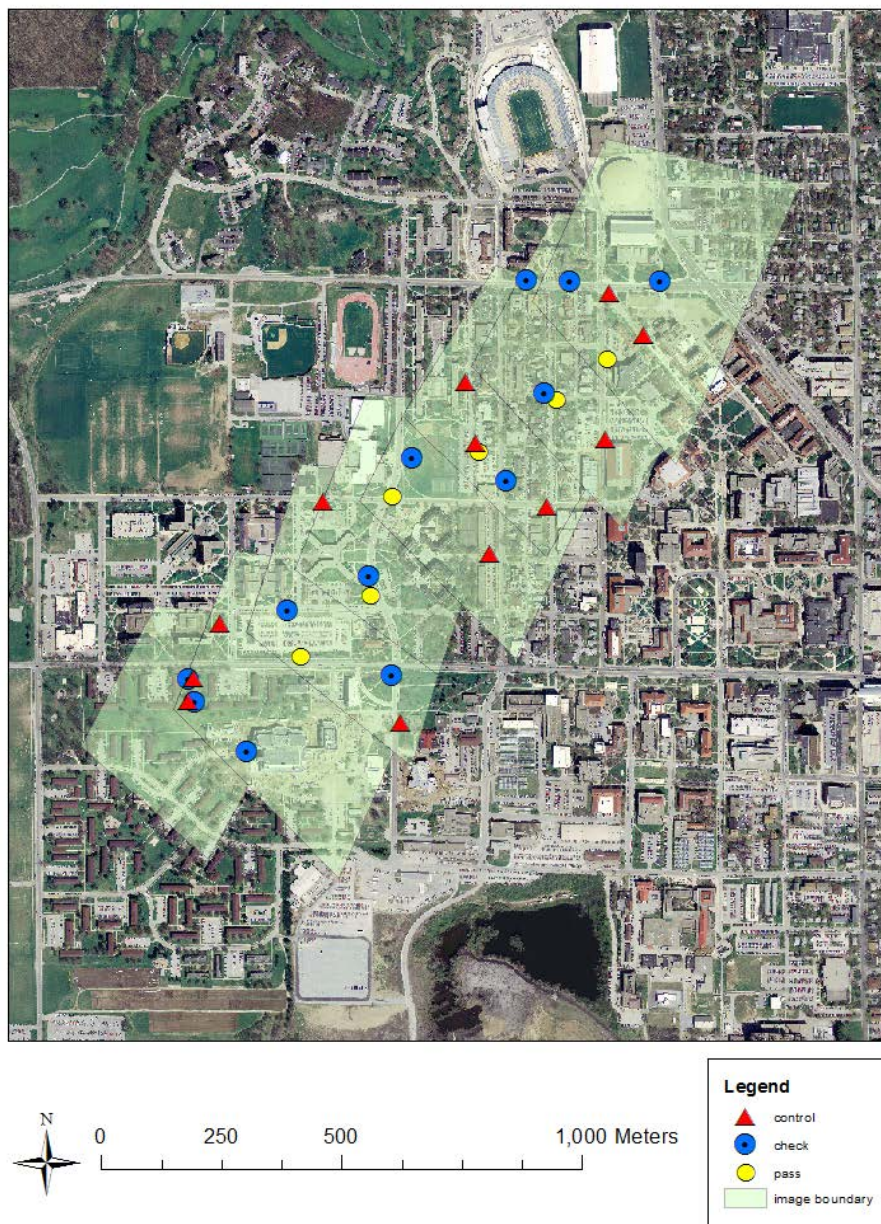


Figure 6.38 Control, Check and Pass Points Configuration (The Second Group)

Table 6.42 Exterior Orientation Parameters from Bundle Block Adjustment

Image no	$X_L(m)$	$Y_L(m)$	$Z_L(m)$	$\omega$ (radian)	$\phi$ (radian)	$\kappa$ (radian)
Bundle Block Adjustment (Group 1)						
1	505862.01	4474930.74	531.71	-0.41	-0.66	4.07
2	506001.52	4475069.70	536.08	-0.52	-0.75	4.03
3	506145.38	4475220.98	535.00	-0.43	-0.74	4.19
4	506270.11	4475362.86	533.92	-0.44	-0.73	4.07
5	506396.25	4475511.32	539.51	-0.55	-0.71	3.98
6	506526.42	4475648.69	547.72	-0.49	-0.67	3.97
7	506645.87	4475785.58	545.75	-0.54	-0.71	3.97
8	506761.17	4475929.23	550.08	-0.56	-0.71	3.99
Bundle Block Adjustment with Self Calibration (Group 1)						
1	505853.40	4474942.03	543.60	-0.38	-0.75	4.10
2	505984.49	4475080.00	546.04	-0.49	-0.85	4.05
3	506125.44	4475222.83	542.56	-0.36	-0.84	4.24
4	506256.78	4475371.87	546.17	-0.39	-0.83	4.11
5	506379.17	4475524.00	544.58	-0.53	-0.82	4.00
6	506512.85	4475650.45	561.30	-0.45	-0.77	4.00
7	506630.43	4475798.48	555.51	-0.52	-0.81	3.98
8	506739.83	4475935.48	548.72	-0.54	-0.83	4.01
Bundle Block Adjustment with Minimal Constraints (Group 1)						
1	505863.22	4474931.80	530.12	-0.41	-0.66	4.06
2	506001.32	4475067.39	536.51	-0.53	-0.74	4.02

Table 6.42 Continued.

3	506136.53	4475204.23	527.19	-0.44	-0.74	4.19
4	506273.57	4475359.62	547.93	-0.46	-0.68	4.05
5	506404.09	4475500.28	546.44	-0.56	-0.66	3.97
6	506539.14	4475639.31	550.46	-0.51	-0.61	3.95
7	506666.21	4475769.35	531.36	-0.58	-0.66	3.94
8	506785.93	4475904.97	537.40	-0.59	-0.65	3.97
Bundle Block Adjustment (Group 2)						
1	505859.91	4474927.81	531.79	-0.40	-0.66	4.07
2	506000.73	4475067.38	534.10	-0.52	-0.75	4.03
3	506138.75	4475214.96	537.04	-0.42	-0.74	4.20
4	506273.94	4475368.29	542.09	-0.44	-0.72	4.07
5	506398.08	4475512.43	541.69	-0.54	-0.71	3.98
6	506523.51	4475650.25	547.40	-0.49	-0.67	3.97
7	506643.87	4475789.41	538.74	-0.56	-0.72	3.96
8	506763.67	4475931.72	550.58	-0.57	-0.71	3.99
Bundle Block Adjustment with Self Calibration (Group 2)						
1	505856.73	4474942.31	550.74	-0.45	-0.68	4.05
2	505987.37	4475074.55	546.56	-0.55	-0.78	4.00
3	506132.31	4475226.32	541.69	-0.46	-0.78	4.17
4	506260.93	4475372.36	552.04	-0.47	-0.76	4.05
5	506387.48	4475521.29	551.69	-0.58	-0.74	3.95
6	506512.52	4475655.46	559.99	-0.52	-0.70	3.95

Table 6.42 Continued.

7	506629.96	4475795.13	549.67	-0.59	-0.75	3.93
8	506744.22	4475938.27	579.90	-0.58	-0.74	3.98
Bundle Block Adjustment with Minimal Constraints(Group 2)						
1	505863.22	4474931.80	530.12	-0.41	-0.66	4.06
2	506001.32	4475068.49	541.46	-0.53	-0.72	4.01
3	506134.46	4475201.18	531.64	-0.44	-0.73	4.18
4	506265.39	4475346.41	540.44	-0.46	-0.69	4.05
5	506390.32	4475481.47	539.33	-0.56	-0.67	3.96
6	506518.15	4475613.26	542.66	-0.52	-0.62	3.95
7	506641.42	4475739.21	522.18	-0.59	-0.66	3.94
8	506754.64	4475866.72	527.69	-0.60	-0.66	3.97

Table 6.42 shows the exterior orientation parameters estimated by each BBA variation and Table 6.43 shows the RMS in image space of residuals in both x and y directions. In every case, the total RMS of residuals was less than one pixel. The camera parameters estimated from BBA with self calibration were already shown in table 6.19 in section 6.1.

As mentioned before, the control points estimated from BBA with minimal constraints were transformed by a seven parameter (rigid body) transformation and table 6.44 shows the results of seven parameter transformation.

Table 6.43 The RMS of Residuals (units=pixels)

	X	Y	total
BBA (1 <sup>st</sup> group)	0.82	0.83	0.83
BBA /w self calibration (1 <sup>st</sup> group)	0.43	0.48	0.45
BBA /w minimal constraints (1 <sup>st</sup> group)	0.16	0.97	0.69
BBA (2 <sup>nd</sup> group)	0.67	1.13	0.93
BBA /w self calibration (2 <sup>nd</sup> group)	0.36	0.82	0.63
BBA /w minimal constraints (2 <sup>nd</sup> group)	0.30	1.02	0.75

Table 6.44 Seven Parameter Values for Transformation to the Control Points from BBA w/ Minimal Constraints

Parameter	1 <sup>st</sup> group	2 <sup>nd</sup> group
$\omega$ (radian)	-0.02	-0.02
$\phi$ (radian)	0.02	0.01
$\kappa$ (radian)	-0.03	-0.02
Scale	1.02	1.07
$T_x$ (m)	144417.36	86746.38
$T_y$ (m)	-112397.28	-305449.82
$T_z$ (m)	-82935.96	-82107.61

Table 6.45 shows the misclosures at check points. As we expected, BBA with pre-calibrated camera parameters gave the best results because the calibration parameters were rigorously estimated. However, the result from the BBA with minimal constraints and seven-parameter transformation were chosen as the accuracy reference since the condition of the procedure is equivalent to the relative and absolute orientation procedure. BBA with self calibration showed far larger misclosure compared to the other two procedures because of poor geometry as explained earlier (sec. 6. 1. 2).

Table 6.45 Misclosures of Check Points (units=meters)

	RMS X	RMS Y	RMS Z	total RMS
BBA (1 <sup>st</sup> group)	1.70	1.07	1.72	1.53
BBA /w self calibration (1 <sup>st</sup> group)	42.26	20.05	33.90	33.35
BBA /w minimal constraints (1 <sup>st</sup> group)	3.42	3.88	3.37	3.56
BBA (2 <sup>nd</sup> group)	1.43	0.93	1.39	1.27
BBA /w self calibration (2 <sup>nd</sup> group)	19.22	10.39	16.78	15.91
BBA /w minimal constraints (2 <sup>nd</sup> group)	3.28	2.67	4.15	3.42
BBA (total)	1.57	1.00	1.56	1.40
BBA /w self calibration (total)	30.74	15.22	25.34	24.63
BBA /w minimal constraints (total)	3.35	3.28	3.76	3.49



Table 6.46 The Length of Semi Major Axis of Error Ellipsoid at Pass Points  
(units=meters)

Model no	BBA	BBA /w self calibration
1 <sup>st</sup> group		
1	2.72	4.55
2	1.86	2.74
3	2.50	2.73
4	2.16	2.49
5	1.97	2.05
6	5.86	8.74
mean	2.84	3.88
2 <sup>nd</sup> group		
1	4.53	7.54
2	2.45	2.86
3	2.67	4.28
4	1.68	1.77
5	3.22	3.51
6	4.60	5.82
mean	3.19	4.30

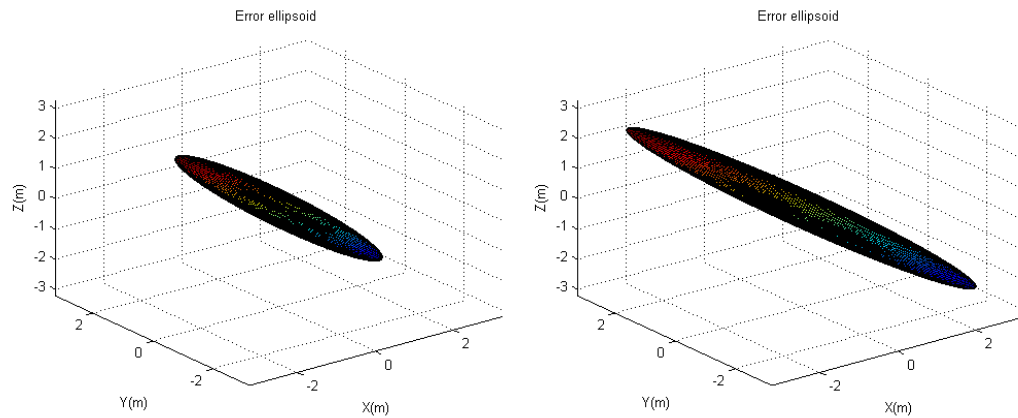


Figure 6.39 Error Ellipsoid for Pass Point2 from Group 1  
(Left; BBA, Right: BBA with Self Calibration)

Figure 6.39 show the examples of error ellipsoid of 90% confidence and table 6.46 shows the length of semi major axis at pass points. The mean of semi major axis lengths of error ellipsoid for BBA is 3.19 meter and BBA with self calibration is 4.30 meter which suggests the higher precision of pre-calibration with strong geometry than *in situ* calibration with poor geometry.

To verify the reliability of the suggested BBA approach with Unified Least Square, another BBA (JSK) was implemented and compared with the BBA results from commercial software iWitness (Photometrix, 2010). Principal point offset ( $x_0, y_0$ ), focal length ( $f$ ) and the coefficients of radial distortions ( $K_1, K_2, K_3$ ) were carried as interior orientation parameters. In BBA (JSK), the image space coordinates, the object space coordinates and the associated standard

deviations of 18 points were adopted from iWitness. Figure 6.40 shows the images used for the BBA comparison with iWitness.

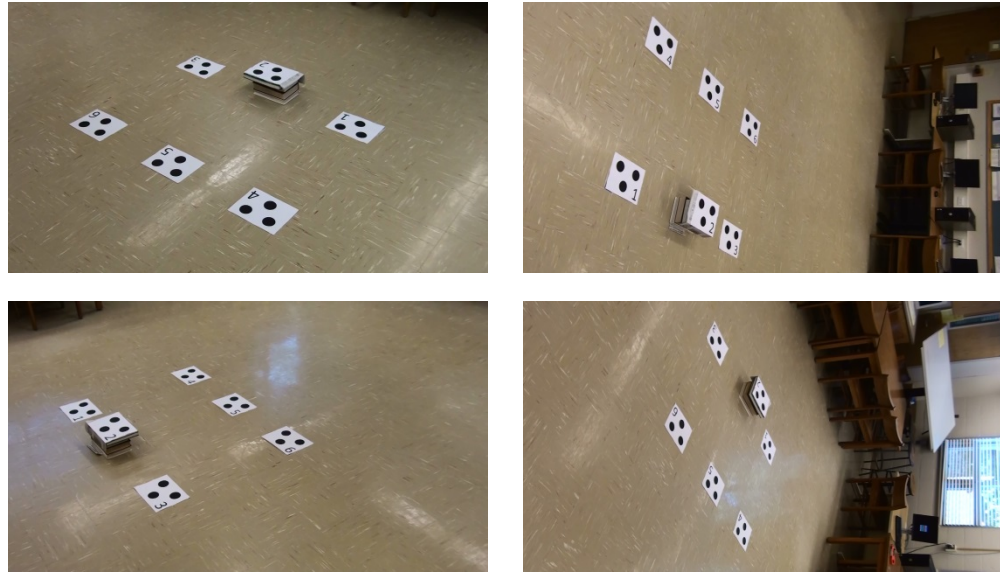


Figure 6.40 The Data for the Comparison of BBA with iWitness

Table 6.47 and table 6.48 show the comparisons of interior and exterior orientation parameters. It was found out that the suggested BBA approach (JSK) gave similar result to iWitness. Therefore, the BBA implemented in this research is found out to be reliable.

Table 6.47 The Comparison of Interior Orientation Parameters

	$x_0(\text{mm})$	$y_0(\text{mm})$	$f(\text{mm})$	$K_1$	$K_2$	$K_3$
JSK	-0.0170	0.0249	3.7179	-0.0091	0.0026	-0.0014
iWitness	-0.0176	0.0250	3.7051	-0.0093	0.0025	-0.0009

Table 6.48 The Comparison of Exterior Orientation Parameters

Image	approach	$X_L(m)$	$Y_L(m)$	$Z_L(m)$	$\omega(\text{radian})$	$\phi(\text{radian})$	$\kappa(\text{radian})$
1	JSK	0.00	0.00	0.00	1.57	0.00	0.00
	iWitness	0.00	0.00	0.00	1.57	0.00	0.00
2	JSK	2.97	1.49	1.42	0.95	1.05	2.68
	iWitness	2.95	1.48	1.40	0.96	1.04	2.68
3	JSK	-1.53	4.62	3.30	-0.39	-0.27	-3.02
	iWitness	-1.53	4.61	3.28	-0.39	-0.27	-3.02
4	JSK	-4.04	1.79	1.46	0.86	-1.14	0.21
	iWitness	-4.02	1.81	1.45	0.86	-1.14	0.21

### 6.3.3 Absolute Orientation for SLS, KF, and CLS

Since the relative orientation (RO) gives the results only in relative sense, we need to transform those results into the real world coordinate system by the procedure described in chapter 4.6. Two kinds of absolute orientation (AO) were implemented – the first was the seven parameter (rigid body=conformal) transformation and the second was a non-conformal polynomial transformation. We used exterior orientation parameters from SLS, KF and CLS. The AO was implemented for two control points groups as in section 6.3.2 and the misclosures at the check points were estimated to compare with those from BBA with minimal constraints. Table 6.49 shows the results of the parameter values. Table 6.50 shows the misclosures at check points in each of the six cases. The overall accuracies from SLS, KF and CLS were similar because of small number of images in the strip. Misclosure (4.2m) from RO was quite similar to that from

BBA with minimal constraints (3.5m). The difference of misclosures between the first and the second groups was quite small, which suggest that the comparisons of misclosures at check points are reliable.

Table 6.49 The Seven Parameters Estimated by Absolute Orientation

Parameter	SLS	KF	CLS
The first group			
$\omega$ (radian)	-0.80	-0.80	-0.80
$\varphi$ (radian)	-0.03	-0.03	-0.03
$\kappa$ (radian)	-1.10	-1.10	-1.10
Scale	1.03	1.03	1.03
$T_x$ (m)	505851.55	505851.52	505851.50
$T_y$ (m)	4474921.13	4474920.84	4474921.20
$T_z$ (m)	-186.65	-186.71	-186.89
The second group			
$\omega$ (radian)	-0.78	-0.78	-0.78
$\varphi$ (radian)	-0.04	-0.04	-0.04
$\kappa$ (radian)	-1.09	-1.10	-1.10
Scale	1.03	1.03	1.03
$T_x$ (m)	505852.50	505852.52	505852.45
$T_y$ (m)	4474921.35	4474920.83	4474921.37
$T_z$ (m)	-200.22	-200.43	-200.43

Table 6.50 Misclosures at Check Points for Seven Parameter Transformation

(units=meters)

	RMSE_X	RMSE_Y	RMSE_Z	RMSE
Experiment 1				
SLS	3.74	2.49	6.09	4.37
KF	3.74	2.43	6.04	4.34
CLS	3.73	2.48	6.07	4.36
Experiment 2				
SLS	4.29	3.17	4.75	4.12
KF	4.37	3.16	4.74	4.14
CLS	4.30	3.16	4.74	4.12
total				
SLS	4.02	2.85	5.46	4.25
KF	4.07	2.82	5.43	4.24
CLS	4.03	2.84	5.45	4.24

Table 6.51 shows the result of polynomial transformation by the Schut method and table 6.52 shows the RMS of misclosures at check points from Polynomial transformation. The order of the polynomial ( $x'$ ,  $y'$ ,  $z'$  as function of  $x, y$ ) was 4. In retrospect, this was too large for the length of the strip. Over

parameterizing polynomials is a common misstep and will account for the poor results at check points.

Table 6.51 The Polynomial Parameters Estimated by Absolute Orientation

Parameter	SLS	KF	CLS
The first experiment			
a1	506194.92	506194.91	506194.90
a2	4474764.69	4474764.67	4474764.68
a3	-0.34	-0.34	-0.34
a4	0.85	0.85	0.85
a5	0.00	0.00	0.00
a6	0.00	0.00	0.00
a7	0.00	0.00	0.00
a8	0.00	0.00	0.00
b0	-344.80	-344.90	-344.95
b1	0.30	0.30	0.30
b2	-0.06	-0.06	-0.06
c1	0.00	0.00	0.00
c2	0.00	0.00	0.00
c3	0.00	0.00	0.00

Table 6.51 Continued.

d1	0.00	0.00	0.00
d2	0.00	0.00	0.00
d3	0.00	0.00	0.00
d4	0.00	0.00	0.00
e1	0.00	0.00	0.00
e2	0.00	0.00	0.00
The second experiment			
a1	506174.20	506174.19	506174.18
a2	4474767.66	4474767.65	4474767.65
a3	-0.27	-0.27	-0.27
a4	0.79	0.79	0.79
a5	0.00	0.00	0.00
a6	0.00	0.00	0.00
a7	0.00	0.00	0.00
a8	0.00	0.00	0.00
b0	-297.70	-298.54	-297.91
b1	0.72	0.71	0.72
b2	0.38	0.38	0.38
c1	0.00	0.00	0.00



Table 6.51 Continued.

c2	0.00	0.00	0.00
c3	0.00	0.00	0.00
d1	0.00	0.00	0.00
d2	0.00	0.00	0.00
d3	0.00	0.00	0.00
d4	0.00	0.00	0.00
e1	0.00	0.00	0.00
e2	0.00	0.00	0.00

In table 6.52, the RMS of misclosures from the polynomial transformation with KF was more than five times of those from the seven parameter transformation. The polynomial transformation gave an inaccurate result in this case and polynomial transformations can be dangerous sometimes. Therefore, the polynomial transformation will not be considered any further. Also, it is suggested that the result of polynomial transformation should be compared to the seven parameter rigid body transformation (effectively a first order polynomial) before using it, if control and check points are available.

Table 6.52 Misclosures at Check Points for Schut Polynomial Transformation  
(units=meters)

	RMSE_X	RMSE_Y	RMSE_Z	RMSE
Experiment 1				
SLS	35.79	7.40	21.84	24.58
KF	35.76	7.38	21.64	24.51
CLS	35.77	7.39	21.81	24.56
Experiment 2				
SLS	26.33	21.62	22.25	23.49
KF	26.30	21.61	21.60	23.28
CLS	26.32	21.61	22.22	23.48
total				
SLS	31.42	16.16	22.05	24.04
KF	31.39	16.15	21.62	23.90
CLS	31.40	16.15	22.02	24.03

Table 6.53 shows the comparison of RMS of misclosures between ARO/AO and BBA/MC/AO. The RMS of misclosures of BBA/MC/AO and ARO/AO with KF were each 3.49 and 4.24 meters respectively. BBA was expected to give the best result. As mentioned before, it is hard to see the differences of misclosures between each approach because of the small number of images and models.

Since it was impractical to acquire more aerial imagery, it was decided that simulation with a larger number of frames would be implemented to better examine the cantilever effect of CLS and how it is alleviated by SLS and KF. Also note that BBA, being a simultaneous solution, requires memory resources on the order of SLS.

Table 6.53 The Comparison of Misclosures for Each Method (units=meters), (AO=absolute orientation, MC=minimal constraints)

	ARO with AO	BBA / MC with AO
SLS	4.25	3.49
KF	4.24	
CLS	4.24	

#### 6.4 APPLICATION 4: Automated Relative Orientation – Simulation

Since there was no significant difference in misclosures in the aerial case between SLS, KF, and CLS (because of the small number of images), simulation with a larger number of images was implemented. In this experiment, relative orientation, absolute orientation, and bundle block adjustment with minimal constraints and AO/7P (absolute orientation by seven parameters) were implemented. The results were assessed with the misclosures at check points. The simulations were done with nominal flight and exposure parameters,

perturbed by random (pseudo random) values from a random number generator (RNG). In order to not be reliant on a single set of random numbers, the simulations were done five times. Each time, the targeted nominal values were perturbed by a zero mean normal random number with given standard deviation ( $\sigma$ ).

#### 6.4.1 Relative Orientation

For simulation, the data was generated as described in table 6.54. Figure 6.41 shows the location of each point and figure 6.42 shows a magnified view for the example of simulation. For simulation, random perturbations for each exterior orientation element, image coordinates and interior orientation parameters were added to the nominal values for camera parameters, image points, pass, scale restraint, control and check points as shown in table 6.55. As in section 6.3, there were two control point groups swapped between control and check point function. In this experiment, we wanted to investigate the effect of different adjustment/estimation methods, in cases where there was a significant cantilever effect. In order to produce such a significant cantilever effect, we re-introduced unmodeled, uncorrected systematic errors. In practice, of course, one would do everything possible to correct/compensate such errors by calibration. In this case we wanted to investigate the performance of strips with cantilever effects, so the internal camera parameters were purposely perturbed. Sigmas for these values are shown in table 6.55.

Table 6.54 The Nominal Parameters for Simulation

no of imageries	Overlap Ratio	base height ratio	baseline	no pass point /image	No. scale restraint point /model	no control points /image	no check points /image
30	0.6	0.6	1000m	20	1	4	4

Table 6.55 The Random Perturbations Added to Nominal Values (Sigmas for RNG)

$X_L, Y_L, Z_L$	$\omega, \varphi, \kappa$	Control and check point	image coordinate	$x_0, y_0, K_1, K_2, K_3, P_1, P_2$
3m	$0.1^\circ$ (equivalent 3m)	1m	1 pixel	equivalent to 10 pixel

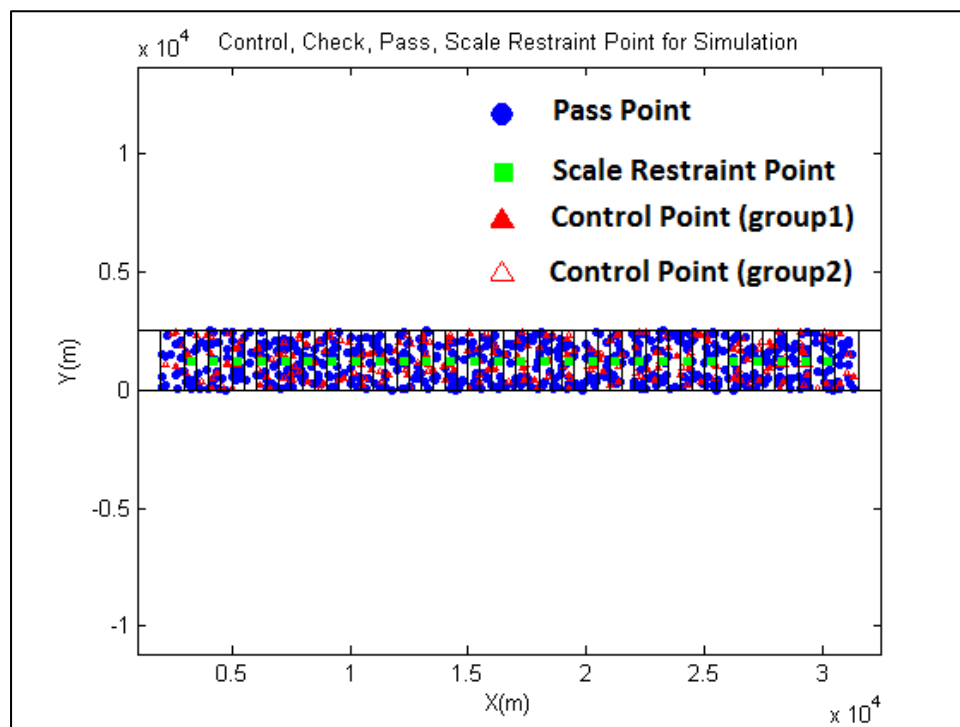


Figure 6.41 Pass, Scale Restraint, Control and Check Points for Simulation

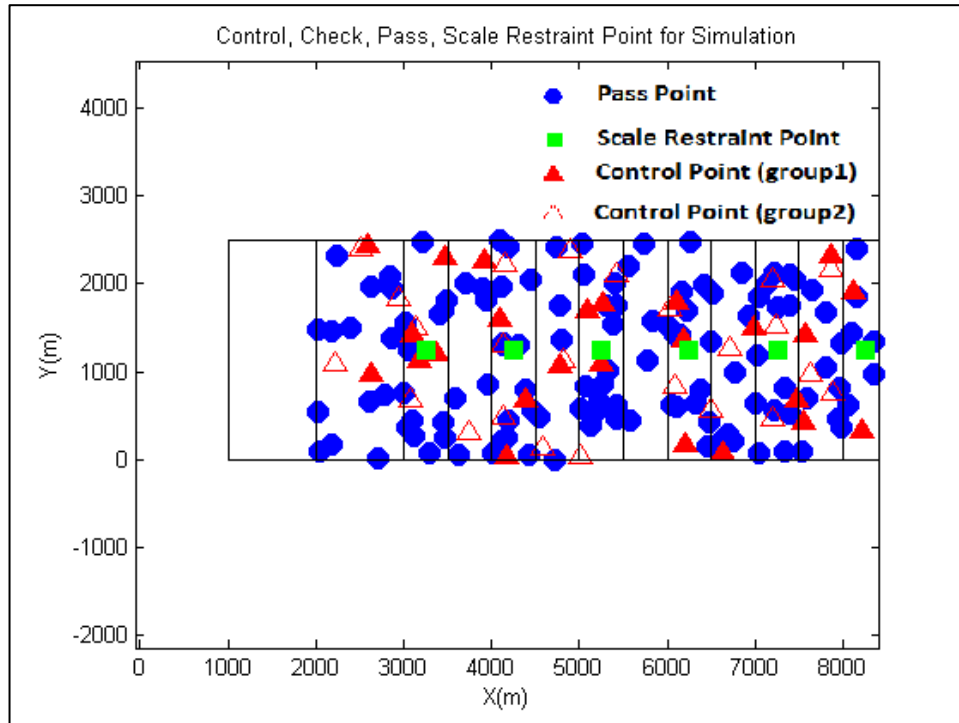


Figure 6.42 Pass, Scale Restraint, Control and Check Points for Simulation (magnified  $\times 5$ )

In order to visualize the extent of the cantilever effect in strip formation, the following steps were done. The strip formation was done by each of the three methods under investigation: SLS, KF and CLS. Then a limited absolute orientation was done by a transformation based only on control points in the first model. That is, it is fixed only one end, and as expected, large cantilever deformation appears as one moves down the strip. These deformations are tabulated as RMS errors within each model. Then these RMS errors, per model, are plotted as a function of portion along the strip. They are plotted twice, once with planimetric aspect ratio to exaggerate the effect, and once with 1:1 aspect ratio (to see the true shape of the cantilever deformation). These plots, figures

6.44 to 6.53, are shown for each of the five simulations. However, prior to doing this, a preliminary test was done, which resulted in modifying the KF algorithm. Using data from simulation 5, the first plot in Figure 6.43 was generated. The KF algorithm took white noise covariance from equation 5.5, and had no prior knowledge about the parameters in the last model. As a test the KF algorithm was modified in two ways: (1) The covariance of white noise was taken from SLS results, (equation 5.12), and (2) the end parameters of the SLS estimation ( $b_x$ ,  $b_y$ ,  $b_z$ ,  $\omega$ ,  $\phi$ ,  $\kappa$ ) were taken as fixed in the KF algorithm. There are relative parameters, not absolute positions and attitudes. But it had the effect of moving the KF solution closer to the SLS solution. This is shown in the second plot of figure 6.43. If one actually did this in practice, then one would lose the benefit of the small memory profile of the KF algorithm. Alternatively, the same information could be provided indirectly by ground control points in the last model or by auxiliary sensors (GPS for position and interior for attitude). Therefore, the comparisons between SLS, KF, and CLS are preordained to show better agreement between SLS and KF, and to show poorer agreement between these and CLS.

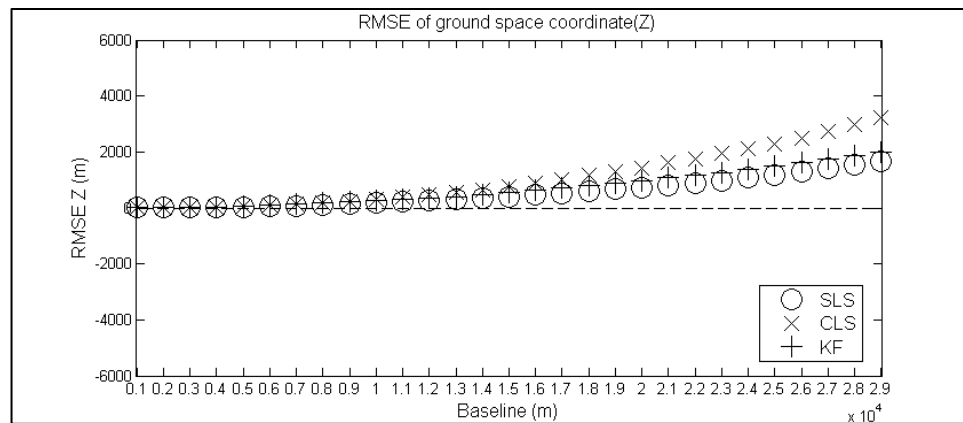
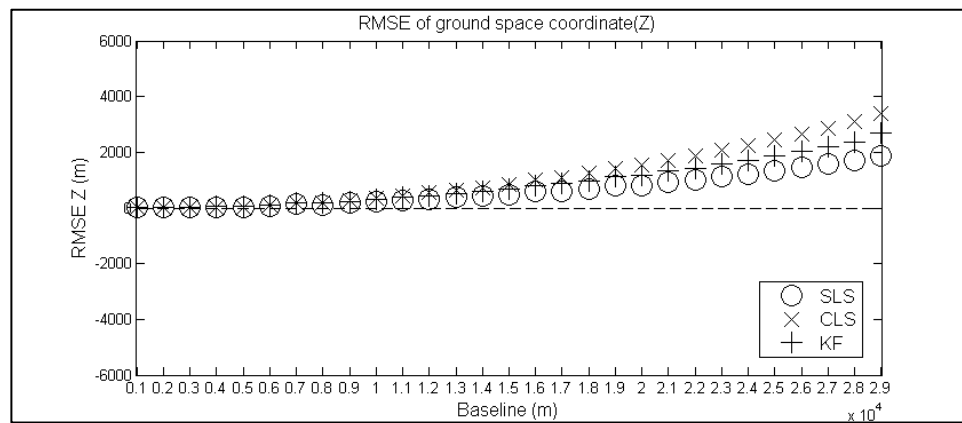


Figure 6.43 Strip Deformation in Z direction  
 (Top: *A Priori* Covariance with Unfixed End Parameters,  
 Bottom: Propagated Covariance with Fixed End Parameters from SLS)



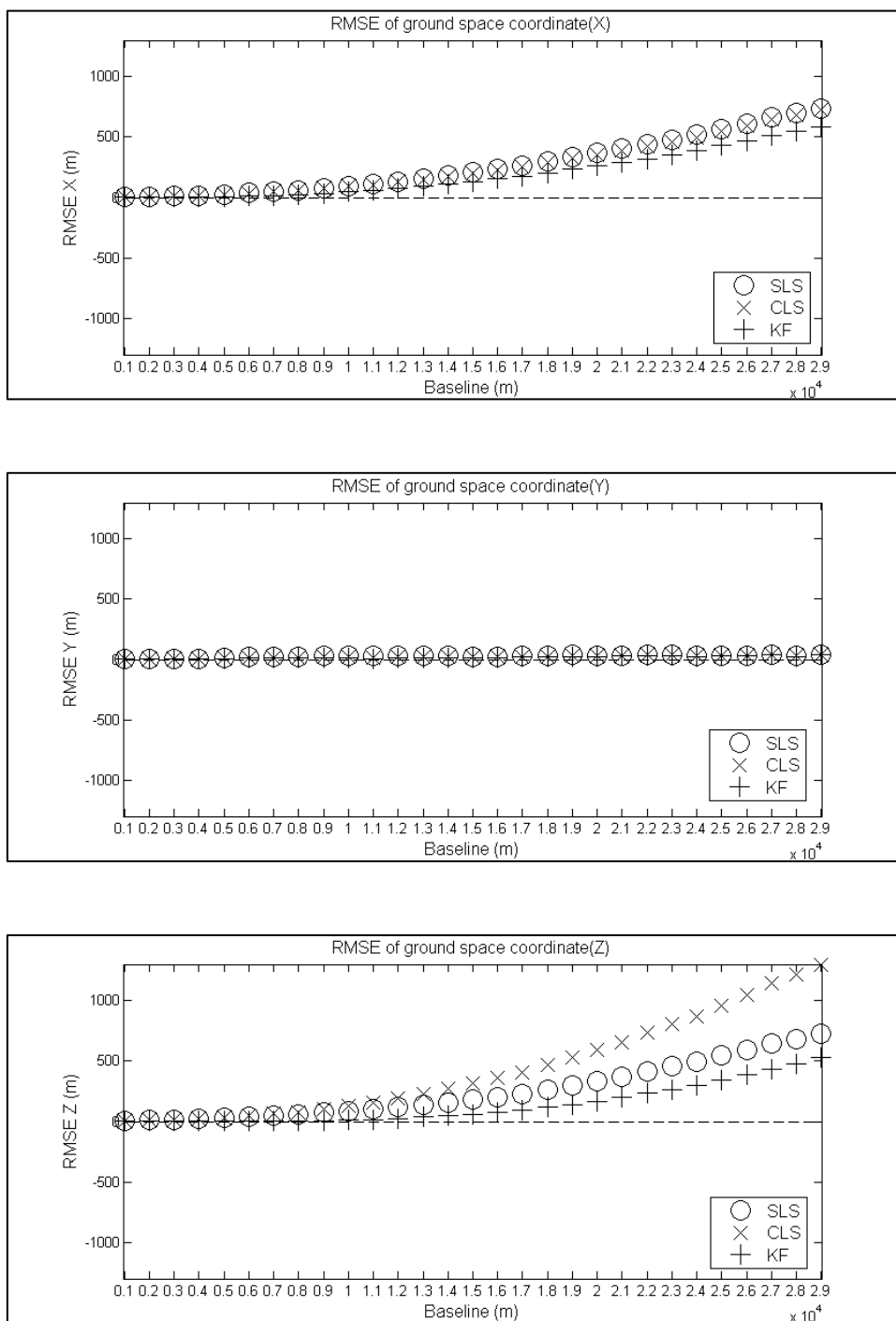


Figure 6.44 Strip Deformation Comparison, Simulation 1, y axis is exaggerated by  $\times 4.62$  (Top: X, Center: Y, Bottom: Z)

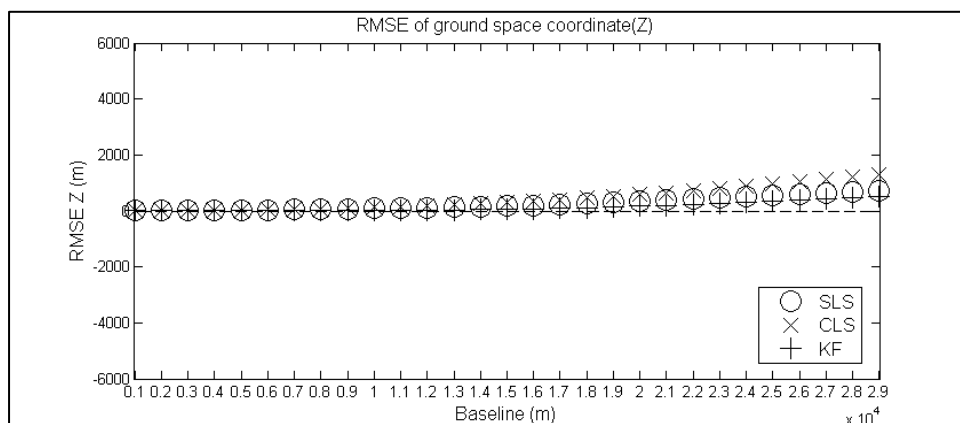
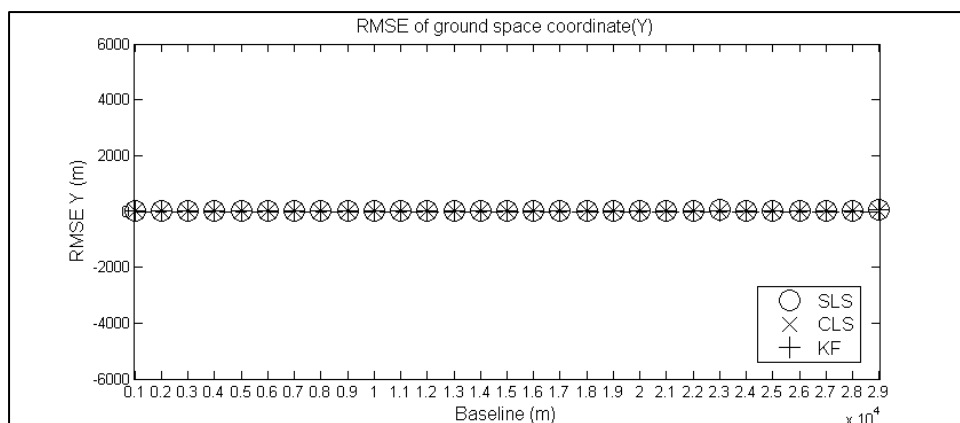
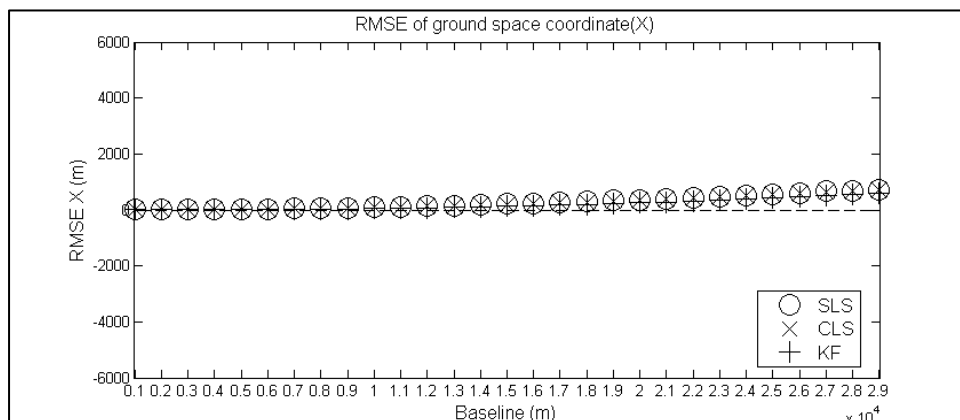


Figure 6.45 Strip Deformation Comparison, Simulation 1, Real Aspect Ratio (Top: X, Center: Y, Bottom: Z)

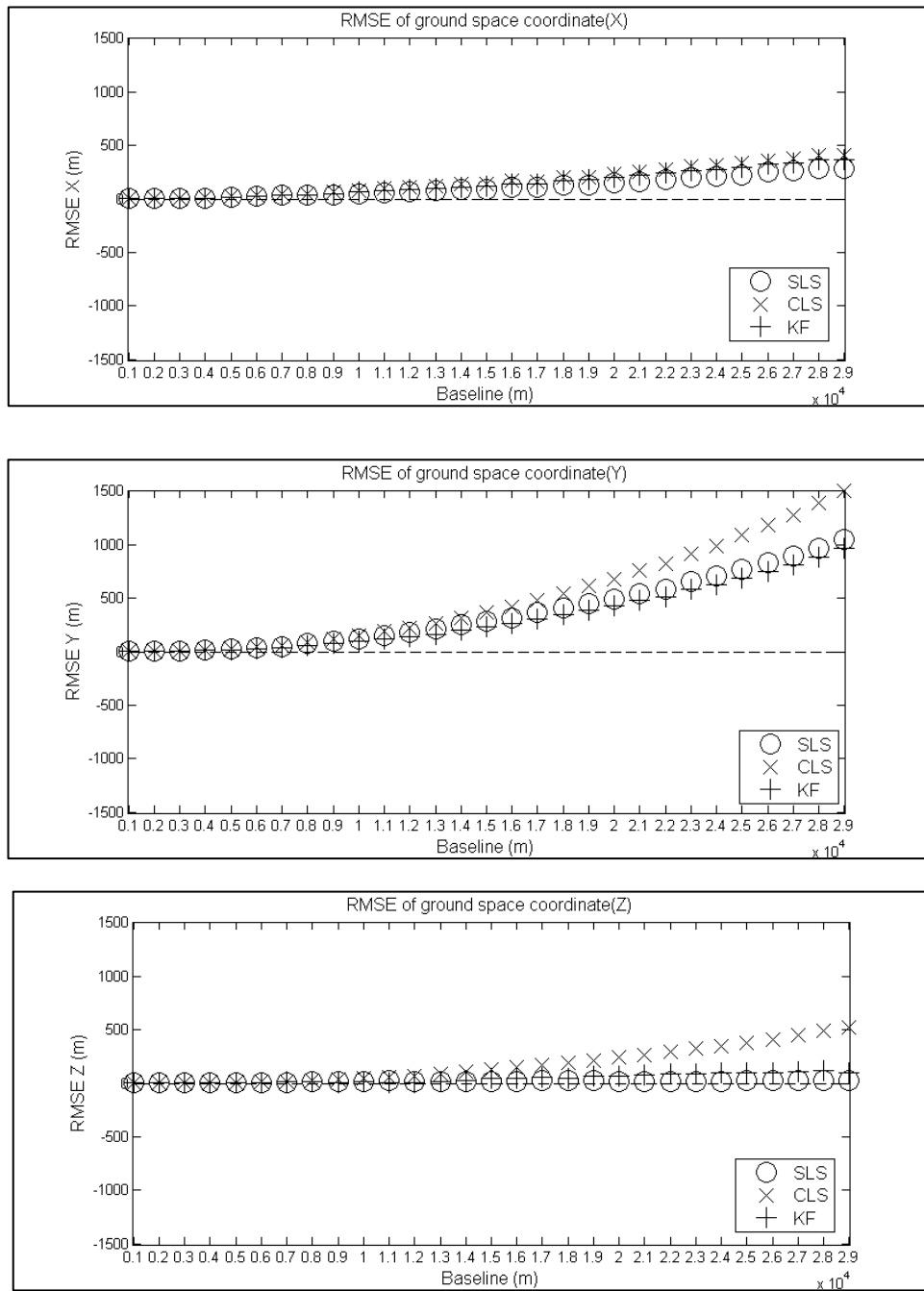


Figure 6.46 Strip Deformation Comparison, Simulation 2, y axis is exaggerated by  $\times 3.97$  (Top: X, Center: Y, Bottom: Z)

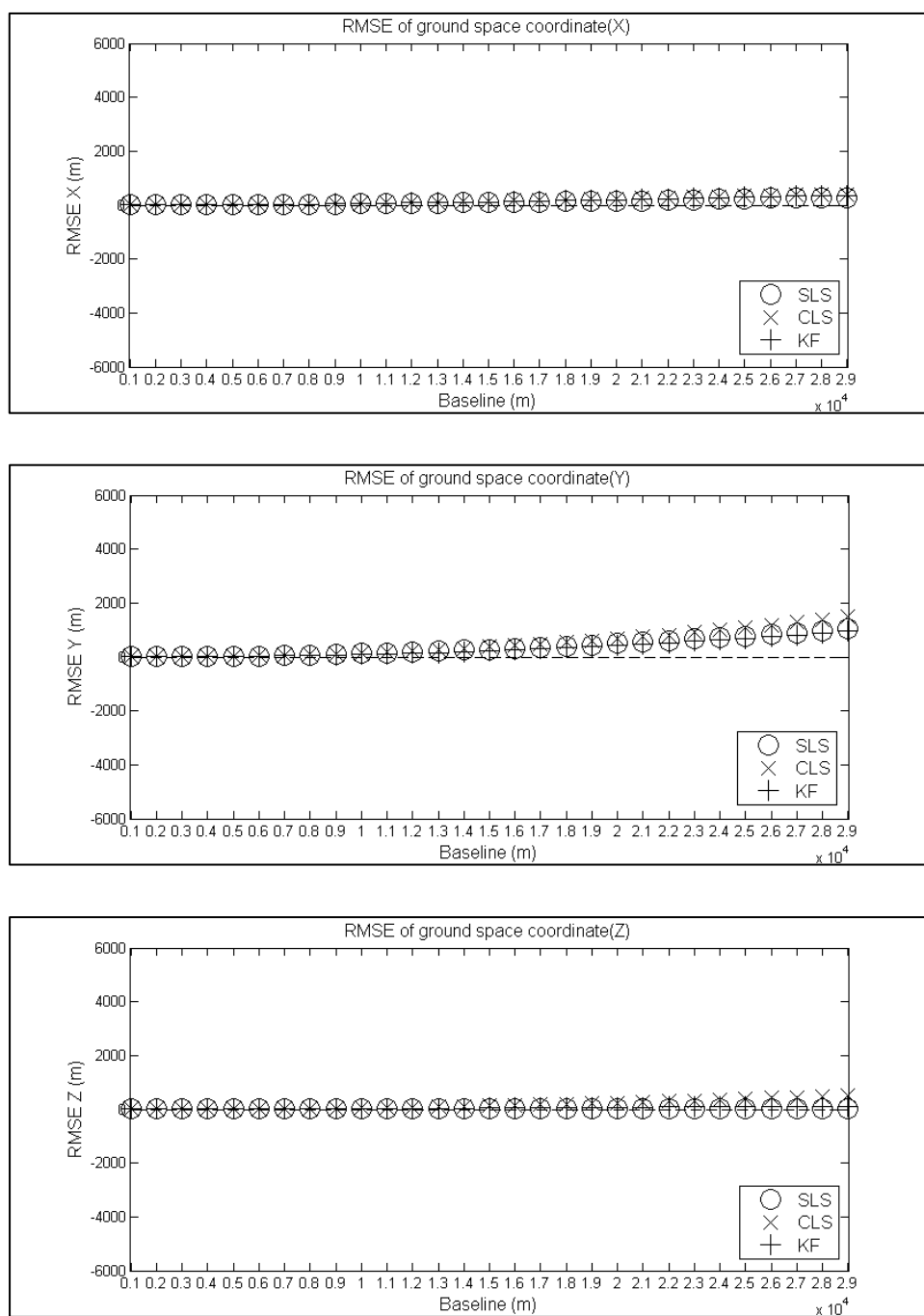


Figure 6.47 Strip Deformation Comparison, Simulation 2, Real Aspect Ratio (Top: X, Center: Y, Bottom: Z)

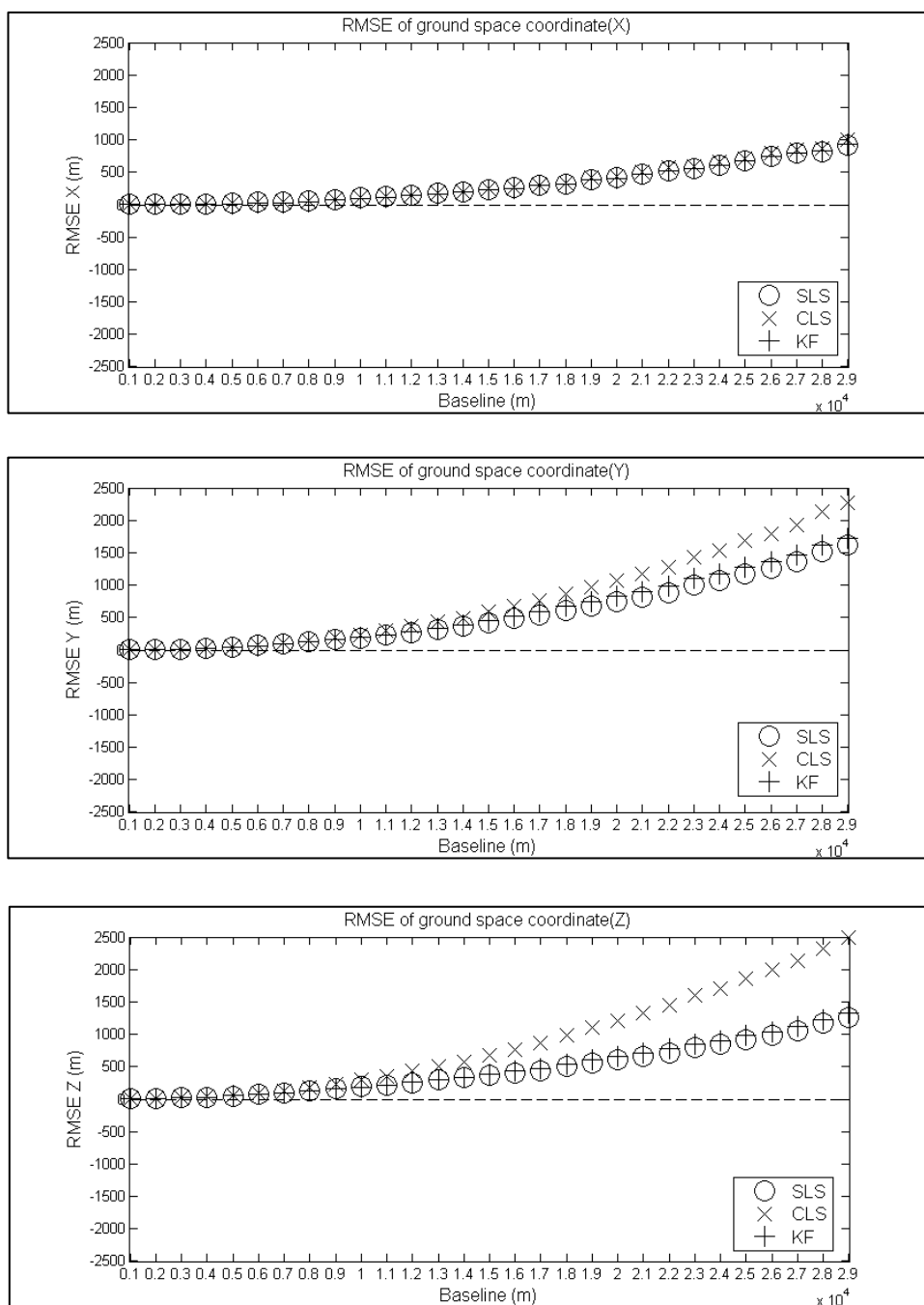


Figure 6.48 Strip Deformation Comparison, Simulation 3, y axis is exaggerated by  $\times 2.39$  (Top: X, Center: Y, Bottom: Z)

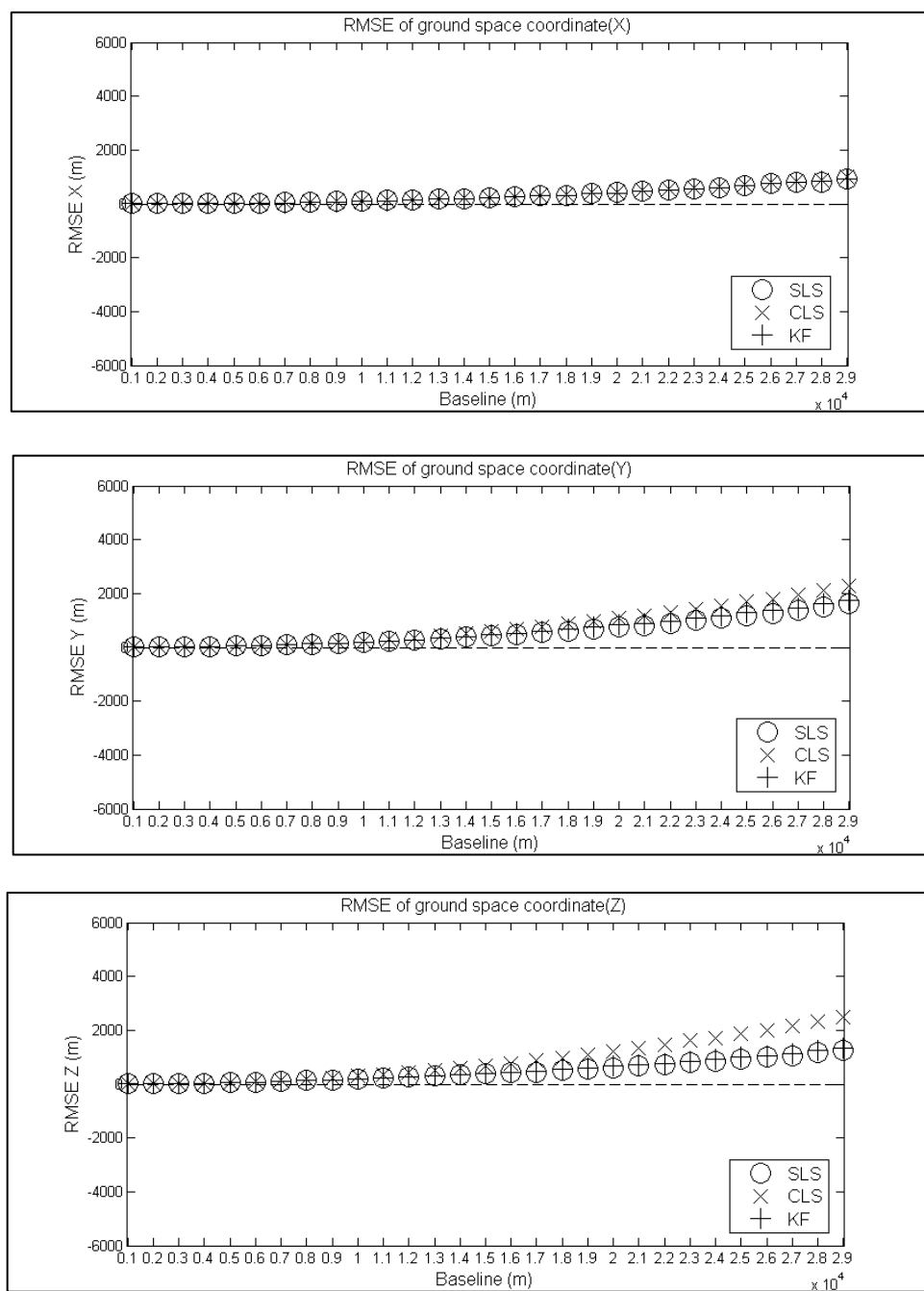


Figure 6.49 Strip Deformation Comparison, Simulation 3, Real Aspect Ratio (Top: X, Center: Y, Bottom: Z)

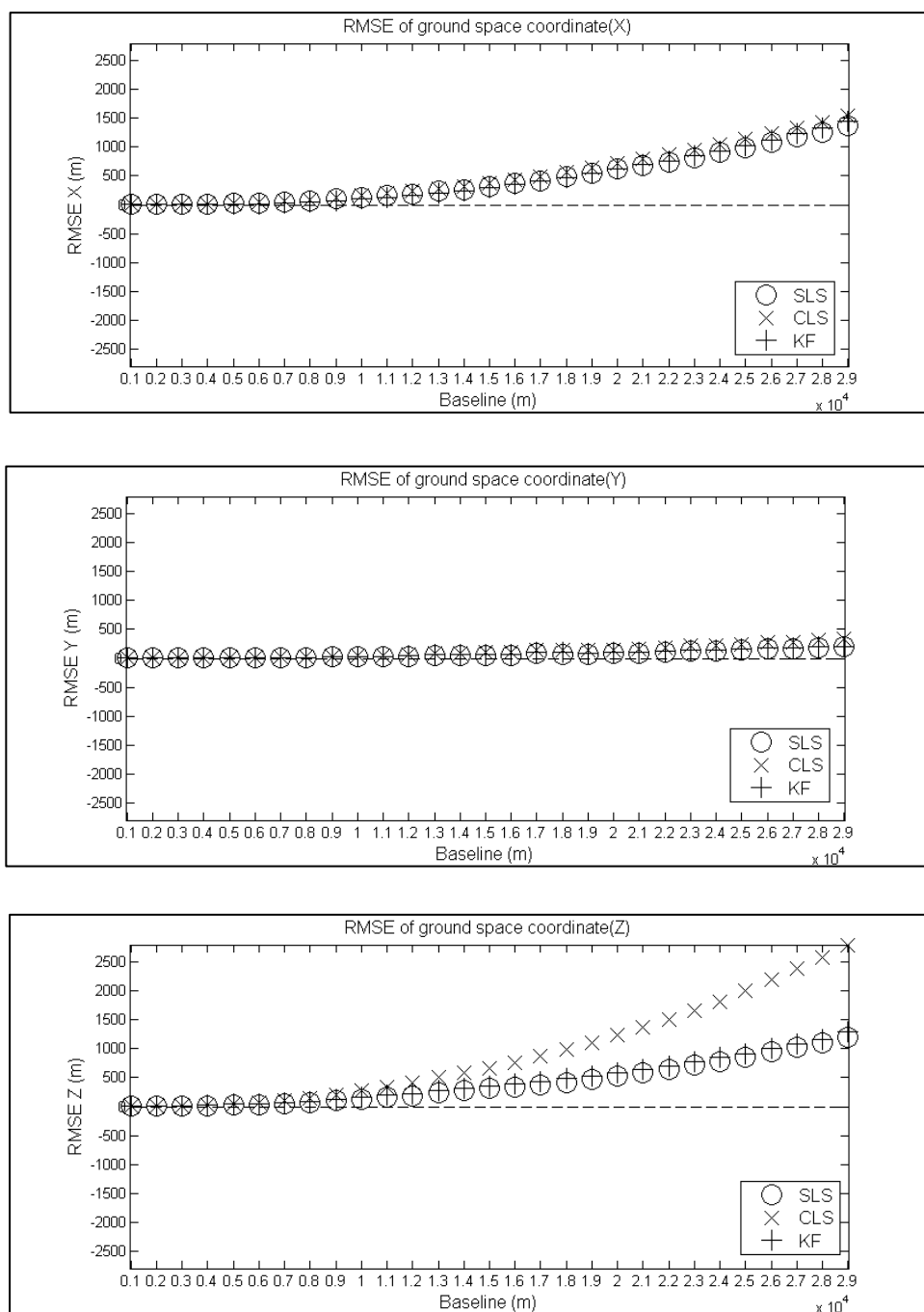


Figure 6.50 Strip Deformation Comparison, Simulation 4, y axis is exaggerated by  $\times 2.14$  (Top: X, Center: Y, Bottom: Z)

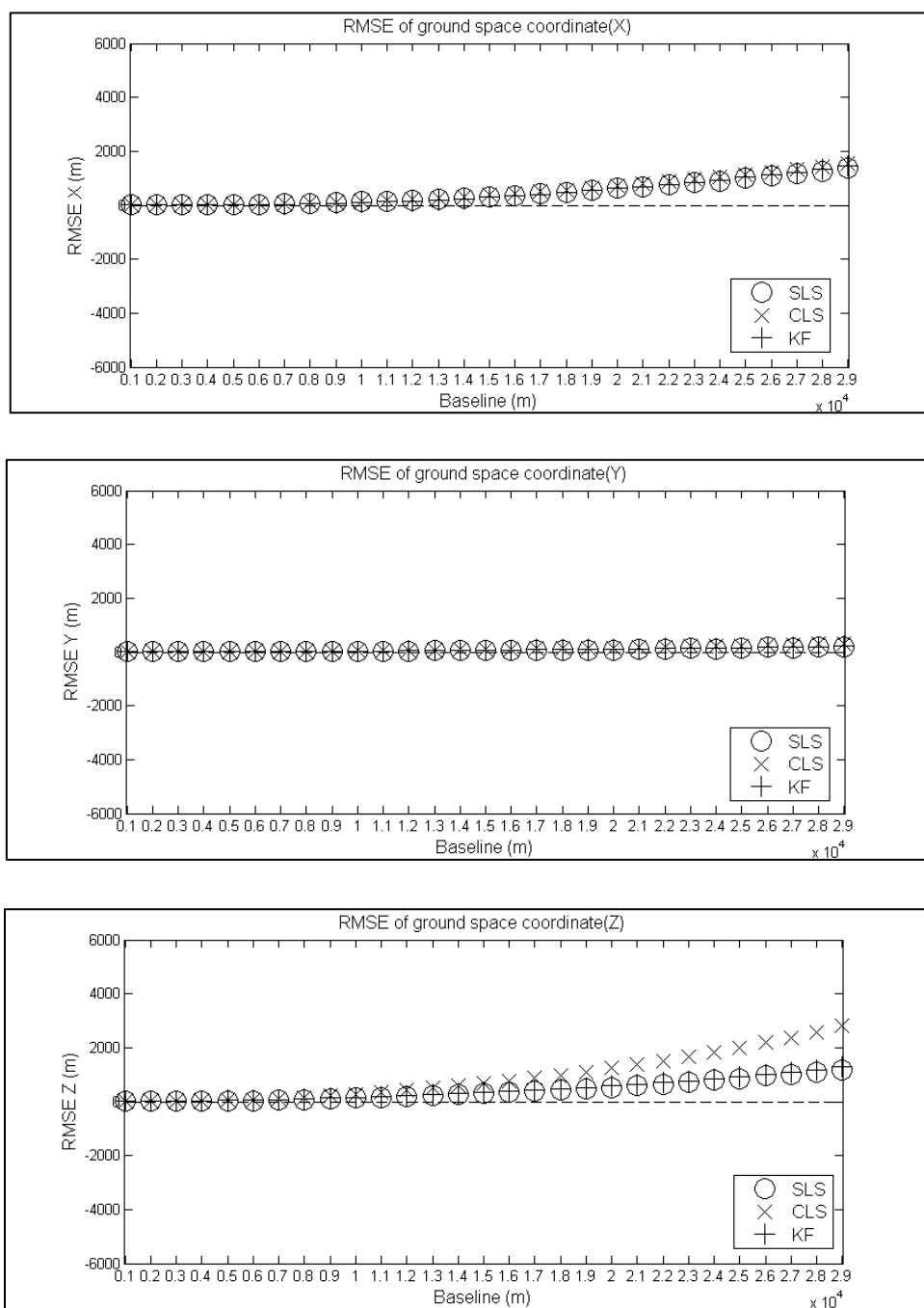


Figure 6.51 Strip Deformation Comparison, Simulation 4, Real Aspect Ratio (Top: X, Center: Y, Bottom: Z)



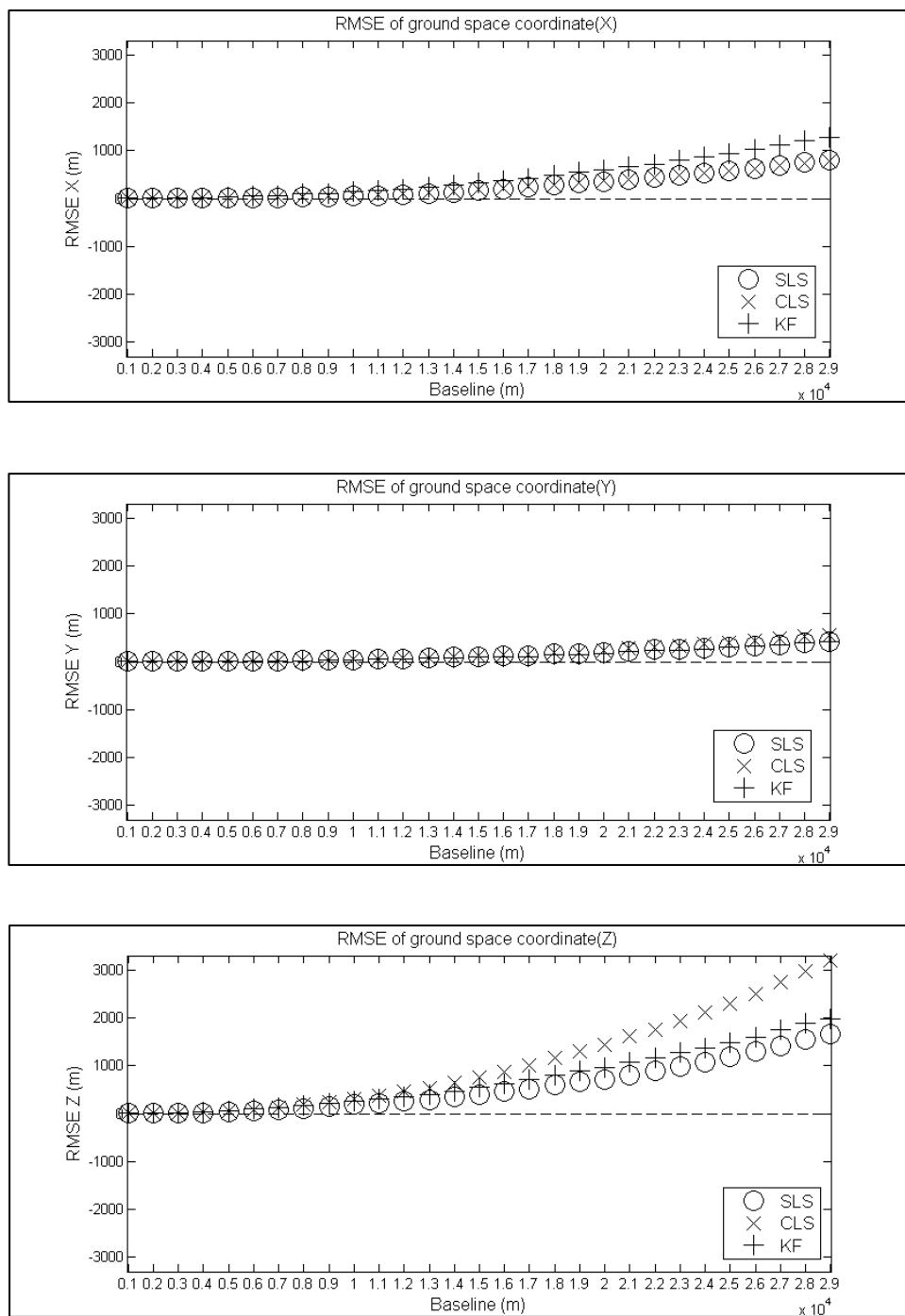


Figure 6.52 Strip Deformation Comparison, Simulation 5, y axis is exaggerated by  $\times 1.82$  (Top: X, Center: Y, Bottom: Z)

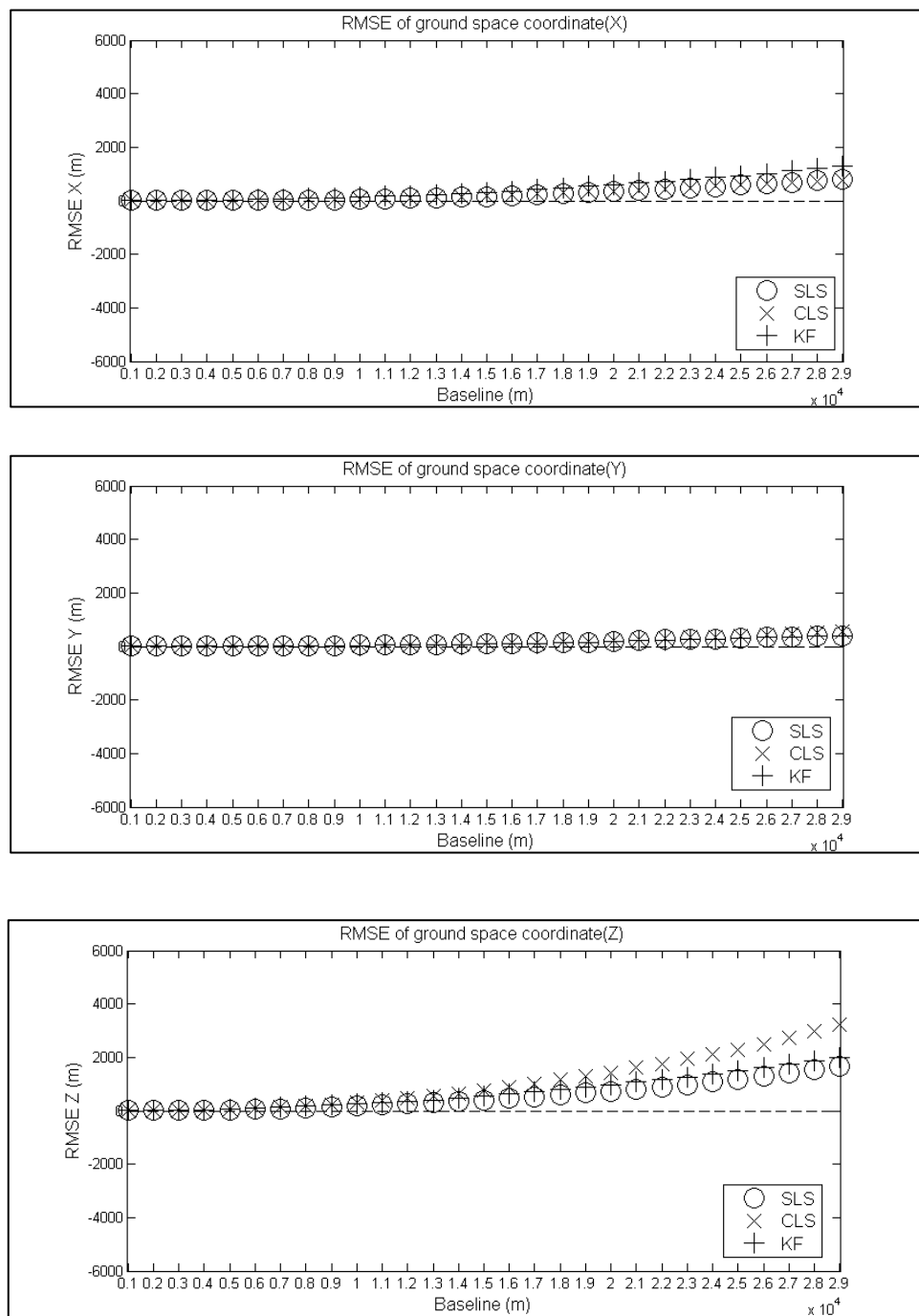


Figure 6.53 Strip Deformation Comparison, Simulation 5, Real Aspect Ratio (Top: X, Center: Y, Bottom: Z)

Table 6.56 shows the semi major and minor axes at the 90% confidence ellipsoid. SLS showed the largest values and KF showed the least values. As mentioned earlier, we believe that the propagated uncertainty of CLS and KF are understated, due to a simplified modeling of the scale restraint equation. Therefore, while interesting, these may not represent the precision achieved in practice. Representative plots are shown in Figure 6.54.

Table 6.56 The Semi Major and Minor Axis of Error Ellipsoid (units=meters)

	semi major	semi minor 1	semi minor 2
case1			
SLS	21.56	13.06	9.90
CLS	11.70	2.97	1.39
KF	7.71	1.99	0.91
case 2			
SLS	20.13	13.14	10.15
CLS	11.86	3.04	1.45
KF	7.80	2.01	0.93
case 3			
SLS	19.17	12.61	9.65
CLS	11.81	2.97	1.38
KF	7.46	1.92	0.90

Table 6.56 Continued.

case 4			
SLS	23.01	14.19	10.53
CLS	13.02	3.28	1.53
KF	8.10	2.09	0.98
case 5			
SLS	21.33	13.14	9.98
CLS	13.64	3.47	1.63
KF	7.91	2.05	0.97

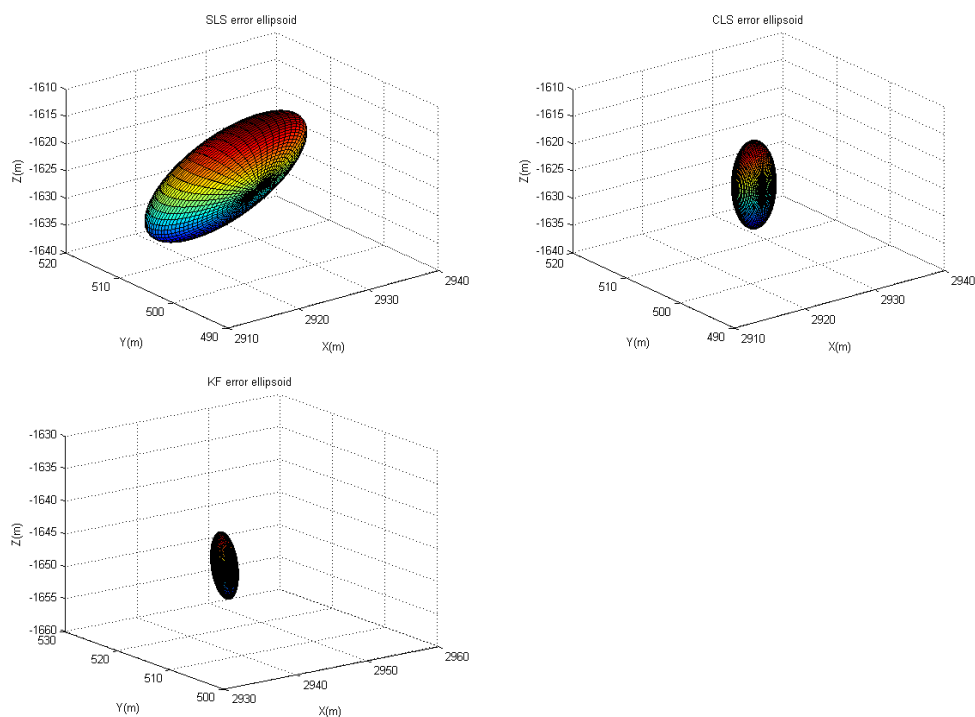


Figure 6.54 Error Ellipsoid from Each Approach (SLS: Top Left, CLS: Top Right, KF: Bottom Center)

Table 6.57 shows the memory occupancy of each solution and they were in the order of SLS, KF and CLS. The memory occupancy of KF and CLS are significantly smaller than SLS. Also, difference between CLS and KF was not significant compared to the difference between SLS and KF. Therefore, it was found out that KF are much more efficient than SLS.

Table 6.57 Average Memory Occupancy (MB). Note: Matlab returns slightly different numbers when running the same program

	CLS	SLS	KF
Simulation 1	0.44	142.68	1.36
Simulation 2	0.52	142.86	1.28
Simulation 3	0.68	144.38	1.56
Simulation 4	0.50	145.91	1.04
Simulation 5	0.47	144.31	1.55
mean	0.52	144.03	1.36

#### 6.4.2 Bundle Block Adjustment (BBA)

Using the simulated dataset, BBA with minimal constraints was implemented and the results were used as the criteria for accuracy assessment of automated relative and absolute orientation. We have a total of 232 control points and we divided them into two groups each with 116 control points. One

group was used as control points and the other group was used as check points. Two experiments were implemented swapping control and check point groups. For the BBA with minimal constraints, seven parameters were fixed (given with very large weight). Those seven parameters were six exterior orientation of the first image and  $X_L$  of the second image. Table 6.58 shows the residuals, and a word must be said about them because they appear quite small indicating a good adjustment, which is not the case. Even though this is a BBA, since (1) we have a minimal constraints and since (2) there is only one three ray point connecting adjacent triplets, the BBA is in fact performing a series of relative orientations. Recall that the image coordinates are corrupted by uncorrected systematic errors. With relative orientation the x-residual is known in advance to be effectively zero. Since the conjugate y-components will be corrupted by approximately the same magnitude, those residuals, while not zero, will be much too small. When an overall RMS is computed, including all of the zero and small residuals, it will seem unusually low, not revealing the true underlying errors. In adjustment parlance, the redundancy numbers are very small (near zero) forcing the errors into (incorrect) parameters estimation, with very little of the errors appearing in the residuals. This will be confirmed later when the AO shows a very poor fit to control points. As we mentioned before, the control points estimated from BBA with minimal constraints were transformed by seven parameter transformation and table 6.59 shows the results of seven parameter transformation.

Table 6.58 The RMS of Residuals (units=pixels)

	X	Y	total
Simulation 1			
BBA /w min const (1 <sup>st</sup> group)	0.00	0.67	0.48
BBA /w min const (2 <sup>nd</sup> group)	0.00	0.68	0.48
total	0.00	0.67	0.48
Simulation 2			
BBA /w min const (1 <sup>st</sup> group)	0.00	0.66	0.47
BBA /w min const (2 <sup>nd</sup> group)	0.00	0.67	0.48
total	0.00	0.67	0.47
Simulation 3			
BBA /w min const (1 <sup>st</sup> group)	0.00	0.64	0.45
BBA /w min const (2 <sup>nd</sup> group)	0.00	0.65	0.46
total	0.00	0.64	0.46
Simulation 4			
BBA /w min const (1 <sup>st</sup> group)	0.00	0.66	0.47
BBA /w min const (2 <sup>nd</sup> group)	0.00	0.68	0.48
total	0.00	0.67	0.47
Simulation 5			
BBA /w min const (1 <sup>st</sup> group)	0.01	0.83	0.59
BBA /w min const (2 <sup>nd</sup> group)	0.01	0.84	0.59
total	0.01	0.84	0.59

Table 6.59 Seven Parameter Transformation to the Control Points from BBA w/ Minimal Constraints

Parameter	$\omega$ (radian)	$\phi$ (radian)	$\kappa$ (radian)	Scale	$T_x$ (m)	$T_y$ (m)	$T_z$ (m)
case1							
group1	-0.01	-0.06	0.00	1.01	-137.91	-32.38	406.18
group2	0.01	-0.06	0.00	1.02	-150.86	-21.29	410.57
case2							
group1	-0.02	0.02	-0.05	0.98	178.25	-363.35	-163.75
group2	-0.01	0.03	-0.05	0.98	179.32	-355.73	-188.59
case 3							
group1	-0.03	-0.10	-0.09	1.02	-24.56	-664.26	657.18
group2	-0.03	-0.10	-0.09	1.02	-12.59	-657.71	665.56
case 4							
group1	0.01	-0.08	0.01	0.94	441.51	154.41	643.84
group2	-0.02	-0.08	0.01	0.93	451.31	138.03	618.56
case 5							
group1	0.02	0.13	0.02	0.98	253.75	149.33	-852.14
group2	-0.01	0.13	0.02	0.98	257.93	181.99	-870.64

Table 6.60 shows the misclosures at check points with only minimal constraints applied in model 1, followed by AO. It will be compared later to the misclosures from SLS, KF CLS with AO.



Table 6.60 Misclosures of Check Points (units=meters) with only MC plus AO

	RMS X	RMS Y	RMS Z	total RMS
Simulation 1				
BBA /w min const (1 <sup>st</sup> group)	47.69	11.56	122.54	76.21
BBA /w min const (2 <sup>nd</sup> group)	48.63	10.30	115.10	72.39
total	48.16	10.95	118.88	74.32
Simulation 2				
BBA /w min const (1 <sup>st</sup> group)	37.34	124.78	44.44	79.45
BBA /w min const (2 <sup>nd</sup> group)	37.34	119.69	50.51	78.04
total	37.34	122.26	47.57	78.75
Simulation 3				
BBA /w min const (1 <sup>st</sup> group)	59.36	189.98	193.57	160.30
BBA /w min const (2 <sup>nd</sup> group)	58.62	191.32	196.64	161.97
total	58.99	190.65	195.11	161.14
Simulation 4				
BBA /w min const (1 <sup>st</sup> group)	134.19	34.03	208.05	144.28
BBA /w min const (2 <sup>nd</sup> group)	136.77	28.28	209.99	145.61
total	135.49	31.29	209.02	144.95
Simulation 5				
BBA /w min const (1 <sup>st</sup> group)	87.96	45.19	255.90	158.39
BBA /w min const (2 <sup>nd</sup> group)	91.70	54.28	246.71	155.16
total	89.85	49.94	251.35	156.79

#### 6.4.3 Absolute Orientation for SLS, KF, and CLS

By using EO parameters estimated by SLS, KF and CLS for RO, the AO was implemented for two control points groups and the misclosures at the check points were estimated to compare with those from BBA with minimal constraints. Table 6.61 shows the results of the seven-parameter transformation. We can see that SLS and KF showed similar values for seven parameters, but CLS showed different values compared to the other methods. Table 6.62 shows the misclosures at check points for each of SLS, KF, CLS for each simulation. Table 6.63 shows the comparison of RMS of misclosures from SLS/AO, KF/AO, CLS/AO, and BBA/MC/AO. The accuracies shown in table 6.63 are, by conventional photogrammetric standards, quite poor. Recall that the image coordinates were purposely corrupted by systematic errors attempt to induce exaggerated strip deformation effects. So while it can be seen that the SLS and KF algorithms (KF augmented by results from SLS) have lower RMSE than CLS and BBA/MC, there results cannot be construed as recommended procedures. In practice one should always do the best and most complete job of camera calibration, rather than devise methods to work around an absence of calibration.

Table 6.61 The Seven Parameters Estimated by Absolute Orientation

Parameter		$\omega$ (radian)	$\phi$ (radian)	$\kappa$ (radian)	Scale	$T_x$ (m)	$T_y$ (m)	$T_z$ (m)
simulation1								
group1	SLS	0.00	-0.04	0.00	1.02	2185.47	1223.30	1839.41
	KF	-0.01	-0.03	0.00	1.01	2176.18	1227.14	1823.63
	CLS	-0.01	-0.06	-0.00	1.02	2233.36	1213.28	1953.79
group2	SLS	0.01	-0.04	0.00	1.02	2186.68	1241.87	1837.71
	KF	0.01	-0.03	0.00	1.01	2177.41	1247.92	1821.91
	CLS	0.01	-0.06	0.00	1.02	2234.19	1249.00	1950.49
simulation2								
group1	SLS	-0.01	0.00	-0.04	0.99	2294.06	1064.34	1646.93
	KF	0.00	0.01	-0.04	0.99	2297.00	1079.79	1614.97
	CLS	-0.02	0.02	-0.06	0.98	2283.23	959.90	1544.93
group2	SLS	-0.01	0.00	-0.04	0.99	2294.80	1065.52	1647.87
	KF	-0.01	0.00	-0.04	0.99	2297.12	1081.20	1616.17
	CLS	-0.02	0.02	-0.06	0.98	2283.84	964.52	1546.39

Table 6.61 Continued.

simulation 3								
group1	SLS	-0.01	-0.05	-0.06	1.02	2194.18	941.57	1911.22
	KF	-0.01	-0.06	-0.07	1.02	2191.63	920.77	1931.63
	CLS	-0.04	-0.10	-0.09	1.02	2305.58	761.82	2148.60
group2	SLS	-0.01	-0.05	-0.06	1.02	2194.69	945.87	1911.23
	KF	-0.01	-0.06	-0.07	1.02	2192.13	921.89	1931.39
	CLS	-0.03	-0.10	-0.09	1.02	2306.34	769.45	2150.19
simulation 4								
group1	SLS	0.01	-0.03	0.01	0.95	2555.14	1304.82	1772.44
	KF	0.01	-0.03	0.01	0.94	2599.20	1290.40	1758.42
	CLS	0.01	-0.09	0.01	0.94	2697.98	1315.84	2016.19
group2	SLS	0.00	-0.03	0.01	0.95	2555.14	1304.82	1772.44
	KF	0.00	-0.04	0.01	0.94	2597.97	1273.24	1758.36
	CLS	-0.02	-0.09	0.01	0.94	2696.40	1259.90	2016.69
simulation 5								

Table 6.61 Continued.

group1	SLS	0.01	0.07	0.01	0.98	2306.58	1322.05	1329.48
	KF	0.01	0.08	0.01	0.97	2346.78	1326.81	1282.35
	CLS	0.02	0.13	0.01	0.98	2251.78	1360.10	1038.85
group2	SLS	-0.01	0.07	0.01	0.98	2306.23	1303.21	1329.67
	KF	-0.01	0.08	0.01	0.97	2346.81	1309.73	1282.48
	CLS	-0.01	0.12	0.02	0.98	2251.37	1331.62	1041.54

Table 6.62 Misclosures at Check Points for Seven Parameter Transformation  
(units=meters)

		RMSE_X	RMSE_Y	RMSE_Z	RMSE
simulation 1					
group1	SLS	51.98	13.44	64.25	48.34
	KF	52.90	11.40	69.42	50.82
	CLS	48.64	11.89	115.92	72.90
group2	SLS	51.68	13.11	64.31	48.23
	KF	52.66	11.61	69.50	50.79
	CLS	48.47	10.87	115.95	72.83
simulation 2					

Table 6.62 Continued.

group1	SLS	25.43	76.66	5.90	46.75
	KF	28.05	80.23	13.05	49.64
	CLS	34.67	122.30	44.53	77.77
group2	SLS	26.94	74.75	5.90	46.00
	KF	29.56	78.34	12.95	48.92
	CLS	36.79	119.60	43.60	76.50
simulation 3					
group1	SLS	63.42	130.22	88.08	97.87
	KF	66.74	135.71	92.96	102.49
	CLS	59.84	187.43	188.15	157.18
group2	SLS	65.06	130.95	88.69	98.74
	KF	68.54	136.27	93.14	103.19
	CLS	61.44	188.24	189.91	158.41
simulation 4					
group1	SLS	114.60	28.68	86.99	84.70
	KF	134.62	28.18	83.25	92.82
	CLS	137.82	35.11	207.94	145.45
group2	SLS	115.15	26.37	87.37	84.83
	KF	135.12	26.13	83.76	93.02

Table 6.62 Continued.

	CLS	138.56	29.13	210.09	146.27
simulation 5					
group1	SLS	81.56	33.23	129.54	90.43
	KF	106.01	40.01	128.50	98.91
	CLS	91.08	46.76	247.93	154.87
group2	SLS	81.74	35.22	129.22	90.59
	KF	106.56	41.95	128.06	99.19
	CLS	91.27	53.90	247.44	155.42

Table 6.63 The Comparison of Misclosures of Each Method (units=meters)

		misclosures from ARO w/ 7 parameter transformation	misclosures BBA w/ minimal constraints	alleviation ratio
simulation 1	SLS	48.29	74.32	0.35
	KF	50.81		0.32
	CLS	72.87		-
simulation2	SLS	46.38	78.75	0.40
	KF	49.28		0.37
	CLS	77.14		-

Table 6.63 Continued.

simulation 3	SLS	98.31	161.14	0.38
	KF	102.84		0.36
	CLS	157.80		-
simulation 4	SLS	84.77	144.95	0.42
	KF	92.92		0.36
	CLS	145.86		-
simulation 5	SLS	90.51	156.79	0.42
	KF	99.05		0.37
	CLS	155.15		-



## CHAPTER 7. CONCLUSIONS AND RECOMMENDATIONS

### 7.1 Conclusions

In this research automated approaches for relative orientation were analyzed, with a further investigation into sequential versus batch estimation strategies. A number of conclusions can be drawn from the results.

(1) An HD digital video camera was calibrated using short baseline urban imagery, long baseline urban imagery (both with object distance  $\sim 30\text{m}$ ), in a laboratory with a target array, and using single strip aerial imagery. These were evaluated using control and check points together with the aerial imagery. The long baseline, urban, 30m dataset gave the best results and was subsequently used. The long baseline provides better angle diversity by increasing the range of  $\kappa$  to 0.46 radian (Urban3) from 0.16 radian (Urban 1,2) and the longer object distance is more consistent with the infinity focus lens position. The misclosures at check points and  $\sigma$  for camera parameters, expressed in pixels, in Urban 2 (narrower baseline) and Lab 1 (shorter object distance) were each 2.37m, 2.08m and 13.47 and 12.53 pixel. Note that high correlations permit individual sigmas to be larger than this actual effect. By the benefit of angle diversity and longer object distance of Urban 3, the misclosures and  $\sigma$  decreased to 1.41 m and 9.42

pixels. The accuracy increased by factor of 0.41, 0.32 and precision increased (sigma decreased) by factor of 0.30, 0.25 compared to each Urban 2 and Lab1. Figure 7.1 and Figure 7.2 show the comparison of misclosures and  $\sigma$  of each calibration results.

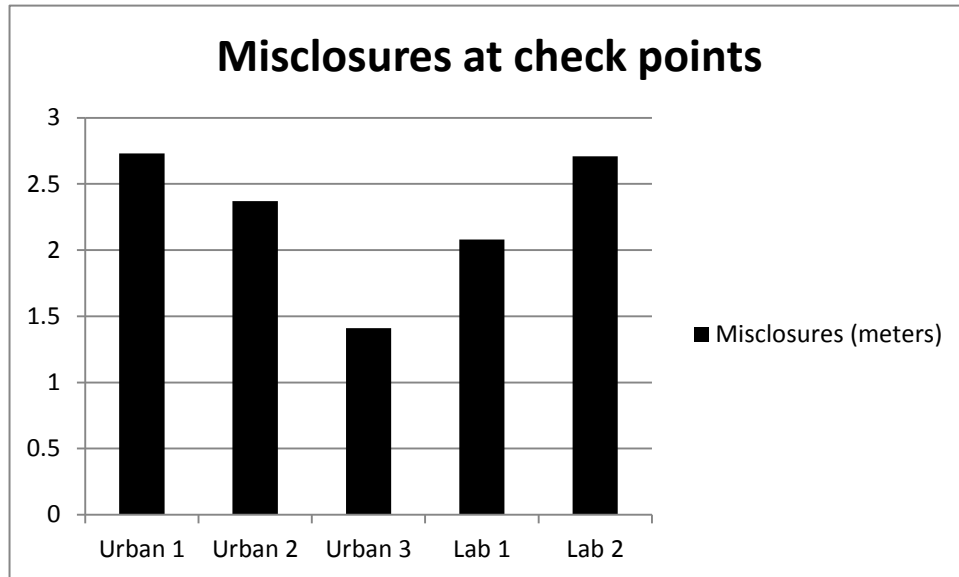


Figure 7.1 Misclosures at Check Points of Each Calibration

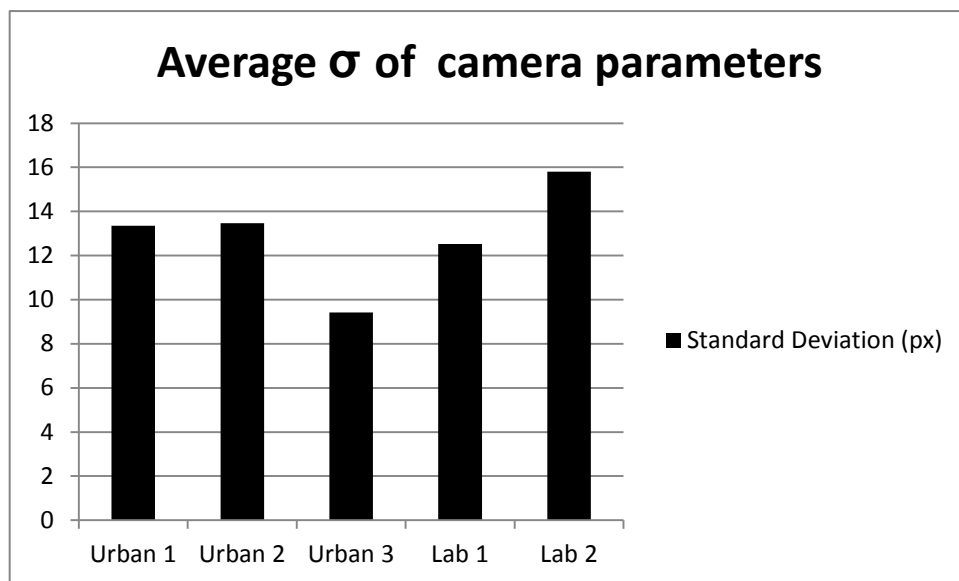


Figure 7.2 Average Standard Deviation of Each Calibration

(2) The large Purdue control point database was supplemented with addition points as required. These were acquired with either GPS/RTK using Indiana INCORS real time network or via static processing using OPUS. Point accuracy is on the order of 1 – 2 cm. This data proved extremely useful in evaluating imagery adjustment technique.

(3) Aerial imagery was acquired through the passenger window of a Cessna high wing aircraft. These low oblique imagery were captured at video rate, then downsampled to approximately 60 and 80% overlap. This proved to be a successful for collecting aerial imagery without having access to a dedicated aerial camera with conventional nadir view and attendant expense of airframe modification.

(4) An approach to automated relative orientation was developed using a colored Harris Laplace Corner Detector to find interest points. The detected points were matched by cross correlation across three image pyramid levels. Preliminary estimation and outlier removal were accomplished via RANSAC and the eight point algorithm. This was followed by conventional least squares using the coplanarity and scale restraint condition equations. This proved to be a successful and eminently workable approach to automated relative orientation and strip formation. This required an innovative interleaving of 80% and 60% overlap processing. The three ray scale restraints points proved resistant to automated detection and were measured manually.

(5) It was shown that the developed automated relative orientation (ARO) technique could be applied to terrestrial imagery. There was minimal strip deformation due to the short length of the strip. Therefore there were no significant differences (RMS discrepancy of 0.01cm for CLS, 0.05cm for KF from SLS) in 3D reconstruction between SLS, KF and CLS.

(6) For the aerial data experiment, three bundle block adjustments (BBA) were made (a) BBA using calibrated camera parameters together with control points and check points (CP/CKP), (b) BBA with self-calibration and (CP/CKP), and (c) BBA using calibrated camera parameters and with minimal constraints at only the beginning of the strip followed by absolute orientation (AO) using CP/CKP. Case (a) gave RMSE of 1.4m, case (b) gave RMSE of 24m, case (c) gave RMSE of 3.4m. Case (c), without CP's in the interior of the strip during adjustment, was quite similar in approach to the test strategies Simultaneous Least Squares (SLS), Kalman Filter (KF), and Cantilever Least Squares (CLS). In fact all three gave quite similar AO results (misclosures at check points - SLS: 4.25m, KF: 4.24m CLS: 4.24m) compared to the reference, case (c). As in the terrestrial case, it was concluded that the short length of the strip prevented differences from appearing.

(7) Since it was not practical to make a longer aerial collection, it was decided to produce such a long strip by simulation. Random perturbations did not produce the expected strip deformations, so such deformations were induced by

purposely introducing lens distortion errors. Large differences in check point error were now apparent between strip formation methods (For example, SLS: 48.29m, KF: 50.81m, CLS: 72.87m for simulation 1) but these should not be the basis for strong conclusions. In retrospect, little is to be gained by effectively experimenting with an uncalibrated camera. In fact, rigorous camera calibration is always recommended.

## 7.2 Recommendations

(1) In related testing, the eight point algorithm used in this research occasionally gave incorrect results. We believe that we found a workaround in those cases, see Benziger (2013), but this needs further study and confirmation.

(2) Matching by cross correlation is valid when the disparity function is constant within the match window. When this assumption is not met, pixel matching rather than area matching may have some benefits. This should be studied further.

(3) Matching for pass point selection for strip formation could be followed by matching for generation of a scene surface model. The geometric frame work supplied by the pass points would provide a rich starting point for surface model generation.

## LIST OF REFERENCES

## LIST OF REFERENCES

- Benziger, R. (2013). *Stereo Model Setup and 3D Data Capture For iOS Programming Environment*. (MS Thesis). Purdue University, West Lafayette, IN.
- Berg, R. F. (1983). Estimation and prediction for maneuvering target trajectories. *Automatic Control, IEEE Transactions on* 28(3), 294-304.
- Besl, P. J., & McKay, N. D. (1992). A method for registration of 3d shapes. *IEEE transactions on pattern analysis and machine intelligence*, 14(2), 239-256.
- Bethel, J. S. (2004). *Post Adjustment Statistics*. Retrieved from <https://engineering.purdue.edu/~bethel/506stat.pdf>.
- Brown, D. C. (1971). Close-range camera calibration. *photogrammetric engineering*, 37(8), 855-866.
- Brown, R. G., & Hwang, P. Y. C. (1997). *Introduction to random signals and applied kalman filtering* (3<sup>rd</sup> ed.). NY: John Wiley & Sons.

- Bruce, N., & Kornprobst, P. (2009). Harris corners in the real world: A principled selection criterion for interest points based on ecological statistics. In *Computer Vision and Pattern Recognition, 2009. CVPR 2009. IEEE Conference on* (pp. 2160-2167). IEEE.
- Brückner, M., Bajramovic, F., & Denzler, J. (2008), Experimental Evaluation of Relative Pose Estimation Algorithms. In *VISAPP (2)* (pp. 431-438).
- Clarke, T. A., & Fryer, J. G. (1998). The development of camera calibration methods and models. *The Photogrammetric Record*, 16(91), 51-66.
- Cooper, M.A.R., & Robson, S. (1996). Theory of close range photogrammetry. In K. B. Atkinson (Ed.), *Close Range Photogrammetry and Machine Vision*. Scotland, UK: Whittles Publishing.
- Dolloff, J. T. (2012). Kalman filter outputs for inclusion in video-stream metadata: Accounting for the temporal correlation of errors for optimal target extraction. In *Proc. of SPIE Vol* (Vol. 8360, pp. 83600I-1).
- Faugeras, O., & Robert, L. (1994). What can two images tell us about a third one?. In *Computer Vision—ECCV'94* (pp. 485-492). Berlin Heidelberg: Springer.



- Fischler, M., & Bolles, R. (1981). Random sample consensus: A paradigm for model fitting with application to image analysis and automated cartography. *Communications of Association for Computing Machinery*, 24(6), 381–395.
- Förstner, W., & Gulch, E (1987). A fast operator for detection and precise location of distinct points, corners and centres of circular features. In *Proc. ISPRS intercommission conference on fast processing of photogrammetric data* (pp. 281-305).
- Förstner, W., Wrobel, B., Paderas, F., Craig, R., Fraser, C. & Dolloff, J. (2004). Analytical photogrammetric operation. In J. C. McClone, E. M. Mikhail & J. Bethel (Eds). *manual of photogrammetry* (4th ed.) (pp. 763-948). Bethesda: ASPRS.
- Forsyth, D., Ponce, J. (2011). *Computer Vision, A Modern Approach* (2<sup>nd</sup> ed.). Upper Saddle River, NJ: Prentice Hall.
- Fraser, C. S. (1997). Digital camera self-calibration. *ISPRS Journal of Photogrammetry & Remote Sensing*, 52(4), 149-159.

- Fraundorfer, F., & Tanskanen, P., & Pollefeys, M. (2010). A minimal case solution to the calibrated relative pose problem for the case of two known orientation angles. In *Computer Vision—ECCV 2010* (pp. 269-282). Berlin Heidelberg: Springer.
- Fryer, J. G. (1996). Introduction. In K. B. Atkinson (Ed.), *Close Range Photogrammetry and Machine Vision*. Scotland, UK: Whittles Publishing.
- Gonzalez, R.C., Woods, R.E., and Eddins, S.L. (2004). *Digital Image Processing using Matlab*. Upper Saddle River, NJ: Prentice Hall.
- Grewal, M. S., & Andrews, A. P. (2001). *Kalman Filtering: Theory and Practice Using MATLAB* (2nd ed.). New York: Wiley, 2001.
- Habib, A., & Kelley, D. (2001). Automatic relative orientation of large scale imagery over urban areas using Modified Iterated Hough Transform. *ISPRS Journal of Photogrammetry & Remote Sensing*, 56(1), 29–41.
- Harris, C., & Stephens, M. (1988). A combined Corner and Edge Detector. *Proceedings from AVC '88: the 4th Alvey Vision Conference* (pp. 147-151).

- Haralick, R. M., Joo, H., Lee, C., Zhuang, X., Vaidya, V. G., & Kim, M. B. (1989). Pose estimation from corresponding point data. *IEEE Transactions of System Man and Cybernetics*, 19(6), 1426-1446.
- Heikkila, J. & O. Silven. (1997). A four-step camera calibration procedure with implicit image correction. In *Computer Vision and Pattern Recognition, 1997. Proceedings., 1997 IEEE Computer Society Conference on* (pp. 1106-1112). IEEE.
- Hartley, R. & Zisserman, A. (2000). *Multiple view geometry in computer vision*. Cambridge University Press: Cambridge, UK.
- Horn, B. K. P. (1990). Relative orientation. *International Journal of Computer Vision*, 4(1), 59-78.
- Horn, B. K. P. (1990). Recovering baseline and orientation from essential matrix. MIT AI Memo.
- Jasiobedzki, P., Se, S., Bondy, M & Jakola, R. (2008). Underwater 3D mapping and pose estimation for ROV operations. In *OCEANS 2008* (pp. 1-6). IEEE.

- Labe, T., & Förstner, W. (2006). Automatic relative orientation of images. *Proceedings of the 5th Turkish-German Joint Geodetic Days*, 29, 31.
- Lee, C. (1999). *Mathematical modeling of airborne pushbroom imagery using point and linear features*. (Doctoral dissertation), Purdue University, West Lafayette, IN.
- Liang, T. & Hiepke, C. (1996). Automatic relative orientation of aerial images. *Photogrammetric Engineering & Remote Sensing*, 62 (1), 47–55.
- Lindeberg, T. (1998). Feature detection with automatic scale selection. *International Journal of Computer Vision*, 30(2), 79–116.
- Lingua, A., Marenchino, D. & Nex, F. (2009). Performance Analysis of the SIFT Operator for Automatic Feature Extraction and Matching in Photogrammetric Applications. *Sensors*, 9(5), 3745-3766.
- Lobonc, T. (1996). *Human Supervised Tools for Digital Photogrammetric Systems*. (Doctoral dissertation). Purdue University, West Lafayette, IN.
- Longuet-Higgins, H. C., & Prazdny, K. (1980). The interpretation of moving retinal image. *Proceedings from the Royal Society of London, Series B, Biological Sciences*, 208 (1173), 385-397.

- Longuet-Higgins, H. C. (1981). A computer algorithm for reconstructing a scene from two projections, *Nature*, 293, 133-135.
- Lowe, D. G. (1999). Object recognition from local scale-invariant features. In *Computer vision, 1999. The proceedings of the seventh IEEE international conference on* (Vol. 2, pp. 1150-1157). IEEE.
- Lowe, D. G. (2004). Distinctive image features from scale-invariant keypoints. *International Journal of Computer Vision*, 2(60), 91-110.
- Mikhail, E. M. (1976). *Observation and least square*. New York, NY: University Press of America.
- Mikhail, E. M., Bethel, J. S., & McGlone, J. C., (2001). *Introduction to modern photogrammetry*. New York, NY: John Wiley & Sons.
- Mikolajczyk, K. & Schmid, C. (2001). Indexing based on scale invariant interest points. In *Computer Vision, 2001. ICCV 2001. Proceedings. Eighth IEEE International Conference on* (Vol. 1, pp. 525-531). IEEE.
- Mikolajczyk, K., & Schmid, C. (2004). Scale & Affine Invariant Interest Point Detectors. *International Journal of Computer Vision*, 60(1), 63–86.

- Mikolajczyk, K., & Schmid, C. (2005). A performance evaluation of local descriptors. *IEEE Transactions on Pattern Analysis and Machine Intelligence*, 27(10), 1615-1630.
- Moffitt, F. H., & Mikhail, E. M.(1980). *Photogrammetry*. New York, NY: Harper and Row.
- Montesinos, P., Gouet, V., & Deriche, R. (1998). Differential invariants for color images. In *Pattern Recognition, 1998. Proceedings. Fourteenth International Conference on* (Vol. 1, pp. 838-840). IEEE.
- Moravec. H. (1980). *Obstacle avoidance and navigation in the real world by a seeing robot rover*. Technical report CMU-RI-TR-80-03, Robotics Institute, Carnegie Mellon University.
- National Geodetic Survey (2012). OPUS: Online Positioning User Service, Retrieved from <http://www.ngs.noaa.gov/OPUS/>.
- Nister, D. (2004). An efficient solution to the five-point relative pose problem. *IEEE Transactions of Pattern Analysis and Machine Intelligence*, 26(6), 756-770.

- O'Neill, M., & Denos, M. (1996). Automated system for coarse-to-fine pyramidal area correlation stereo matching. *Image and Vision Computing* 14(3), 225-236.
- Pan, H. (1999). A direct closed-form solution to general relative orientation of two stereo views. *Digital Signal Processing*, 9(3), 195-221.
- Photometrix (2010). iWitness 2.0 [computer software]. Photometrix, Australia.
- Robert, L. (1996). Camera calibration without feature extraction. *Computer Vision, Graphics, and Image Processing*, 63(2), 314-325.
- Schmid, C., & Mohr, R. (1997). Local grayvalue invariants for image retrieval. *IEEE Transaction on Pattern Analysis and Machine Intelligence*, 19(5), 530-534.
- SONY (2011). Picture Motion Browser 5.8.02.10270 [computer software], SONY Corporation of America, USA.
- Stöttinger, J., Sebe, N., Gevers, T., & Hanbury, A. (2007). Colour interest points for image retrieval. In *Proceedings of the 12th Computer Vision Winter Workshop* (pp. 83-90).

- Stöttinger, J. (2008). *Local colour features for image retrieval. A more distinct coloured scale-invariant interest point detector*. Saarbrücken, Germany: VDM
- Sturm, P., & Maybank, S. (1999). On plane-based camera calibration: A general algorithm, singularities, applications. In *Computer Vision and Pattern Recognition, 1999. IEEE Computer Society Conference on*. (Vol. 1). IEEE.
- Sullivan, S., & Ponce, J. (1998). Automatic model construction, pose estimation, and object recognition from photographs using triangular splines. In *Computer Vision, 1998. Sixth International Conference on* (pp. 510-516). IEEE.
- Theiss, H. (2000). Photogrammetric triangulation and dynamic modeling of airborne video imagery. (Doctoral Dissertation), Purdue University, West Lafayette, IN.
- Tomasi, C., & Kanade, T. (1992). Shape and motion from image streams: A factorization method. *International Journal of Computer Vision*, 9(2), 137–154.



- Tomasi, C., & Shi, J. (1993). Direction of heading from image deformations. In *Computer Vision and Pattern Recognition, 1993. Proceedings CVPR'93., 1993 IEEE Computer Society Conference on* (pp. 422-427). IEEE.
- Tomasi, C., & Shi, J. (1996). Image Deformations Are Better than Optical Flow, *Mathematical and computer modelling*, 24(5), 165-175.
- Tsai, R. Y. (1987). A versatile camera calibration technique for high accuracy 3d machine vision metrology using off-the-shelf TV cameras and lenses. *IEEE J. Robotics Automat.*, RA-3(4), 323-344.
- Welch, G. & Bishop, G. (1995). An Introduction to the Kalman Filter. University of North Carolina, Department of Computer Science, TR 95-041.
- Weng, J., Huang, T. S., & Ahuja, N. (1989). Motion and structure from two perspective views: Algorithms, error analysis, and error estimation. *IEEE Transactions on Pattern Analysis and Machine Intelligence*, 11(5), 451-476.
- Weng, J., Cohen, P., & Herniou, M. (1992). Camera Calibration with Distortion Models and Accuracy Evaluation. *IEEE Transactions on Pattern Analysis and Machine Intelligence*, 14(10), 965-980.

Zhang, Z. (1999). Flexible camera calibration by viewing a plane from unknown orientations. In *Computer Vision, 1999. The Proceedings of the Seventh IEEE International Conference on* (Vol. 1, pp. 666-673). IEEE.

## APPENDICES

Appendix A Static GPS Survey Log

FILE: pt1.tps OP1340054656154

2005 NOTE: The IGS precise and IGS rapid orbits were not available  
 2005 at processing time. The IGS ultra-rapid orbit was/will be used to  
 2005 process the data.  
 2005

### NGS OPUS-RS SOLUTION REPORT

=====

All computed coordinate accuracies are listed as 1-sigma RMS values.  
 For additional information: <http://www.ngs.noaa.gov/OPUS/about.jsp#accuracy>

USER: DATE: June 18, 2012  
 RINEX FILE: pt1\_170k.12o TIME: 21:39:19 UTC

SOFTWARE: rsgps 1.37 RS64.prl 1.81 START: 2012/06/18 10:48:13  
 EPHEMERIS: igu16931.eph [ultra-rapid] STOP: 2012/06/18 11:17:21  
 NAV FILE: brdc1700.12n OBS USED: 3132 / 3195 : 98%  
 ANT NAME: JPSREGANT\_SD\_E NONE QUALITY IND. 30.93/ 37.55  
 ARP HEIGHT: 1.5 NORMALIZED RMS: 0.309

REF FRAME: NAD\_83(2011)(EPOCH:2010.0000) IGS08  
 (EPOCH:2012.46301)

X:	261532.204(m)	0.004(m)	261531.412(m)	0.004(m)
Y:	-4855068.640(m)	0.018(m)	-4855067.249(m)	0.018(m)
Z:	4114418.162(m)	0.013(m)	4114418.075(m)	0.013(m)

LAT:	40 25 42.51704	0.004(m)	40 25 42.54499	0.004(m)
E LON:	273 5 0.31719	0.004(m)	273 5 0.28682	0.004(m)
W LON:	86 54 59.68281	0.004(m)	86 54 59.71318	0.004(m)
EL HGT:	155.385(m)	0.021(m)	154.239(m)	0.021(m)
ORTHO HGT: [Geoid Model Not Yet Available w/ NAD83 (2011).]				
UTM COORDINATES STATE PLANE COORDINATES				
UTM (Zone 16) SPC (1302 IN W)				
Northing (Y) [meters]	4475319.075		575106.951	
Easting (X) [meters]	507076.122		914149.962	
Convergence [degrees]	0.05409869		0.10814037	

Point Scale	0.99960062	0.99996913
Combined Factor	0.99957625	0.99994476

US NATIONAL GRID DESIGNATOR: 16TEK0707675319(NAD 83)

#### BASE STATIONS USED

PID	DESIGNATION	LATITUDE	LONGITUDE	DISTANCE(m)
DM5395	INWL WEST LAFAYETTE CORS ARP			N402728.468
W0865534.309	3368.7			
DM5385	INMO INDOT MONTICELLO CORS ARP			N404333.353
W0864509.945	35825.9			
AH5611	WLCI WOLCOTT CORS ARP	N404830.241	W0870307.129	
43718.3				
DM5391	INRN RENSSELAER CORS ARP	N405646.977	W0870822.514	
60524.3				
DM5393	INTP TIPTON CORS ARP	N401649.307	W0860319.846	
74975.9				
DL2760	INHC HENDRICKS COUNTY CORS ARP			N394524.651
W0863123.536	81775.0			
DM5389	INPL PLAINFIELD CORS ARP	N394130.687	W0862339.851	
93138.9				
DM4642	INCL CLOVERDALE CORS ARP	N393211.116	W0864805.530	
99537.2				
DM5966	INWB WABASH CORS ARP	N404929.023	W0854811.622	
103970.0				

#### NEAREST NGS PUBLISHED CONTROL POINT

LB0872	PURDUE UNIV RESET 1959	N402543.	W0865449.	251.9
--------	------------------------	----------	-----------	-------

This position and the above vector components were computed without any knowledge by the National Geodetic Survey regarding the equipment or field operating procedures used.

FILE: second\_pt\_1.tps OP1340204307244

2005 NOTE: The IGS precise and IGS rapid orbits were not available  
 2005 at processing time. The IGS ultra-rapid orbit was/will be used to  
 2005 process the data.  
 2005

#### NGS OPUS-RS SOLUTION REPORT

=====

All computed coordinate accuracies are listed as 1-sigma RMS values.

For additional information: <http://www.ngs.noaa.gov/OPUS/about.jsp#accuracy>

USER:                      DATE: June 20, 2012  
RINEX FILE: seco171b.12o                      TIME: 15:21:17 UTC

SOFTWARE: rsgps 1.37 RS43.prl 1.81                      START: 2012/06/19 01:42:49  
EPHEMERIS: igu16932.eph [ultra-rapid]                      STOP: 2012/06/19 01:57:37  
NAV FILE: brdc1710.12n                      OBS USED: 1584 / 1719 : 92%  
ANT NAME: JPSREGANT\_SD\_E NONE                      QUALITY IND. 19.39/ 32.09  
ARP HEIGHT: 1.5                      NORMALIZED RMS: 0.284

REF FRAME: NAD\_83(2011)(EPOCH:2010.0000)                      IGS08  
(EPOCH:2012.46469)

X:	261532.194(m)	0.004(m)	261531.402(m)	0.004(m)
Y:	-4855068.683(m)	0.015(m)	-4855067.292(m)	0.015(m)
Z:	4114418.185(m)	0.013(m)	4114418.098(m)	0.013(m)

LAT:	40 25 42.51672	0.004(m)	40 25 42.54467	0.004(m)
E LON:	273 5 0.31667	0.004(m)	273 5 0.28629	0.004(m)
W LON:	86 54 59.68333	0.004(m)	86 54 59.71371	0.004(m)
EL HGT:	155.433(m)	0.019(m)	154.286(m)	0.019(m)
ORTHO HGT: [Geoid Model Not Yet Available w/ NAD83 (2011).]				

	UTM COORDINATES	STATE PLANE COORDINATES
	UTM (Zone 16)	SPC (1302 IN W)
Northing (Y) [meters]	4475319.065	575106.941
Easting (X) [meters]	507076.110	914149.950
Convergence [degrees]	0.05409859	0.10814028
Point Scale	0.99960062	0.99996913
Combined Factor	0.99957624	0.99994475

US NATIONAL GRID DESIGNATOR: 16TEK0707675319(NAD 83)

BASE STATIONS USED				
PID	DESIGNATION	LATITUDE	LONGITUDE	DISTANCE(m)
DM5395	INWL WEST LAFAYETTE	CORS	ARP	N402728.468
W0865534.309	3368.7			
DN2118	P775 PURDUE_U__IN2010	CORS	ARP	N402831.380
W0865931.483	8255.4			

DM5385 INMO INDOT MONTICELLO CORS ARP	N404333.353
W0864509.945 35826.0	
AH5611 WLCI WOLCOTT CORS ARP	N404830.241 W0870307.129
43718.4	
DM5391 INRN RENSSELAER CORS ARP	N405646.977 W0870822.514
60524.3	
DM5393 INTP TIPTON CORS ARP	N401649.307 W0860319.846
74975.9	
DL2760 INHC HENDRICKS COUNTY CORS ARP	N394524.651
W0863123.536 81775.0	
DM5389 INPL PLAINFIELD CORS ARP	N394130.687 W0862339.851
93138.9	
DM4642 INCL CLOVERDALE CORS ARP	N393211.116 W0864805.530
99537.2	

#### NEAREST NGS PUBLISHED CONTROL POINT

LB0872 PURDUE UNIV RESET 1959	N402543. W0865449.	251.9
-------------------------------	--------------------	-------

This position and the above vector components were computed without any knowledge by the National Geodetic Survey regarding the equipment or field operating procedures used.

Appendix B RTK GPS Survey Log

Table B.1 RTK GPS Survey Log

RTK for No 9	
Icon	
Name	99
Grid Northing (m)	4474669.128
Grid Easting (m)	506329.065
Elevation (m)	156.762
Code	
Control	
Note	
Photo Notes	
Layer	0
Source	
Std Dev n (m)	0.001
Std Dev e (m)	0.001
Std Dev u (m)	0.002
Std Dev Hz (m)	0.001
Point Symbol	
Geoid Separation (m)	
Color	



# Appendix C Exterior Orientation Parameters from Simulation

Table C.1 Simulation 1

SLS					
$X_L(m)$	$Y_L(m)$	$Z_L(m)$	$\omega(rad)$	$\phi(rad)$	$\kappa(rad)$
0.00	0.00	0.00	0.00	0.00	0.00
1004.75	-0.09	9.42	0.00	-0.01	0.00
1994.39	-1.77	25.54	0.00	-0.01	0.00
2989.44	-4.32	40.47	0.00	-0.01	0.00
3995.66	1.58	55.90	0.01	-0.02	0.00
4994.23	2.58	72.68	0.00	-0.02	0.00
5989.15	11.49	88.64	0.00	-0.02	0.00
6978.75	11.61	99.63	0.00	-0.02	0.00
7968.39	14.62	127.00	0.00	-0.02	0.00
8962.45	21.26	151.04	0.00	-0.02	0.00
9943.49	15.35	173.10	0.00	-0.02	0.00
10932.81	7.64	193.55	0.00	-0.02	0.00
11908.55	3.11	218.69	0.00	-0.03	0.00
12886.49	0.94	244.18	0.00	-0.03	0.00
13864.20	5.46	274.83	0.00	-0.03	0.00

Table C.1 Continued.

14842.25	4.89	303.90	0.00	-0.03	0.00
15818.85	3.79	335.68	0.00	-0.03	0.00
16781.79	2.68	378.12	0.00	-0.04	0.00
17760.47	-2.65	419.80	0.00	-0.04	0.00
18725.08	-8.11	461.18	0.00	-0.05	0.00
19690.46	-9.35	508.62	0.00	-0.05	0.00
20662.46	-10.67	555.03	0.00	-0.05	0.00
21625.41	-2.14	602.34	0.00	-0.05	0.00
22595.24	-20.42	656.51	0.00	-0.05	0.00
23557.09	-17.04	699.24	0.00	-0.05	0.00
24515.83	-19.32	757.89	0.00	-0.05	0.00
25471.99	-19.60	812.70	0.00	-0.06	0.00
26439.39	-29.38	872.87	0.00	-0.06	0.00
27390.33	-26.30	932.81	0.00	-0.06	0.00
28351.04	-24.53	991.24	0.00	-0.06	0.00
KF					
0.00	0.00	0.00	0.00	0.00	0.00
1004.75	-0.33	9.69	0.00	-0.01	0.00
2009.49	0.80	23.10	0.00	-0.01	0.00

Table C.1 Continued.

3013.24	0.94	31.14	0.00	-0.01	0.00
4024.56	3.31	41.08	0.00	-0.01	0.00
5031.73	0.93	51.40	0.00	-0.01	0.00
6033.81	6.48	59.94	0.00	-0.01	0.00
7030.64	1.99	62.87	0.00	-0.01	-0.01
8033.47	0.97	80.14	0.00	-0.01	0.00
9033.06	3.96	92.79	0.00	-0.01	-0.01
10018.31	-3.53	104.49	0.00	-0.01	0.00
11012.95	-13.05	115.77	0.00	-0.01	0.00
11996.33	-18.38	132.32	0.00	-0.02	0.00
12982.42	-20.43	148.60	0.00	-0.02	0.00
13966.55	-15.98	170.16	0.00	-0.02	0.00
14951.04	-18.62	189.90	0.00	-0.02	0.00
15934.08	-21.31	213.24	0.00	-0.02	0.00
16905.62	-25.43	246.90	0.00	-0.03	0.00
17892.28	-30.36	278.56	0.00	-0.03	0.00
18858.95	-33.80	311.06	0.00	-0.04	0.00
19832.57	-32.92	350.33	0.00	-0.04	0.00
20812.98	-34.64	387.94	0.00	-0.04	0.00

Table C.1 Continued.

21780.68	-25.49	426.81	0.00	-0.04	0.00
22757.06	-43.55	473.36	0.00	-0.04	0.00
23723.06	-39.65	509.27	0.00	-0.05	0.00
24685.85	-43.44	562.05	0.00	-0.05	0.00
25641.15	-41.85	612.86	0.00	-0.05	0.00
26607.00	-52.75	671.85	0.00	-0.06	0.00
27562.13	-49.12	732.52	0.00	-0.06	0.00
28522.83	-47.35	790.94	0.00	-0.06	0.00
CLS					
0.00	0.00	0.00	0.00	0.00	0.00
1004.75	-0.33	9.69	0.00	-0.01	0.00
1994.88	0.38	26.18	0.00	-0.01	0.00
2990.51	1.64	40.05	0.00	-0.01	0.00
3992.77	5.19	58.20	0.00	-0.02	0.00
4988.14	2.75	79.89	0.00	-0.02	0.00
5979.18	10.45	102.42	0.00	-0.02	0.00
6967.53	8.81	122.38	0.00	-0.02	0.00
7960.55	9.71	158.95	0.00	-0.03	0.00
8950.93	15.80	193.35	0.00	-0.03	0.00

Table C.1 Continued.

9929.35	9.60	228.09	0.00	-0.03	0.00
10915.77	0.90	264.39	0.00	-0.04	0.00
11891.25	-2.34	307.14	0.00	-0.04	0.00
12869.01	-2.42	351.59	0.00	-0.05	0.00
13844.72	3.23	403.27	0.00	-0.05	0.00
14821.99	0.94	454.58	0.00	-0.06	0.00
15798.43	-1.39	510.57	0.00	-0.06	0.00
16762.41	-4.75	577.64	0.00	-0.07	0.00
17742.72	-9.10	644.29	0.00	-0.07	0.00
18702.05	-9.98	712.23	0.00	-0.07	0.00
19668.94	-8.67	788.07	0.00	-0.08	0.00
20642.55	-9.91	863.29	0.00	-0.08	0.00
21603.09	-0.57	940.53	0.00	-0.08	0.00
22571.44	-17.25	1027.06	0.00	-0.08	0.00
23531.52	-13.10	1103.64	0.00	-0.09	0.00
24487.25	-16.50	1197.70	0.00	-0.09	0.00
25436.48	-15.04	1290.15	-0.01	-0.10	-0.01
26395.48	-26.02	1391.60	0.00	-0.10	0.00
27342.44	-21.64	1494.48	-0.01	-0.11	-0.01
28305.48	-23.28	1596.84	-0.01	-0.11	0.00

Table C.2 Simulation 2

SLS					
$X_L(m)$	$Y_L(m)$	$Z_L(m)$	$\omega(rad)$	$\phi(rad)$	$\kappa(rad)$
0.00	0.00	0.00	0.00	0.00	0.00
992.48	-4.62	-4.45	0.00	0.00	0.00
1993.26	-11.58	0.29	0.00	0.00	-0.01
2994.17	-18.55	-3.64	0.00	0.00	-0.01
3999.74	-26.24	4.24	0.00	0.00	-0.01
5004.33	-40.40	6.08	0.00	0.00	-0.02
6009.27	-60.32	7.96	0.00	0.00	-0.02
7011.18	-80.76	12.61	0.00	0.00	-0.02
8019.39	-109.03	11.84	0.00	0.00	-0.03
9025.53	-138.42	12.87	0.00	0.00	-0.03
10031.12	-166.54	10.49	0.00	0.00	-0.03
11038.94	-202.61	11.14	0.00	0.00	-0.03
12044.38	-240.32	14.36	0.00	0.00	-0.03
13046.41	-278.07	9.27	0.01	0.00	-0.03
14052.15	-316.57	10.31	0.00	0.00	-0.04
15068.30	-355.09	17.43	0.00	0.00	-0.04
16074.43	-396.92	13.58	0.00	0.00	-0.04

Table C.2 Continued.

17091.09	-438.48	18.57	0.00	0.00	-0.04
18088.23	-478.84	16.26	0.00	0.00	-0.04
19108.90	-533.78	10.71	0.00	0.00	-0.05
20122.57	-580.75	21.11	0.00	0.00	-0.05
21136.56	-637.75	11.72	0.00	0.00	-0.06
22150.36	-696.21	6.03	0.00	0.00	-0.06
23162.88	-757.46	11.77	0.00	0.00	-0.06
24175.32	-818.67	12.58	0.00	0.00	-0.07
25188.98	-880.75	16.81	0.00	-0.01	-0.07
26210.30	-950.21	18.34	0.00	0.00	-0.07
27224.82	-1019.87	10.03	0.00	0.00	-0.07
28232.28	-1085.31	15.53	0.00	0.00	-0.08
29243.42	-1172.32	21.02	0.00	0.00	-0.08
KF					
0.00	0.00	0.00	0.00	0.00	0.00
992.48	-4.58	-4.36	0.00	0.00	0.00
1984.95	-12.18	2.51	0.00	-0.01	-0.01
2991.40	-19.07	1.00	0.00	0.00	-0.01
3998.07	-27.34	10.26	0.00	-0.01	-0.01

Table C.2 Continued.

5004.22	-43.34	13.22	0.00	-0.01	-0.01
6017.83	-62.59	14.66	0.00	0.00	-0.01
7024.45	-74.79	17.65	0.00	0.00	-0.02
8040.02	-96.63	13.16	0.00	0.00	-0.02
9049.94	-120.99	9.81	0.01	0.00	-0.02
10063.36	-143.78	1.56	0.01	0.01	-0.02
11078.64	-175.99	-6.08	0.01	0.01	-0.02
12091.41	-205.00	-13.62	0.00	0.01	-0.03
13092.08	-238.66	-28.13	0.01	0.01	-0.03
14098.79	-274.73	-35.47	0.01	0.00	-0.04
15115.06	-312.77	-35.43	0.01	0.00	-0.04
16125.22	-353.75	-45.47	0.01	0.00	-0.04
17144.32	-394.56	-46.86	0.01	0.00	-0.04
18147.89	-436.02	-54.22	0.01	0.00	-0.04
19174.24	-489.09	-67.23	0.01	0.00	-0.04
20190.11	-532.99	-63.22	0.01	0.00	-0.05
21205.46	-588.37	-78.12	0.01	0.00	-0.05
22220.16	-641.18	-87.53	0.01	0.00	-0.05
23243.50	-699.94	-86.57	0.01	0.01	-0.06



Table C.2 Continued.

24267.23	-760.58	-93.72	0.01	0.01	-0.07
25281.64	-821.38	-98.38	0.01	0.00	-0.07
26306.91	-889.58	-105.48	0.01	0.01	-0.07
27312.60	-949.25	-118.09	0.01	0.00	-0.07
28322.73	-1009.04	-112.45	0.00	0.00	-0.08
29333.87	-1096.04	-106.96	0.00	0.00	-0.08
CLS					
0.00	0.00	0.00	0.00	0.00	0.00
992.48	-4.58	-4.36	0.00	0.00	0.00
1993.36	-9.78	0.59	0.00	0.00	-0.01
3002.46	-18.47	-4.43	0.00	0.00	-0.01
4015.23	-28.15	-0.47	0.00	0.00	-0.02
5023.88	-45.06	-4.02	0.00	0.00	-0.02
6038.48	-68.94	-9.14	0.00	0.00	-0.02
7046.73	-86.38	-12.71	-0.01	0.01	-0.03
8062.46	-115.09	-23.26	-0.01	0.01	-0.03
9074.12	-149.76	-32.38	0.00	0.01	-0.03
10091.32	-185.32	-47.01	0.00	0.01	-0.04
11108.70	-230.56	-61.50	0.00	0.02	-0.04

Table C.2 Continued.

12124.61	-274.44	-76.70	-0.01	0.02	-0.04
13127.44	-323.85	-98.98	0.00	0.02	-0.05
14138.26	-375.64	-115.55	-0.01	0.01	-0.06
15163.70	-431.56	-127.54	-0.01	0.02	-0.06
16175.43	-493.65	-151.57	-0.01	0.02	-0.06
17197.98	-555.99	-167.60	-0.01	0.02	-0.06
18204.90	-621.54	-191.02	0.00	0.02	-0.07
19235.56	-699.96	-221.63	-0.01	0.02	-0.07
20253.72	-769.35	-236.55	-0.01	0.02	-0.08
21271.93	-853.29	-270.97	-0.01	0.02	-0.08
22291.85	-935.88	-301.64	0.00	0.02	-0.08
23317.55	-1025.52	-323.62	-0.01	0.03	-0.09
24346.00	-1121.05	-354.97	-0.01	0.03	-0.10
25363.14	-1216.73	-385.87	-0.01	0.03	-0.10
26390.75	-1321.64	-420.62	0.00	0.03	-0.10
27408.72	-1428.59	-465.25	0.00	0.03	-0.10
28422.02	-1528.35	-496.35	0.00	0.04	-0.11
29440.99	-1651.50	-529.69	0.00	0.04	-0.11

Table C.3 Simulation 3

SLS					
$X_L(m)$	$Y_L(m)$	$Z_L(m)$	$\omega(rad)$	$\phi(rad)$	$\kappa(rad)$
0.00	0.00	0.00	0.00	0.00	0.00
1000.98	-5.95	12.99	0.00	-0.01	-0.01
2000.08	-16.98	22.23	0.00	-0.01	-0.01
3008.20	-28.61	34.96	0.00	-0.02	-0.02
3997.28	-48.16	57.82	0.00	-0.02	-0.02
4986.41	-74.42	82.95	0.00	-0.03	-0.03
5974.33	-101.92	117.08	0.00	-0.03	-0.03
6967.71	-129.42	151.65	0.00	-0.03	-0.03
7960.17	-157.45	189.68	0.00	-0.03	-0.03
8952.02	-204.16	227.36	0.01	-0.04	-0.04
9932.38	-250.86	263.96	0.01	-0.04	-0.04
10916.50	-298.17	298.82	0.01	-0.04	-0.05
11897.63	-345.77	347.39	0.01	-0.04	-0.05
12875.35	-401.40	389.40	0.01	-0.04	-0.05
13853.26	-458.63	431.75	0.01	-0.05	-0.05

Table C.3 Continued.

14831.23	-515.22	474.28	0.02	-0.05	-0.05
15799.21	-578.83	527.83	0.01	-0.05	-0.06
16767.52	-645.58	578.55	0.02	-0.06	-0.07
17738.31	-713.42	631.84	0.01	-0.06	-0.07
18702.86	-782.90	694.96	0.01	-0.06	-0.08
19659.96	-868.54	754.52	0.01	-0.07	-0.08
20620.72	-945.96	820.70	0.02	-0.07	-0.09
21582.74	-1039.61	893.66	0.02	-0.07	-0.09
22529.31	-1127.71	968.61	0.01	-0.08	-0.10
23474.29	-1228.11	1039.01	0.02	-0.08	-0.10
24419.12	-1324.39	1126.06	0.01	-0.09	-0.11
25363.95	-1431.64	1204.93	0.02	-0.10	-0.11
26306.57	-1543.44	1302.20	0.01	-0.10	-0.12
27248.15	-1657.61	1396.65	0.02	-0.10	-0.12
28186.50	-1774.92	1497.54	0.02	-0.10	-0.12
KF					
0.00	0.00	0.00	0.00	0.00	0.00

Table C.3 Continued.

1000.98	-6.05	13.01	0.00	-0.01	-0.01
2001.96	-18.23	22.11	0.00	-0.01	-0.01
2999.86	-24.25	37.94	0.00	-0.02	-0.01
3998.41	-43.20	65.04	0.00	-0.03	-0.02
4999.93	-78.15	90.97	0.01	-0.03	-0.03
5989.56	-107.02	122.48	0.01	-0.03	-0.03
6990.13	-141.27	152.83	0.01	-0.03	-0.03
7982.62	-172.19	187.17	0.01	-0.03	-0.04
8962.82	-219.29	224.72	0.01	-0.04	-0.04
9941.79	-266.41	262.88	0.01	-0.04	-0.05
10927.64	-316.64	299.15	0.01	-0.04	-0.05
11899.54	-369.90	349.21	0.01	-0.05	-0.05
12876.95	-428.48	395.21	0.01	-0.05	-0.06
13850.46	-491.81	442.19	0.02	-0.05	-0.07
14824.11	-562.57	491.40	0.02	-0.06	-0.07
15784.56	-636.46	553.75	0.02	-0.06	-0.07
16751.61	-712.67	615.28	0.02	-0.07	-0.08

Table C.3 Continued.

17723.47	-790.50	679.26	0.02	-0.07	-0.08
18700.55	-870.54	749.03	0.02	-0.07	-0.09
19658.88	-962.71	810.41	0.02	-0.07	-0.09
20619.64	-1046.78	877.18	0.02	-0.07	-0.09
21578.78	-1146.28	949.86	0.02	-0.07	-0.09
22523.22	-1237.94	1026.75	0.02	-0.08	-0.10
23467.30	-1342.61	1098.48	0.02	-0.09	-0.11
24413.95	-1441.22	1186.39	0.02	-0.09	-0.11
25358.97	-1548.31	1264.91	0.02	-0.10	-0.11
26295.53	-1655.20	1361.55	0.01	-0.10	-0.12
27232.90	-1765.35	1457.70	0.02	-0.10	-0.12
28171.25	-1882.65	1558.59	0.02	-0.10	-0.12
CLS					
0.00	0.00	0.00	0.00	0.00	0.00
1000.98	-6.05	13.01	0.00	-0.01	-0.01
1998.70	-17.69	22.58	0.00	-0.02	-0.01
2989.92	-25.73	41.28	0.00	-0.03	-0.02

Table C.3 Continued.

3984.14	-46.96	73.70	0.00	-0.03	-0.02
4980.06	-83.15	107.16	0.01	-0.04	-0.03
5959.94	-115.78	148.73	0.00	-0.04	-0.04
6945.78	-148.77	198.68	0.00	-0.05	-0.04
7928.34	-185.50	255.84	0.00	-0.06	-0.05
8904.15	-238.50	321.46	0.00	-0.07	-0.06
9879.10	-298.33	390.14	0.00	-0.07	-0.06
10862.66	-362.37	459.10	0.00	-0.07	-0.07
11828.18	-428.25	543.21	0.00	-0.08	-0.07
12798.69	-497.59	628.15	-0.01	-0.09	-0.08
13765.68	-574.06	716.90	-0.01	-0.09	-0.09
14729.71	-658.17	812.29	0.00	-0.10	-0.09
15687.47	-750.93	923.47	-0.01	-0.11	-0.09
16649.85	-845.91	1035.37	-0.01	-0.12	-0.10
17617.54	-947.28	1151.51	-0.01	-0.12	-0.11
18576.50	-1048.40	1277.39	-0.01	-0.13	-0.11
19526.68	-1165.43	1400.37	-0.01	-0.13	-0.12

Table C.3 Continued.

20479.40	-1276.64	1531.49	-0.01	-0.14	-0.12
21430.33	-1401.54	1672.12	-0.01	-0.14	-0.13
22367.81	-1523.95	1817.18	-0.01	-0.15	-0.14
23307.03	-1660.08	1958.56	-0.01	-0.16	-0.14
24245.21	-1791.40	2116.95	-0.01	-0.16	-0.15
25180.96	-1937.71	2267.11	-0.01	-0.17	-0.15
26108.27	-2081.66	2436.48	-0.02	-0.17	-0.16
27035.53	-2228.13	2605.96	-0.02	-0.18	-0.17
27959.99	-2385.32	2782.98	-0.01	-0.18	-0.17



Table C.4 Simulation 4

SLS					
$X_L(m)$	$Y_L(m)$	$Z_L(m)$	$\omega(rad)$	$\phi(rad)$	$\kappa(rad)$
0.00	0.00	0.00	0.00	0.00	0.00
994.48	-1.80	-1.97	0.01	0.00	0.00
1997.95	1.62	7.23	0.00	-0.01	0.00
3011.18	-12.18	2.38	0.01	-0.01	0.00
4024.51	-6.31	5.57	0.00	-0.01	0.00
5042.95	-1.76	19.38	0.00	-0.02	0.00
6049.97	1.77	37.32	0.00	-0.03	0.00
7072.26	-2.01	56.52	0.00	-0.03	0.00
8099.88	-10.82	77.71	0.00	-0.03	0.00
9133.00	-13.25	99.55	0.01	-0.03	0.00
10158.09	-8.52	134.16	0.00	-0.03	0.00
11194.65	-0.68	158.69	0.00	-0.04	0.00
12225.92	0.30	196.43	0.00	-0.05	0.00
13274.70	9.21	239.42	0.00	-0.05	0.00
14326.21	17.85	282.97	0.00	-0.05	0.01
15386.33	9.67	323.32	0.00	-0.05	0.01
16445.65	16.23	363.60	0.01	-0.04	0.00
17504.97	22.66	401.49	0.01	-0.05	0.01

Table C.4 Continued.

18570.97	40.85	449.84	0.01	-0.05	0.01
19637.18	45.65	498.22	0.01	-0.05	0.01
20703.47	56.91	549.34	0.01	-0.06	0.01
21769.36	61.53	612.53	0.01	-0.07	0.01
22838.31	61.50	680.15	0.01	-0.07	0.01
23928.10	75.40	745.44	0.01	-0.07	0.01
25016.96	76.24	827.69	0.01	-0.07	0.01
26105.91	90.26	903.85	0.01	-0.08	0.01
27196.26	104.49	973.44	0.01	-0.08	0.01
28293.44	111.57	1057.39	0.01	-0.08	0.01
29391.10	124.32	1138.33	0.01	-0.09	0.01
30488.95	143.79	1232.87	0.01	-0.09	0.01
KF					
0.00	0.00	0.00	0.00	0.00	0.00
994.48	-1.54	-1.68	0.00	-0.01	0.00
1988.95	3.78	8.11	0.00	-0.01	0.00
2991.17	-9.29	7.28	0.00	-0.02	0.00
4004.39	-2.50	14.88	0.00	-0.02	0.00
5020.73	4.53	31.46	0.00	-0.02	0.00

Table C.4 Continued.

6025.20	4.59	53.61	0.00	-0.03	0.00
7047.32	4.93	74.56	0.00	-0.03	0.00
8070.82	6.31	99.50	0.00	-0.03	0.00
9099.86	5.29	127.64	0.00	-0.04	0.00
10125.95	11.77	168.72	0.00	-0.04	0.00
11168.72	26.46	198.24	0.00	-0.04	0.01
12201.45	29.63	238.87	-0.01	-0.05	0.00
13253.47	39.65	284.18	0.00	-0.05	0.01
14311.22	45.08	332.11	0.00	-0.05	0.01
15365.52	42.51	376.01	0.00	-0.05	0.01
16434.72	48.72	423.13	0.00	-0.05	0.00
17499.85	54.74	465.46	0.00	-0.05	0.01
18570.14	70.96	518.36	0.00	-0.06	0.01
19644.22	75.91	571.30	0.00	-0.06	0.00
20729.82	87.76	624.28	0.00	-0.06	0.01
21800.96	95.21	687.62	0.00	-0.07	0.01
22878.27	96.75	756.37	0.00	-0.07	0.01
23983.24	109.81	821.53	0.00	-0.07	0.01
25074.70	109.66	903.74	0.00	-0.08	0.01

Table C.4 Continued.

26176.15	117.80	981.22	0.01	-0.08	0.01
27276.18	128.27	1052.03	0.01	-0.08	0.01
28373.05	130.82	1140.23	0.01	-0.09	0.01
29498.35	135.94	1228.16	0.01	-0.09	0.01
30596.20	155.42	1322.69	0.01	-0.09	0.01
CLS					
0.00	0.00	0.00	0.00	0.00	0.00
994.48	-1.54	-1.68	0.00	-0.01	0.00
1997.88	1.85	8.64	0.00	-0.01	0.00
2998.22	-10.22	9.88	0.00	-0.02	0.00
4006.55	-4.83	24.92	0.00	-0.03	0.00
5022.89	4.91	54.35	0.00	-0.04	0.00
6030.27	7.75	92.36	0.00	-0.05	0.00
7051.78	8.54	133.11	0.00	-0.05	0.00
8079.56	11.79	181.39	0.00	-0.06	0.00
9106.72	14.98	236.70	0.00	-0.07	0.00
10135.95	24.62	308.48	0.00	-0.07	0.01
11178.77	42.02	371.86	0.00	-0.08	0.01
12214.42	47.01	450.07	0.00	-0.09	0.00

Table C.4 Continued.

13267.35	59.68	536.18	0.00	-0.09	0.01
14316.44	71.72	628.09	0.00	-0.09	0.01
15365.46	75.30	723.42	0.00	-0.10	0.01
16418.87	84.30	829.73	0.00	-0.11	0.01
17481.53	95.63	939.35	0.00	-0.11	0.01
18550.05	117.55	1062.30	0.00	-0.12	0.01
19623.67	127.91	1188.43	0.00	-0.13	0.01
20705.48	145.23	1318.39	0.00	-0.13	0.02
21775.66	158.83	1460.47	0.00	-0.14	0.02
22848.69	168.02	1610.86	0.00	-0.15	0.02
23944.01	191.06	1764.60	0.00	-0.16	0.01
25025.53	201.76	1938.86	0.00	-0.16	0.01
26111.08	225.44	2116.53	0.00	-0.17	0.02
27201.27	247.95	2293.84	0.00	-0.18	0.01
28288.53	265.09	2493.75	0.00	-0.19	0.02
29395.14	284.88	2698.61	0.00	-0.20	0.02
30499.02	314.79	2918.00	0.00	-0.20	0.02

Table C.5 Simulation 5

SLS					
$X_L(m)$	$Y_L(m)$	$Z_L(m)$	$\omega(rad)$	$\phi(rad)$	$\kappa(rad)$
0.00	0.00	0.00	0.00	0.00	0.00
1009.21	2.50	-10.40	0.00	0.01	0.00
2003.70	1.46	-23.07	0.00	0.02	0.00
2990.11	-4.04	-52.17	0.00	0.02	0.00
3979.02	-5.29	-77.62	0.00	0.02	0.00
4970.93	-8.06	-106.57	0.00	0.02	0.00
5972.34	7.97	-136.33	0.00	0.03	0.00
6974.06	5.59	-171.17	0.00	0.03	0.01
7976.63	15.62	-219.24	0.00	0.04	0.01
8979.14	22.11	-265.17	0.00	0.04	0.01
9975.01	25.44	-310.12	0.00	0.04	0.01
10992.88	29.38	-365.38	0.00	0.05	0.01
12001.62	34.07	-413.79	0.00	0.05	0.01
13017.49	38.86	-478.80	0.00	0.06	0.01
14028.63	55.72	-527.95	0.00	0.06	0.01
15053.00	63.76	-593.13	0.00	0.06	0.01
16081.91	77.49	-663.73	0.00	0.07	0.01

Table C.5 Continued.

17110.92	92.86	-733.87	0.00	0.07	0.01
18139.70	110.87	-818.07	-0.01	0.07	0.01
19169.07	136.39	-896.15	-0.01	0.07	0.02
20202.48	142.15	-987.76	-0.01	0.08	0.02
21237.18	172.61	-1089.02	-0.01	0.09	0.02
22269.88	193.24	-1186.27	-0.01	0.10	0.02
23311.86	211.96	-1296.01	-0.01	0.10	0.02
24360.47	230.78	-1404.10	-0.01	0.11	0.02
25406.49	247.98	-1532.40	-0.01	0.11	0.02
26443.56	269.02	-1649.54	-0.01	0.11	0.02
27481.55	290.37	-1777.79	-0.01	0.11	0.02
28524.00	313.18	-1904.92	-0.01	0.12	0.02
29584.95	337.38	-2051.15	-0.01	0.12	0.02
KF					
0.00	0.00	0.00	0.00	0.00	0.00
1009.21	2.60	-10.29	0.00	0.01	0.00
2018.41	1.23	-24.57	0.00	0.02	0.00
3008.94	-5.35	-56.01	0.00	0.02	0.00
4020.03	-5.69	-86.76	0.00	0.03	0.00

Table C.5 Continued.

5022.22	-10.98	-124.78	0.00	0.03	0.00
6033.54	2.65	-162.64	0.00	0.04	0.00
7047.62	-2.10	-207.15	0.00	0.04	0.00
8056.86	6.87	-262.28	0.00	0.04	0.00
9071.90	10.24	-313.44	0.00	0.05	0.00
10093.70	8.31	-368.22	0.00	0.06	0.01
11124.49	11.34	-435.80	0.00	0.06	0.01
12150.76	14.90	-497.53	0.00	0.06	0.01
13175.53	18.10	-575.28	0.00	0.07	0.01
14218.29	32.61	-642.46	0.00	0.07	0.01
15251.68	39.42	-726.28	0.00	0.08	0.01
16292.80	50.84	-814.31	0.01	0.08	0.01
17337.56	66.28	-901.71	0.00	0.08	0.01
18384.37	82.93	-1003.66	0.00	0.09	0.01
19430.89	108.87	-1098.25	0.00	0.09	0.02
20476.88	126.20	-1201.60	-0.01	0.09	0.02
21533.83	156.43	-1314.24	-0.01	0.10	0.02
22590.54	176.10	-1421.96	-0.01	0.10	0.02
23655.52	194.28	-1541.52	-0.01	0.10	0.02



Table C.5 Continued.

24724.75	223.70	-1657.33	-0.01	0.11	0.02
25799.84	239.08	-1791.76	-0.01	0.12	0.02
26874.07	260.44	-1920.17	-0.01	0.12	0.02
27931.58	284.53	-2058.73	-0.01	0.12	0.02
29005.89	310.75	-2195.24	-0.01	0.13	0.02
30066.84	334.95	-2341.46	-0.01	0.12	0.02
CLS					
0.00	0.00	0.00	0.00	0.00	0.00
1009.21	2.60	-10.29	0.00	0.01	0.00
2005.30	1.72	-22.87	0.00	0.02	0.00
2994.19	-4.32	-52.63	0.00	0.02	0.00
4003.40	-2.54	-84.67	0.00	0.03	0.00
5003.12	-7.01	-127.21	0.00	0.04	0.00
6011.06	8.28	-172.45	0.00	0.05	0.00
7025.99	4.81	-228.53	0.00	0.05	0.01
8034.97	18.05	-300.90	0.00	0.06	0.01
9043.98	25.23	-372.72	0.00	0.07	0.01
10062.02	28.55	-452.41	0.00	0.08	0.01
11085.47	35.07	-548.28	0.00	0.09	0.01

Table C.5 Continued.

12103.49	43.78	-641.24	0.00	0.10	0.01
13120.69	52.51	-753.47	0.00	0.10	0.01
14154.39	71.79	-859.90	0.00	0.11	0.02
15175.71	84.01	-985.35	0.00	0.12	0.01
16205.06	102.42	-1118.53	0.00	0.13	0.02
17238.39	120.92	-1254.90	0.00	0.13	0.02
18270.52	142.33	-1409.86	0.00	0.14	0.02
19304.21	175.26	-1562.12	0.00	0.15	0.03
20332.64	197.82	-1726.57	-0.01	0.16	0.03
21371.95	235.08	-1905.02	-0.01	0.16	0.03
22411.42	261.97	-2083.88	-0.01	0.18	0.03
23454.87	290.24	-2279.56	-0.01	0.18	0.03
24499.21	328.95	-2474.38	-0.01	0.19	0.03
25545.35	356.10	-2690.72	-0.01	0.20	0.03
26591.54	387.78	-2903.81	-0.01	0.21	0.03
27629.32	424.48	-3133.02	-0.01	0.21	0.04
28668.52	459.43	-3365.79	-0.01	0.22	0.04
29719.85	496.26	-3620.49	-0.01	0.23	0.04

VITA

## VITA

Jae Sung Kim  
School of Civil Engineering, Purdue University

Education

Bachelor of Engineering, Civil Engineering, 1997, Korea University, Seoul, Republic of Korea

Master of Engineering, Civil Engineering, 1999, Korea University, Seoul, Republic of Korea

M.S in Civil Engineering, Civil Engineering, 2006, Purdue University, West Lafayette, Indiana

Ph.D., Civil Engineering, 2013, Purdue University, West Lafayette, Indiana

Research Interests

Photogrammetry, Geographic Information System, Remote Sensing.